# Spin dependent electron transport in semiconductors due to the Pauli principle

Fabian Cadiz

Thèse présentée pour obtenir le grade de

**Docteur de l'École Polytechnique**

Spécialité: Physique des Solides

par

**Fabian CADIZ**

---

# Transport dépendant du spin dans les semi-conducteurs: une conséquence du principe de Pauli

---

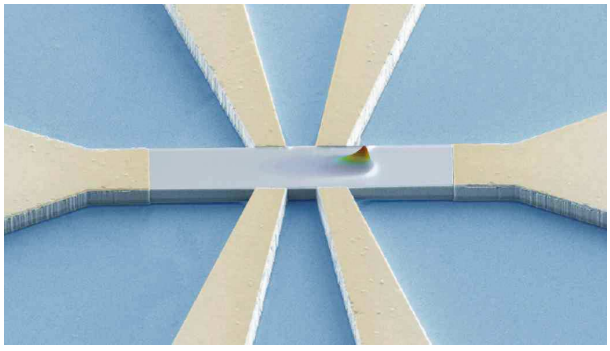

Soutenue publiquement le 6 Juillet 2015 devant le jury composé de:

| | | |
|---|---|---|
| Dr. Kees VAN DER BEEK | École Polytechnique-LSI | Président |
| Dr. Pierre RENUCCI | INSA Toulouse -LPCNO | Rapporteur |
| Dr. Jöerg WUNDERLICH | Hitachi Cambridge Laboratory | Rapporteur |
| Dr. Jean-Marie GEORGE | CNRS/Thales | Examinateur |
| Dr. Daniel PAGET | École Polytechnique-PMC | Directeur de thèse |
| Dr. Alistair ROWE | École Polytechnique-PMC | Co-directeur de thèse |

Thesis submitted to obtain the title of

**Docteur de l'École Polytechnique**

Specialty: SOLID STATE PHYSICS

---

# Spin dependent electron transport in semiconductors due to the Pauli principle

---

by

**Fabian CADIZ**

defended publicly on July 6, 2015 in front of the jury composed of

| | | |
|---|---|---|
| Dr. Kees VAN DER BEEK | École Polytechnique-LSI | President |
| Dr. Pierre RENUCCI | INSA Toulouse-LPCNO | Reviewer |
| Dr. Jöerg WUNDERLICH | Hitachi Cambridge Laboratory | Reviewer |
| Dr. Jean-Marie GEORGE | CNRS/Thales | Examiner |
| Dr. Daniel PAGET | École Polytechnique-PMC | Thesis advisor |
| Dr. Alistair ROWE | École Polytechnique-PMC | Thesis advisor |

Prepared at Laboratoire de Physique de la matière condensée
École Polytechnique, Palaiseau, France,

Pour la patrie, les sciences et la gloire.

- Devise de l'Ecole Polytechnique.

A ma famille et à Manon Chloé.

# Remerciements

Ce travail a été réalisé au sein du laboratoire de Physique de la Matière Condensée de l'Ecole Polytechnique, dans le groupe Electrons Photons Surfaces. Je voudrais ici exprimer toute ma reconnaissance aux nombreuses personnes avec lesquelles j'ai eu l'opportunité de collaborer durant mon doctorat.

Tout d'abord, je tiens à remercier Kees Van der Beek,Pierre Renucci,Jöerg Wunderlich et Jean-Marie George de m'avoir fait l'honneur d'accepter de faire partie de mon jury de thèse et d'accorder leur jugement positif à ce travail.

Ensuite, je tiens à remercier mes deux encadrants à qui je dois ma formation dans le monde de la recherche scientifique, Daniel et Alistair. Travailler avec vous pendant ces années a été un vrai plaisir. Avec le temps je me rends compte de l'énorme chance que j'ai eu d'avoir rencontré de si bonnes personnes, toujours optimistes et prêtes à répondre à toutes mes questions, vous savez vraiment encourager les doctorants. Daniel est un physicien exceptionnel à qui je dois une bonne partie de mes connaissances sur la physique des semi-conducteurs. J'ai beaucoup apprécié aussi tous les moments partagés avec Alistair, les discussions scientifiques (généralement autour d'un café), les voyages au LPS d'Orsay pour utiliser leur micro-soudeuse (sans son aide je serais encore en train d'essayer d'utiliser cette machine) et aussi le match Chili-Australie en compagnie des crevettes.

Ce travail de thèse doit beaucoup à Lucio Martinelli qui, par exemple, est capable de construire en cinq minutes un obturateur fait maison juste pour me dépanner. Ses solutions ne connaissent pas de limites, allant jusqu'à percer un trou dans un mur pour voler des photons depuis une pièce voisine. Merci pour toute ton aide et ta bonne humeur. Merci à Jacques Peretti de m'avoir donné la possibilité de travailler au PMC lors de mon stage

de M1, ainsi qu'à Yves Lassailly par sa sympathie et ses conseils amicaux.

Merci aux informaticiens Julien Monguillon et Denis Coupvent-Desgraviers, ainsi qu'aux deux directeurs successifs du laboratoire durant cette période: François Ozanam et Mathis Plapp. Merci à Anne Marie Dujardin pour sa gentillesse au moment de m'aider avec les nombreuses démarches administratives qu'on a à faire tout au long du doctorat. J'ai beaucoup apprécie la sympathie et le travail d'André Wack, un grand mécanicien qui nous a fourni des magnifiques pièces pour le microscope. Un grand merci aussi à Didier Lenoir pour ses boîtiers électroniques, et à Patrice Delaroque pour m'avoir donné le titre de directeur du labo, ce qui motiverait n'importe quelle personne!. Merci à Audrey Lemaréchal et Alexandra Belus de la Graduate School.

Merci à Steve Arscott de nous avoir fabriqué de si beaux échantillons. A mon avis, ce sont de vrais objets artistiques. Merci aussi à Thierry Amand de m'avoir accueilli lors de ma visite à Toulouse, ainsi qu'à Philippe Barate et Delphine Lagarde pour les expériences de TRPL effectuées au Laboratoire de Physique et Chimie des Nano-objets. Je voudrais aussi remercier Chris Weber, qui m'a accueilli dans son laboratoire en Californie où j'ai eu le luxe de travailler sur une expérience de spectroscopie ultra rapide de haute volée. Merci à Giovanni Vignale pour ses conseils concernant les calculs de spin Coulomb drag.

Merci à Marcin Konczykowski qui m'a généreusement offert un flacon de GE varnish, ce qui m'a permis de refroidir efficacement les photo-électrons. Merci à Sophie Guéron, Hélène Bouchiat et Richard Deblock du Laboratoire de Physique de Solides d'Orsay pour nous avoir facilité l'accès à leur machine à souder dans nombre d'occasions. Merci aussi à Robert Cortes pour ses mesures de diffraction de rayons X et à Eric Larquet pour le temps qu'il a dédié à imager mes échantillons au TEM.

Mon amour pour la physique des semi-conducteurs doit beaucoup à la personne d'Emmanuel Rosencher, dont les cours à l'Ecole Polytechnique m'ont énormément inspiré à suivre cette branche de la physique. Merci à Khalid et Jacques de m'avoir amené gentillement à Orsay suite au séminaire de Bernard Sapoval, dont j'ai malheureusement raté la fin.

Mes remerciements vont ensuite à Rafael Benguria et Maria Cristina Depassier qui m'ont inspiré à suivre le chemin de la physique, ainsi qu'à mes amis Matthias Salas, Joaquin Arancibia, Felipe Garrido, Patricio Gallardo, Jaime Arancibia, Pedro Ramaciotti. Merci au team Nano de l'Institut d'Optique (Nicolas,Jérémie,Laurent,Valérian,Julien) pour leur sympathie. Merci à mes amis du laboratoire, Tapajyoti, Maria, Nikoletta, Nan, Lili, Lucie, Nicolas, Petr, Duc, Marco, Godefroy, Maxime, Tim, Hongye, Stefan, Anne, Marine et tant d'autres. Grâce à vous les pauses cafés ont été toujours un des meilleurs moments de la journée. Je remercie à mon frère qui m'a toujours stimulé intellectuellement et à qui je doit mon intérêt pour les sciences, merci à mes parents et à ma sœur pour leur soutien constant. Finalement, merci à Manon Chloé, mon amour, et sa magnifique famille grâce à laquelle j'aime la France encore plus!.

# Spin dependent electron transport in semiconductors due to the Pauli principle


## Abstract

This thesis is concerned with transport of photoinjected minority spin-polarized electrons in doped semiconductors, as a function of both the density and the temperature of the injected electron gas. In $p^+$ GaAs thin films, charge and spin transport is investigated theoretically and experimentally by using a novel polarized microphotoluminescence ($\mu$PL) technique which consists in imaging the spatially-resolved PL intensity and polarization under a tightly-focused circularly-polarized CW laser excitation. Study of the experimental profiles at low concentration and under an applied electric field shows that the minority electron mobility is mainly determined by the electron temperature instead of the majority hole statistics, introducing a puzzling piece to the current understanding of scattering processes in semiconductors.

At higher densities, this experimental technique has allowed us to explore a novel charge-spin coupling mechanism which modifies electron transport. Under degeneracy of the electron gas (high concentration, low temperature), a dip at the centre of the spin polarization profile appears with a polarization maximum at a distance of about $r = 2\ \mu m$ from the excitation. This counterintuitive result reveals that photoelectron diffusion depends on spin, as a direct consequence of the Pauli principle which causes in general a concentration dependence of the spin stiffness. This results in a novel spin filter effect in an homogeneous material. The other effects which may modify spin transport in a degenerate electron gas are thermoelectric spin currrents (spin Soret currents) and ambipolar coupling with holes. A comparison of the data with a numerical solution of the coupled diffusion equations reveals that ambipolar diffusion increases the steady-state photo-electron density at the centre and therefore the amplitude of the degeneracy-induced spin-dependent diffusion, while the contribution of the spin Soret current is negligible. Coulomb spin drag and bandgap renormalization are negligible due to electrostatic screening by the hole gas. It is expected for degeneracy to have larger effects in confined systems, such as quantum wells, where both the spin stiffness and the mobility can have a much stronger spin dependence.



## Keywords

Spin diffusion, semiconductor spintronics, GaAs, Pauli principle

# Transport dépendant du spin dans les semi-conducteurs: une conséquence du principe de Pauli


### Résumé

Ce travail de thèse est consacré à l'étude du transport des électrons minoritaires dans des semi-conducteurs dopés, en fonction de la densité et de la température du gaz électronique. Dans des couches minces de $p^+$-GaAs, le transport de la charge et du spin est étudié par une approche à la fois théorique et expérimentale en utilisant une technique de microscopie originale permettant d'imager en régime stationnaire le profil de charge et de spin en fonction de la distance $r$ par rapport à la tache d'excitation lumineuse. L'étude de ces profils à faible concentration et sous l'application d'un champ électrique montre que la mobilité des électrons minoritaires est déterminée principalement par la température des électrons et non pas par la statistique des trous majoritaires, ce qui invite à reformuler les modèles théoriques concernant les processus de diffusion des porteurs minoritaires dans les semi-conducteurs.

Notre technique expérimentale a aussi permis d'explorer un nouveau mécanisme de couplage charge-spin lorsque la densité électronique est élevée. En effet, sous l'effet de la dégénérescence du gaz électronique (forte concentration, basse température), une diminution de la polarisation de spin à l'endroit d'excitation apparaît, avec un maximum de polarisation visible à environ $r = 2\ \mu$m. Ce résultat contre-intuitif révèle le fait que, à cause du principe de Pauli, la diffusion des photo-électrons dépend du spin, car la raideur de spin devient une fonction de la concentration dans le régime dégénéré. Un nouveau mécanisme de filtre à spin en découle, mais qui ne fait pas intervenir une interface entre deux matériaux. D'autres effets pouvant modifier le transport de spin dans le régime dégénéré sont les courants thermoélectriques de spin (courants de Soret) et le couplage ambipolaire avec les trous. Une comparaison entre les profils expérimentaux et une solution numérique des équations de diffusion couplées montre que le couplage ambipolaire augmente la concentration de photo-électrons dans le régime stationnaire, et donc l'amplitude des effets liées à la dégénérescence, tandis que les courants de Soret de spin sont négligeables. Des effets tels que la renormalisation du gap et le couplage Coulombien entre électrons de spin opposés sont négligeables à cause de l'écrantage des intéractions électron-électron induit par le gaz électronique. On s'attend à ce que l'effet de la dégénérescence augmente dans des systèmes confinés, tels que les puits quantiques, où la raideur de spin et la mobilité peuvent avoir des dépendances en spin encore plus fortes.

# Contents

Contents

**Contents**

# Chapter 1

# Introduction

The injection, control and transport of non equilibrium minority charge carriers in semiconductors is central to the operation of all bipolar microelectronic devices, including transistors, light emitting diodes and photovoltaic cells. The main physical quantities of importance to device operation are the ensemble averaged minority carrier lifetime, $\tau$, diffusion constant, $D$, and mobility, $\mu$. This thesis will be concerned with non-uniformly photoexcited p-type GaAs so that $\tau_e$, $D_e$ and $\mu_e$ will be associated with the charge transport of the minority photo-electron density, $n$. The two fundamental laws which determine charge transport in semiconductors are Fick's law for diffusion:

$$\vec{J}_c^{\text{diff}} = qD_e\vec{\nabla}n \tag{1.1}$$

and Ohm's law for drift under the influence of an electric field $\vec{E}$:

$$\vec{J}_c^{\text{drift}} = \sigma_e\vec{E} = qn\mu_e\vec{E} \tag{1.2}$$

where $q$ is the absolute value of the electron charge, and $\sigma_e = qn\mu_e$ is the electronic conductivity. The total charge current is then $\vec{J}_c = \vec{J}_c^{\text{drift}} + \vec{J}_c^{\text{diff}}$.

In addition to carrying charge, a conduction electron also carries spin angular momentum. Being spin-1/2 particles, each electron will have associated with it a spin component of $\pm 1/2$ projected along some arbitrary axis. These two orthogonal states are denoted here by $+$ and $-$. In consequence, the electronic density in a non-magnetic semiconductor can be split into two sub-populations $n_+$ and $n_-$, corresponding to the two possible values of

the spin, such that $n = n_+ + n_-$ and $\vec{J_c} = \vec{J_+} + \vec{J_-}$, where each $\vec{J_\pm}$ current is defined as the sum of Eq.(1.1) and Eq.(1.2) for each sub-population $n_\pm$. The ensemble spin polarization is defined by $\mathscr{P} = (n_+ - n_-)/n$. This polarization is zero in the absence of any perturbation that destroys time reversal symmetry (e.g. magnetic field, circularly polarized photoexcitation,...), i.e. $n_+ = n_-$.

In contrast, under a bandgap resonant photoexcitation of p-GaAs with circularly polarized photons, conservation of angular momentum dictates that the minority electrons will be spin polarized, thus generating a non-equilibrium magnetization proportional to the spin density $s = n_+ - n_-$. In this case, spin currents are naturally defined as the difference between currents of spin + and spin − electrons:

$$\vec{J}_s^{\text{diff}} = \vec{J}_+^{\text{diff}} - \vec{J}_-^{\text{diff}} = qD_s\vec{\nabla}s \tag{1.3}$$

and

$$\vec{J}_s^{\text{drift}} = \vec{J}_+^{\text{drift}} - \vec{J}_-^{\text{drift}} = \sigma_s\vec{E} = qs\mu_s\vec{E}. \tag{1.4}$$

These currents define the spin diffusion constant $D_s$ and the spin mobility $\mu_s$. It might naively be assumed that in all circumstances $D_e = D_s$ and $\mu_e = \mu_s$ since the minority electrons carry both the charge and the spin. This however is not generally the case, and this is one of the reasons why spin transport in semiconductors is of interest. It is also the potential route to new functionalities in semiconductor spintronics. In general $D_e \neq D_s$ and $\mu_e \neq \mu_s$ because of a variety of coupling phenomena, the most important of which is the spin-orbit interaction. This directly results in a number of unusual and intriguing phenomena such as the spin Hall effect (Kato et al. (2004),Wunderlich et al. (2005)), in which a longitudinal charge current in a bar shaped semiconductor generates a transverse spin current in the abscence of any magnetic field. The spin-orbit interaction modifies spin transport so that in Eq.(1.4), the spin conductivity should be replaced by a conductivity matrix $[\sigma_s]$. The spin-orbit interaction can be tuned in semiconductor heterostructures to obtain a controlled precession of the electron's spin during transport. This provides the basis for electrical manipulation of the spin (Wang et al. (2013a,b); Balocchi et al. (2011)).

Another effect recently reported by Weber et al. (2005), because of which $D_e \neq D_s$, is a

spin-spin coupling phenomenom which not only modifies the spin conductivity but also modifies the spin diffusion current in Eq.(1.3); the so-called spin Coulomb drag. During a scattering event between electrons of opposite spin, the total momentum of the electrons is preserved, and so therefore is the charge current. In contrast, this collision does not necessarily conserve the spin current, as can be seen in Fig.1.1.

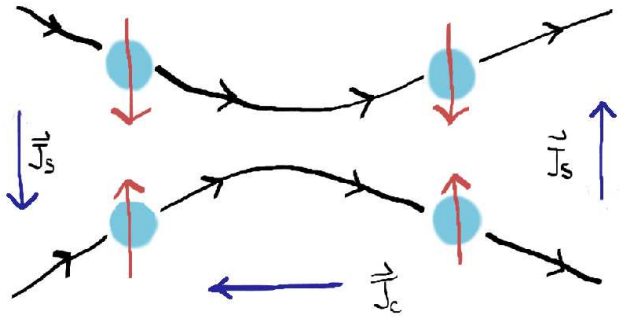


**Figure 1.1:** A representation of an electron-electron scattering, that conserves charge momentum and current, but not spin momentum and current, which reverses its sign after the collision in this example.

The ensemble of electrons relax its momentum at a rate $1/\tau_m$, where $\tau_m$ is the momentum relaxation time. This does not include electron-electron ($e$-$e$) collisions, since they preserve the total momentum. For spin transport, however, $e$-$e$ collisions must be included in the total collision rate, given by $1/\tau_m + 1/\tau_{ee}$, where $\tau_{ee}$ is the exchange time between electrons of opposite spin, schematically shown in Fig.1.1. It can be shown (D'Amico and Vignale (2000)) that there is a reduction of the spin diffusion constant $D_s$ relative to the electron diffusion constant $D_e$ given by:

$$D_s = D_e \frac{\tau_{ee}}{\tau_{ee} + \tau_m} \tag{1.5}$$

This Coulomb drag can be seen as a friction between the currents $\vec{J}_+$ and $\vec{J}_-$ due to a momentum transfer between them during electron-electron collisions. This coupling between spins can be accounted for if Fick's law for diffusion takes the following matrix form:

$$\begin{aligned} \vec{J}_+^{\text{diff}} &= q[D_{++}\vec{\nabla}n_+ + D_{+-}\vec{\nabla}n_-] \\ \vec{J}_-^{\text{diff}} &= q[D_{-+}\vec{\nabla}n_+ + D_{--}\vec{\nabla}n_-] \end{aligned} \tag{1.6}$$

and if the generalized Ohm's law for drift considers a conductivity tensor:

$$\begin{aligned}\vec{J}_{+}^{\text{drift}} &= ([\sigma_{++}] + [\sigma_{+-}])\vec{E} \\ \vec{J}_{-}^{\text{drift}} &= ([\sigma_{-+}] + [\sigma_{--}])\vec{E}\end{aligned} \tag{1.7}$$

Another example of spin-spin coupling may arise due to a spin-dependent density of states via bandgap renormalization (Takahashi et al. (2008)). In general, when a coupling of the form (1.6) and (1.7) exists, the charge and spin diffusion currents cannot be written in their simpler form (1.1) and (1.3). A linear combination of the currents appearing in Eqs.(1.6) and (1.7) leads to the following coupled charge and spin drift-diffusion currents:

$$\boxed{\begin{aligned}\vec{J}_{c}^{\text{diff}} &= q[D_{cc}\vec{\nabla}n + D_{cs}\vec{\nabla}s] \\ \vec{J}_{s}^{\text{diff}} &= q[D_{sc}\vec{\nabla}n + D_{ss}\vec{\nabla}s]\end{aligned}} \tag{1.8}$$

$$\boxed{\begin{aligned}\vec{J}_{c}^{\text{drift}} &= ([\sigma_{cc}] + [\sigma_{sc}])\vec{E} \\ \vec{J}_{s}^{\text{drift}} &= ([\sigma_{sc}] + [\sigma_{ss}])\vec{E}\end{aligned}} \tag{1.9}$$

It is concluded that, as far as diffusion currents are concerned:

1. Spin-spin couplings result in a non diagonal $D_{ij}$ matrix (where $i$ and $j$ are $+$ or $-$), because of which a gradient of $n_+$ affects the diffusive current of $n_-$ and vice versa.

2. Charge-spin and spin-charge couplings originate from non zero values of $D_{cs}$ and $D_{sc}$, respectively, and result in a dependence on the spin (charge) current on the charge (spin) density. Spin coulomb drag generates an asymmetrical charge-spin coupling, since it does not modify charge diffusion ($D_{cs} = 0$), but it does modify spin diffusion via a coupling term $D_{sc} \neq 0$. Band-gap renormalization gives both charge-spin and spin-charge couplings, $D_{cs} \neq 0$ and $D_{sc} \neq 0$.

One element whose direct consequences on spin-polarized transport are yet to be explored is the Pauli Principle, which is a key aspect in the quantum mechanical description of nature. Its basic premise, that two Fermions may not simultaneously occupy the same quantum state, has profound consequences for a number of apparently disparate physical systems (Pauling (1960); Shapiro and Teukolsky (1983)). At high Fermion densities (in

the so-called Pauli blockade regime) it predicts the appearance of a quantum degeneracy pressure that was recently observed under controlled conditions in an atom trap by Truscott et al. (2001), and that manifests itself as an increase of the charge carrier diffusion constant and mobility in solids (Smith (1978)).

This thesis describes a new charge-spin coupling phenomenon ($D_{cs} \neq 0$, $D_{sc} \neq 0$ ) induced by this principle that modifies diffusive spin transport, the key result being that diffusion of photoelectrons depend on their spin orientation in the degenerate regime, creating a novel spin filter effect in a homogeneous semiconductor. The consequences of this coupling between charge and spin transport and its experimental observation will be the main topic of this manuscript, whose structure is the following:

Chapter 2 consists of a discussion of the main physical mechanisms involved in spin injection, transport and detection in semiconductors. This allows for some of the recently discovered spin related phenomena to be discussed, together with a brief description of the experimental techniques that were used for their observation.

Chapter 3 presents a detailed description of the experimental technique used in this work, pointing out the advantages and disadvantages with respect to the other existing methods discussed in Chapter 2. The optical alignment procedure is discussed in the hope to help researchers interested in using this setup in the future. The experimental technique used here might appear "poorly-controlled", or "dirty", as the tightly focused light excitation creates large charge, spin, and temperature inhomogeneities,potentially giving rise to a mixture of several distinct effects. The method that we have followed for dealing with this complexity relies on 3 aspects, each of which being devoted to one chapter.

Chapter 4 presents a detailed characterization of the charge and spin transport properties of a $p^+$-GaAs sample in *nondegenerate* conditions.

Chapter 5 contains an extensive theoretical description of the various effects which are likely to modify spin transport in degenerate conditions: spin-dependent diffusion and mobility, thermoelectric currents, etc.

In Chapter 6, I present the experimental results concerning charge and spin transport in a degenerate, spin-polarized photo-electron gas. These experiments were performed as a function of temperature and power density, and their results will be interpreted using the transport parameters measured in Chapter 4 and solving the equations of Chapter 5. It will be shown that the results can be understood in terms of a spin-dependent diffusion of photoelectrons in the degenerate regime, that is, at low temperature and high photo-electron concentration. Moreover, it is shown that the apparently "dirty" experimental configuration is better adapted than more conventional techniques for investigating the effect of degeneracy on spin transport.

Finally, in Chapter 7 I summarize the most important results of this work, together with proposed experiments that can be done in other systems in which Pauli blockade can have much larger effects at even higher temperatures.

# Chapter 2

# Background on spin transport phenomena in semiconductors

The subject of this thesis is part of a larger research effort; semiconductor spintronics, which has received a lot of attention in the last decades in the hope to exploit the quantum nature of the electron spin as a means for processing information and possibly improve future electronic devices. As such, any physical interaction which modifies spin transport is not only of fundamental interest but also of potential practical importance. In this chapter, I will present, without any pretention to be exhaustive, a selection of the most commonly used optical techniques for studying charge and spin transport in semiconductors together with recently discovered transport phenomena observed with these experiments. They all rely in measuring physical quantities that are proportional to $n$ or $s$. Most of these techniques also rely on the ability to create spin-polarized electrons by light excitation. In a general situation, the continuity equation involving $n_+$ and $n_-$ electrons at the steady state is given by

$$\frac{\partial n_\pm}{\partial t} = g_\pm - \frac{n_\pm}{\tau_e} - \frac{n_\pm - n_\mp}{2T_1} + \frac{1}{q}\vec{\nabla}\cdot\vec{J}_\pm = 0 \tag{2.1}$$

where $g_\pm$ is the creation rate of electrons of spin $\pm$ (by either optical or electrical means), $\tau_e$ is the electron lifetime in the conduction band and $T_1$ is the spin relaxation time. Eq.(2.1) dictates that $n$ and $s$ should satisfy the drift-diffusion equation which, according to Eqs.(1.6) and (1.7), is given by:

$$\begin{aligned}(g_+ + g_-) - n/\tau_e + \vec{\nabla}\cdot[\frac{1}{q}([\sigma_{cc}]+[\sigma_{cs}])\vec{E} + D_{cc}\vec{\nabla}n + D_{cs}\vec{\nabla}s] = 0\\ (g_+ - g_-) - s/\tau_s + \vec{\nabla}\cdot[\frac{1}{q}([\sigma_{sc}]+[\sigma_{ss}])\vec{E} + D_{sc}\vec{\nabla}n + D_{ss}\vec{\nabla}s] = 0\end{aligned} \tag{2.2}$$

where $\vec{E}$ is an electric field, and where $1/\tau_s = 1/\tau_e + 1/T_1$. In the absence of charge-spin coupling mechanisms, Eq.(2.2) simplifies to the usual steady state drift-diffusion equations:

$$\begin{aligned}(g_+ + g_-)\tau_e - n + \vec{\nabla}\cdot[n\mu_e\tau_e\vec{E}] + D_e\tau_e\Delta n = 0\\ (g_+ - g_-)\tau_s - s + \vec{\nabla}\cdot[s\mu_s\tau_s\vec{E}] + D_s\tau_s\Delta s = 0\end{aligned} \tag{2.3}$$

A spatially resolved measurement of $n$ and $s$ under non-homogeneous excitation gives access to the transport parameters $L_e$, $L_s$, $\mu_e\tau_e$ and $\mu_s\tau_s$, where $L_e = \sqrt{D_e\tau_e}$, $\mu_e$, $L_s = \sqrt{D_s\tau_s}$, and $\mu_s$, are the charge and spin diffusion length and mobility, respectively.

## 2.1 Kerr and Faraday microscopy (Spin transport only)

This is a microscopy technique that enables a measurement of the spin diffusion length $L_s$. When combined with time resolution, both the spin relaxation time $\tau_s$ and the spin diffusion constant $D_s$ are accessible (Kikkawa and Awschalom (1999); Henn et al. (2013)). It is based on the Kerr (or Faraday) rotation which is a magneto-optical effect that manifests itself by a rotation of the plane of linear polarization of an incident probe beam after reflection (or transmission) from a magnetized surface. A schematic of the Faraday effect is shown on panel a) of Fig. 2.1. Since the angle of rotation of the probe polarization plane is proportional to the magnetization of the sample, this is a way of probing electron spins in semiconductors with spatial and/or time resolution.

Kerr microscopy, commonly used in GaAs, has allowed for interesting spin-orbit coupling phenomena to be observed for the first time. One of them is the Spin Hall Effect (SHE),

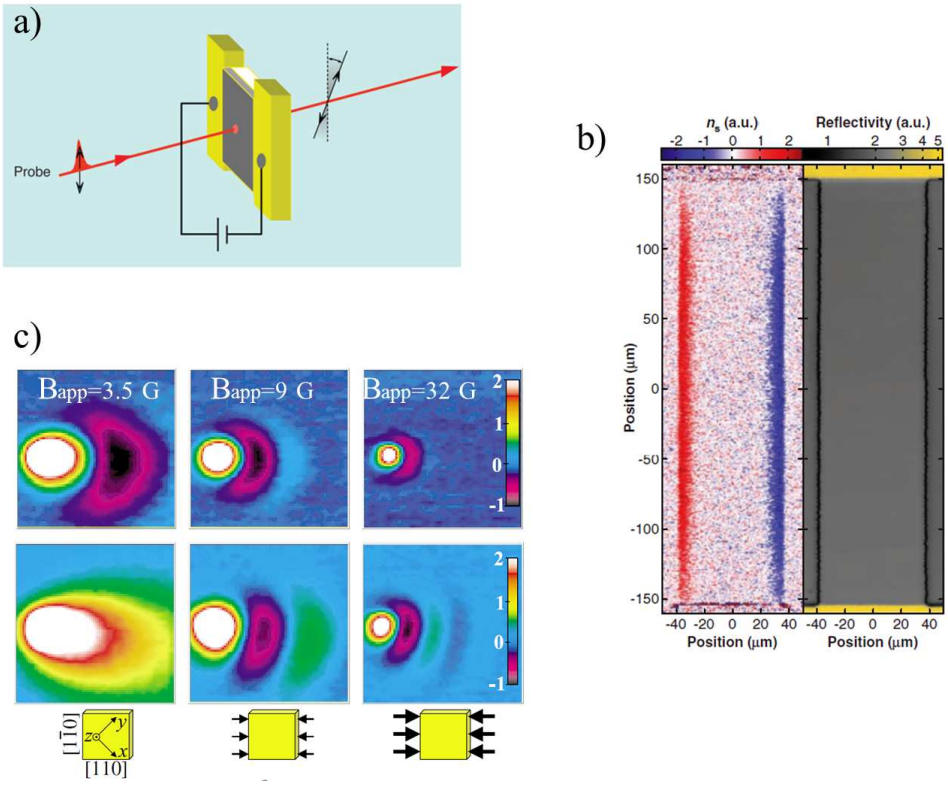


**Figure 2.1:** Panel a) Principle of the Faraday effect (Taken from Awschalom and Samarth (2009)). A linearly polarized probe beam is used to probe the magnetization of a sample. The polarization of the transmitted beam will be rotated with respect to the incident beam by an angle that is proportional to the magnetization of the film. b) Two-dimensional images of spin density $s$ and reflectivity, for a GaAs sample at $T = 30$ K and $E = 100$ V/cm. The Kerr signal at the edges of the sample is signature of the Spin Hall Effect. Taken from Kato et al. (2004). c) $80 \times 80$ $\mu$m$^2$ images of spin flow ($E = 10$ V/cm) in n-GaAs at 4 K with increasingly applied in-plane magnetic field (top) or strain field (bottom). Modified from Crooker and Smith (2005).

predicted more than 40 years ago by D'yakonov and Perel (1971a) but whose experimental confirmation came 30 years later, as reported by Kato et al. (2004). As shown in panel b) of Fig.2.1, a uniform (as verified from the reflectivity image of the sample) unpolarized electron current leads to a spatial separation of electrons with opposite spin due to an asymmetric Mott scattering off unpolarized impurities in the prescence of the spin-orbit interaction. This separation leads to an out of plane spin accumulation at the edges of the sample detected by a Kerr rotation near the boundaries. The sample was a bar shaped 2 $\mu$m thick, Si doped n-GaAs ($n = 3 \times 10^{16}$ cm$^{-3}$), the temperature was $T = 30$ K, and the magnitude of the Kerr rotation at the boundaries was 2 $\mu$rad, which corresponds to a spin polarization of $\sim 0.1$ %, estimated by fitting the spatial dependence of the Kerr signal

with a spin drift-diffusion equation in the steady state. The small magnitude of this effect, together with the fact that the SHE does not lead to a net transverse charge imbalance, explains why the first observation came 40 years after the theoretical prediction.

Another beautiful experiment using Kerr microscopy was performed by Crooker and Smith (2005) in which a spin density is optically generated by a circularly polarized laser spot (this process of optical pumping will be detailed in sec.2.2) of diameter $\phi = 4$ $\mu$m at an energy 1.58 eV on a 1 $\mu$m thick, Si doped n-GaAs ($n = 1.5 \times 10^{16}$ cm$^{-3}$) sample. These electrons drift and diffuse laterally under the influence of an applied electric field. 2D images of the out of plane component of the electron spin were obtained at 4 K by measuring the Kerr rotation of the reflected probe (also focused to a 4 $\mu$m spot). Combined with an ultrafast technique that gives a spin lifetime of $\tau_s = 120$ ns, the authors find a spin diffusion constant of $D_s = 3$ cm$^2$/s, and therefore, a spin diffusion length of $L_s = 6$ $\mu$m.

In the experiment of Crooker and Smith (2005), an electric field is applied along the [110] crystallographic direction. The top inset of panel c) of Fig.2.1 shows $80 \times 80$ $\mu$m$^2$ images of the spin flow with an electric field of $E = 10$ V/cm and increasing values of an applied in-plane magnetic field $\vec{B}_{\text{app}}//[1\overline{1}0]$. Spin precession under the influence of this field is evident from the oscillations of the Kerr rotation in the direction of the electric field. However, the coherence length is limited to just 1 precession period, especially when this latter becomes comparable to the spin diffusion length. This is a consequence of the randomizing nature of diffusion ; electrons with different wavevectors at the same point in space had precessed over different times. The bottom inset of the same panel shows that the spatial coherence of spin flows persists over many precession cycles when the spins are manipulated with a strain instead of a magnetic field. A uniaxial stress along [110] generates an in-plane effective magnetic field along $[1\overline{1}0]$ which is proportional to $\mid \vec{k} \mid$. This is a consequence of the spin-orbit interaction, and it correlates precession frequency with electron velocity, and therefore position. This strain-controlled precession of the spin ensemble is an example that shows that manipulation of spin polarized electrons in a semiconductor is possible even in the absence of magnetic fields or ferromagnetic contacts, which are complicated to implement in future spintronic devices.

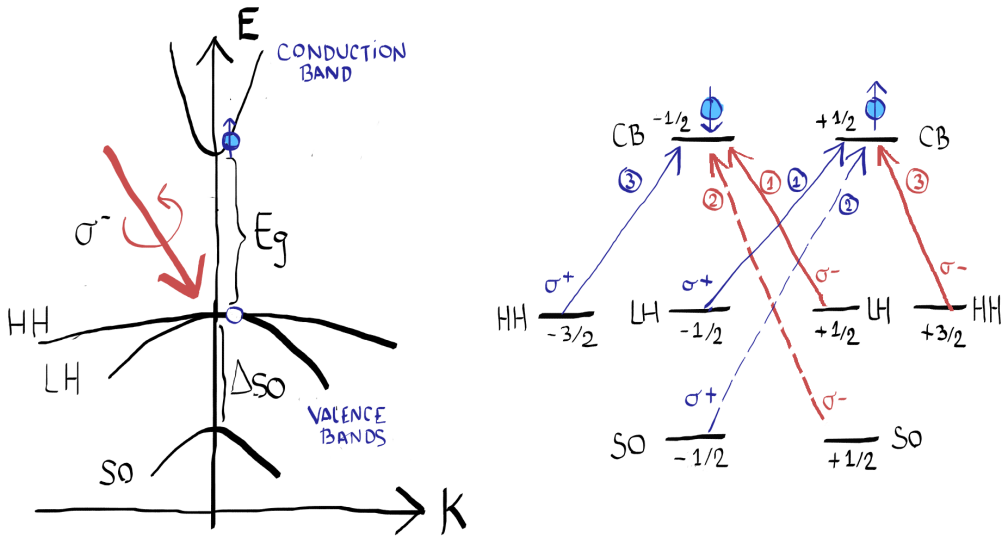


**Figure 2.2:** Left: Dispersion relations near the centre of the Brillouin zone in GaAs, a direct gap III-V semiconductor that crystallises in the zinc-blende structure. The valence bands are composed of the heavy-hole (HH), the light-hole (LH), and the split-off band (SO). At $k = 0$, the HH and LH bands are degenerate, whereas the SO band lies at an energy $\Delta_{SO}$ below the top of both HH and LH bands. A circularly polarized photon with energy above bandgap $E_g$ and below $E_g + \Delta_{SO}$ will transfer an electron from the valence band to the conduction band that will have a preferential spin orientation. On the right, at $k = 0$ the states are labeled by their $m_j$ quantum number, the projection of the total angular momentum on the axis of propagation of light. The optical selections rules for absorption of right $\sigma^+$ ($\Delta m_j = +1$) and left $\sigma_-$ ($\Delta m_j = -1$) circularly polarized light are shown by blue and red arrows, respectively, the circled numbers being their relative transition probabilities. The up and down arrows in the conduction band indicate the two possible spin orientations after absorption.

## 2.2 Optical spin orientation

In the experiment of Crooker and Smith (2005) discussed above, a spin density was created in GaAs by optical means. Lampel (1968) showed that it is indeed possible to induce a non equilibrium spin polarization of electrons in a non-magnetic semiconductor ($g_+ \neq g_-$ in Eq.(2.1)) via the absorption of circularly-polarized light that couples initial states in the valence band to final states in the conduction band that have a preferential spin orientation. In III-V direct bandgap semiconductors such as GaAs, the optical selection rules are relatively simple (see Fig. 2.2) and this makes photoluminescence measurements possible.

For example, absorption of a right ($\sigma^+$) or left ($\sigma^-$) circularly polarized photon will only induce transitions preserving the projection of the photon angular momentum along the

propagation axis $\Delta m_j = \pm 1$. The possible optical transitions and their relative probabilities are shown as arrows and numbers, respectively, in Fig. 2.2. It is seen that if the energy $h\nu$ of the incident photons is restricted to the interval $E_g < h\nu < E_g + \Delta_{SO}$, then transitions from the split-off (SO) band are not possible. According to the optical selection rules, the creation rates $g_\pm$ appearing in Eq.(2.2) for a $\sigma^\pm$ polarized light excitation satisfy $g_\mp = 3g_\pm$, so that the initial spin polarization will be $\mathscr{P}_i = (g_+ - g_-)/(g_+ + g_-) = \mp 0.5$ (Meier and Zakharchenya (1984)). For GaAs, $\Delta_{SO} = 0.34$ eV and $E_g = 1.42$ eV at room temperature, so near infrared laser excitation (in our experiments, $h\nu = 1.59 \pm 0.01$ eV) can be used to excite only the light-hole (LH) and heavy hole (HH) bands.

It is pointed out that the absorption process described in Fig.2.2 is reversible in time, so that relaxation of conduction electrons by spontaneous emission will generate a luminescence light whose degree of circular polarization is directly proportional to the spin density $s$. This will be discussed in more detail in sec.3.1.

## 2.3 Transient charge and spin gratings

A very elegant method for studying both charge and spin transport was demonstrated by Cameron et al. (1996), and it consists in measuring the diffraction dynamics produced by an optically induced grating in a semiconductor. These gratings are formed when two coherent, non-collinear pulses of equal intensity interfere to produce a spatial modulation of the refraction index via carrier photoexcitation. Different physical mechanisms involving photoexcitation can modify the refractive index, such as band filling, band-gap renormalization, free-carrier absorption, or many-body effects.

As seen from panel a) of Fig. 2.3, when the two beams are linearly polarized along the same direction, they will produce an intensity interference pattern on the sample. The number of excited carriers will have a sinusoidal variation in space $n(x) = \frac{n^{max}}{2}(1 + \sin(qx))$, with wavevector $q = \frac{\Lambda}{2\pi}$, which can be varied by changing the angle of incidence $\vartheta$ of the beams, since $\Lambda = \frac{\lambda}{2\sin\vartheta}$. On the other hand, if the two incident beams have crossed polarizations, the light amplitude in the sample will be uniform but a sinusoidal modulation of the light polarization, changing from left ($\sigma^-$) to right ($\sigma^+$) circular polarization, will be formed.

### 2.3. Transient charge and spin gratings

In this case, the optical pumping selection rules of sec.2.2 dictates that there will be a sinusoidal variation of the photoelectron spin density $s = s^{max}\sin(qx)$, with the same wavevector $q$.

A modulated electron density will modify the refractive index of the sample that is independent of incoming light polarization. In contrast, a spin density modulation creates a circular optical birefringence, that is, a different refractive index for left and right circularly polarized light. In both cases, an incident probe beam will be diffracted by the sample. This diffraction is used to monitor the temporal evolution of the optically imprinted charge or spin wave. In panel c) of Fig.2.3, a possible configuration for detection is shown, where two linearly polarized probe beams are used. Their polarizations should be parallel or crossed in order to detect a charge or a spin grating, respectively. In any case, the reflection of the probe 1 will interfere with the first order diffraction of probe 2. If the phase between these two beams is modulated at a given frecquency, heterodyne detection can be implemented in order to measure the amplitude of the diffracted probe as a function of time delay with respect to the pumps. In a linear regime, both the charge and the spin grating will produce a diffracted signal whose magnitude is proportional to $n^{max}(t)$ and $s^{max}(t)$, respectively.

The (either charge or spin) grating decay rate $\gamma$ will be determined by a combination of the lifetime $\tau$ and of diffusion outwards from concentration peaks, according to the solution of the time-dependent diffusion equation (Cameron et al. (1996)):

$$\gamma = \frac{1}{\tau} + q^2 D \tag{2.4}$$

By changing the grating wavevector $q$ (or equivalently, the angle of incidence of the beams), it is possible to separate diffusion from recombination and relaxation. In panel a) of Fig. 2.4, the decay of a spin grating at 15 K on a semi-insulating GaAs sample is shown for different values of the wavevector $q$, as obtained by Weber et al. (2011). This permits to measure the spin diffusion constant $D_s$ by comparing the $q^2$ dependence of $\gamma$ with Eq.(2.4). This is shown on panel b) of Fig.2.4.

As discussed in Chapter 1, since charge and spin are transported by the same particle, it

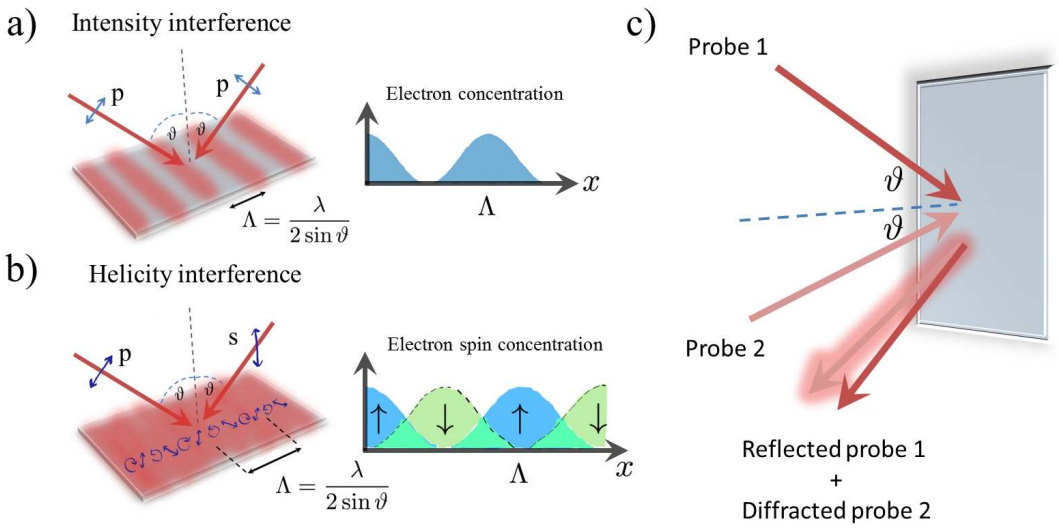


**Figure 2.3:** Principle of the transient grating technique. Two non-collinear pulses interfere at the sample, creating either a charge density grating (panel a), or a spin density grating (panel b). As shown in panel c), after a certain time after the excitation, two probe beams are used in order to detect the interference between the diffracted beam of probe 2 with the reflection of probe 1.

has been widely assumed that diffusion of both charge and spin densities are governed by the same diffusion constant, i.e $D_e = D_s$. But as pointed out by D'Amico and Vignale (2000) and confirmed experimentally by Weber et al. (2005), the assumption $D_e = D_s$ fails to take into account electron-electron collisions, that although they respect momentum conservation, and therefore, charge currents, they do not conserve spin currents (an schematic of this situation is shown in Fig.1.1). This predicts a reduction of the spin diffusion constant $D_s$ relative to the electron diffusion constant $D_e$ given by Eq.(1.5). Panel c) of Fig. 2.4 shows the measured $D_e/D_s$ by Weber et al. (2005) as a function of temperature for a (100) GaAs multiple quantum well (12 nm thick) separated by 48 nm layers of $Ga_{0.7}Al_{0.3}As$ doped with different Si concentrations, corresponding to Fermi temperatures of $T_F = 400$ K (red), 220 K (green) and 100 K (blue). The prediction of Eq.(1.5) corresponds to the dotted line; $D_s$ is found to be always smaller than $D_e$ in the range $40-300$ K.

The spin grating technique has been also used to explore very interesting phenomena involving the spin orbit interaction. Relativity dictates that, in the presence of an electric field, the spin and momentum states of an electron are coupled. In a III-V semiconductor (such as GaAs), whose crystal lattice lacks inversion symmetry, the electron experiences a varying microscopic electric field during its movement. In his reference frame, a mag-

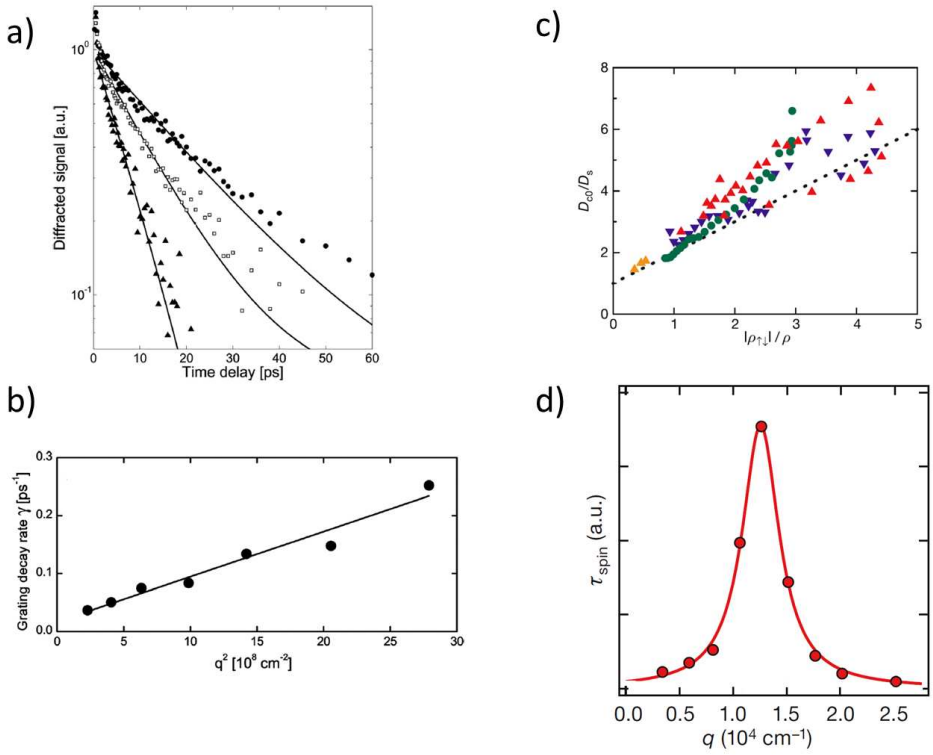


**Figure 2.4:** Panel a) Decay of a spin grating at 15 K in semi-insulating GaAs for different values of the grating wavevector, $q = 2.01, 3.14$ and $4.53$ $\mu$m$^{-1}$ (slowest to fastest). b) Decay rate of the spin grating vs $q^2$ at 15 K. The line is a fit to the form of Eq.(2.4), indicating diffusive behavior with $D_s = 78$ cm$^2$/s. Taken from Weber et al. (2011). c) Supression of the spin diffusion constant $D_s$ relative to the electron diffusion constant $D_e$ for samples with $T_F = 400$ K (red), 220 K (green) and 100 K (blue). The dashed line has unity slope and intercept, indicating the prediction of Eq.(1.5). For points above the line, small many-body effects are present. Taken from Weber et al. (2005). d) Lifetime of a spin diffraction grating in a [001] GaAs quantum well, exhibiting a peak for a non-zero value of the grating wavevector $q$, in high contrast with diffusion dynamics. Modified from Koralek et al. (2009).

netic field appears that leads to precession of the electron spin. This causes a splitting of the conduction band along particular crystal momenta $\vec{k}$, that can be characterized by an effective Dresselhaus magnetic field whose magnitude and direction depends on $\vec{k}$, $\vec{B}_D = \vec{B}_D(\vec{k})$ (Dresselhaus (1955)). In a diffusive regime, this spin-orbit field is responsible for the D'yakonov-Perel spin dephasing mechanism (D'yakonov and Perel (1971b)). Since the effective magnetic field depends on the electron wavevector $\vec{k}$, after every collision event the precession axis and frequency for a given electron will change in a random manner, leading to dephasing of the spin orientation during diffusive transport.

In heterostructures or quantum wells, in addition to this Dresselhaus field, there is also a Bychkov-Rashba field $\vec{B}_R$, due to a macroscopic electric field associated to an inversion asymmetry of the confinement potential. Therefore, the Rashba field can be tuned so that it exactly cancels the Dresselhaus field along some particular directions, supressing the spin dephasing mechanisms associated with the spin-orbit interaction (Wang et al. (2013b)). Using the spin grating technique, this supression of spin relaxation was demonstrated in GaAs quantum wells grown on the [001] direction by Koralek et al. (2009). The spin-orbit interaction is highly suppressed for a particular, non-zero value of the grating wavevector $q$, as shown in panel d) of Fig.2.4. This causes a long-lived spin wave to decay over time scales much longer than predicted by diffusive dynamics alone. This is called the persistent spin helix.

While the transient charge and spin grating technique is a very powerful method, it is difficult to implement, and more importantly, it is not adapted to study simultaneous diffusion of both charge and spin densities. For example, a spin grating will not be coupled with neither hole or electron diffusion, since their concentration is constant in space. I will show in Chapter 5 that degeneracy has a larger effect on spin diffusion when both couplings are present.

## 2.4 Photoelectrical measurements

Combination of electrical and optical measurements may also be used to obtain valuable information about spin transport phenomena. For example, the SHE may give rise to a measurable transverse voltage when the electrons are spin polarized, $n_+ \neq n_-$. Very recently, optically pumped polarized electrons in a Si doped n-GaAs ($n = 1 \times 10^{16}$ cm$^3$) Hall bar were used to electrically detect and control the SHE. Okamoto et al. (2014) showed that when the electrons are transferred from the $\Gamma$ to the $L$ valley by a sufficiently high electric field, the magnitude of the SHE is enhanced by a factor of 40, due to the much larger spin-orbit coupling in the $L$ valley. This is illustrated in panel a) of Fig. 2.5.

An intrinsic mechanism for the SHE was also proposed by Murakami et al. (2003) and by Sinova et al. (2004), in which spin deflection can occur directly from relativistic band

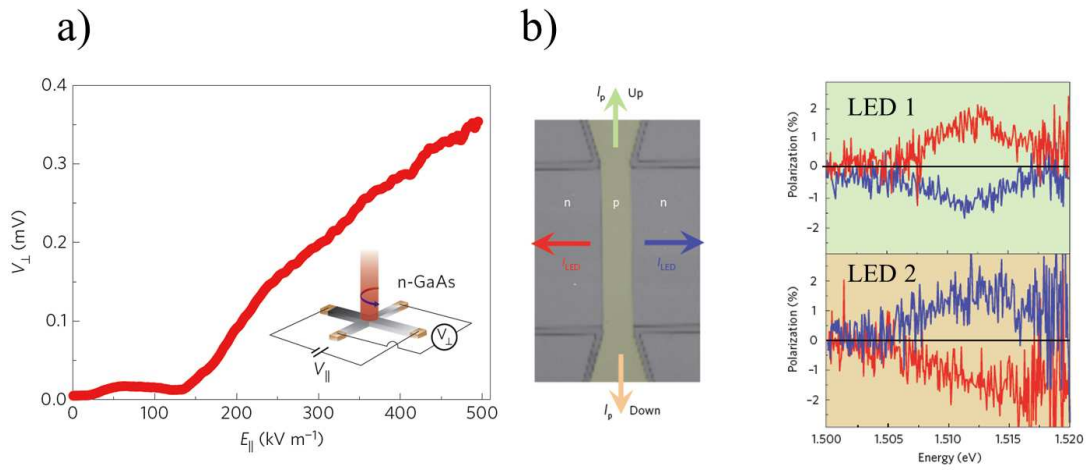


**Figure 2.5:** a) The optically induced SHE voltage as a function of the longitudinal electric field in a n-GaAs layer shows a 40-fold increase when transfer from the Γ to the $L$ valley occurs. Taken from Okamoto et al. (2014). b): electron microscope image of a microdevice with symmetrically placed p–n diodes at both edges of a 2D hole gas channel. At the right, the emitted light polarization of recombined light in each p–n junction is shown for the two possible directions of the current flow. Taken from Wunderlich (2010)

structure without any Mott scattering being involved. This was observed by Wunderlich et al. (2005), this time by measuring the degree of circular polarization coming from a p-n junction at opposite edges of a p region, as shown in panel b) of Fig. 2.5. The signal reached $\mathscr{P} = 1$ % at 4.2 K in this experiment. The SHE and the inverse SHE (Jungwirth et al. (2012)) has been used as an electric means of generating and probing spin currents in nonmagnetic systems. However, its magnitude is still too small to construct any practical device.

Another example of combined optical and electrical investigation of spin transport is the electrical manipulation of the Bychkov-Rashba effect. On [111] oriented quantum wells, and in contrast with the [001] quantum wells in which the spin helix was observed, compensation of the Dresselhaus and the Rashba fields may occur for all possible directions, leading to strongly enchanced spin relaxation times. This was demonstrated recently by Wang et al. (2013b) and by Hernandez-Minguez et al. (2014).

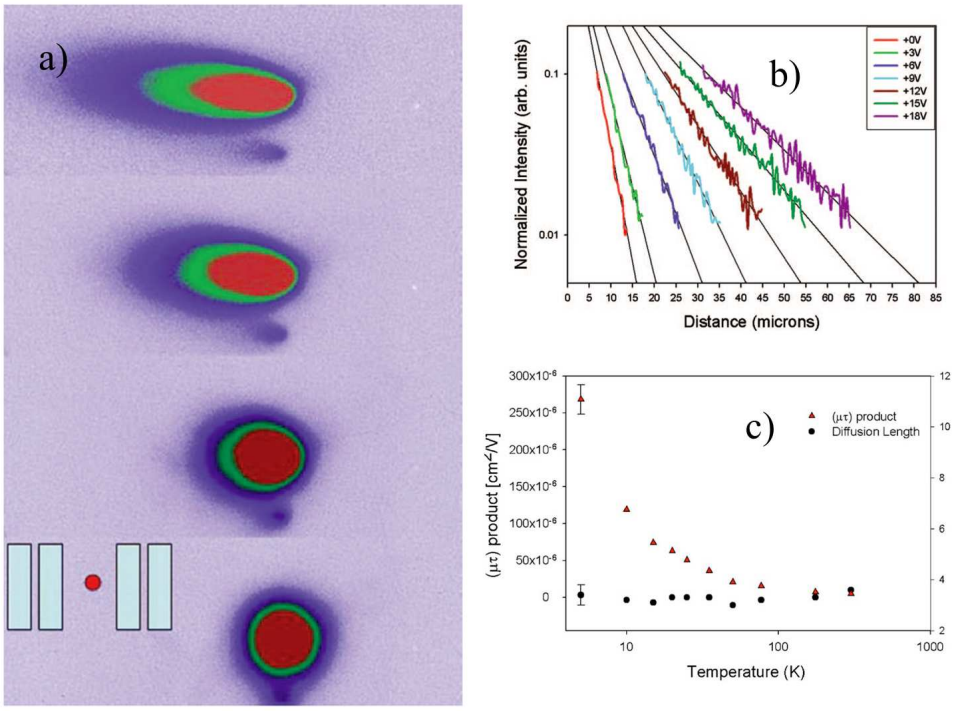


**Figure 2.6:** Panel a) shows the spatially-resolved steady state luminescence of a double heterostructure representing drift and diffusion of electrons under an applied electric field in p type GaAs. b) Semilogarithmic plot of the data along the applied electric field revealing an exponential decay that is due to both drift and diffusion. c) The $\mu_e \tau_e$ product measured as a function of sample temperature. All figures taken from Luber et al. (2006).

## 2.5 Luminescence imaging

Although luminescence imaging has been mostly used in the past to investigate charge rather than spin transport, it will be described here since it will serve as a basis for our spin transport studies. The principle of this technique is based on the linear relationship between the luminescence intensity and the total density of minority carriers in sufficiently doped semiconductors. A technique was developed by Luber et al. (2006) to measure the minority carrier charge diffusion length $L_e$. In their experiment, a 20 keV electron beam is tightly focused (diameter less than 50 nm) by a scanning electron microscope (SEM) on a GaInP (25 nm)/p-GaAs (0.1 $\mu$m)/GaInP(50 nm) double heterostructure with Be as a dopant at a density $p = 5 \times 10^{18}$ cm$^{-3}$. This electronic beam excites minority electrons in the conduction band at steady state and an optical microscope coupled to a CCD camera is then used to image the luminescence.

## 2.5. Luminescence imaging

Patterned Ti:Au contacts were used to apply an electric field. Images of the steady-state luminescence for different values of the electric field $E$ are shown on panel a) of Fig.2.6. It can be shown that the solution of the drift-diffusion equation (2.3) (see appendix 8.1) out of the excitation area dictates that the electron concentration along the direction $x$ of the electric field will decay exponentially, according to $n \propto e^{Cx}$, with

$$C = \left(\frac{q}{2k_BT}\right) E - \sqrt{\left(\frac{qE}{2k_BT}\right)^2 + \frac{1}{L_e^2}} \tag{2.5}$$

provided that the decay length is larger than the sample width, $1/C >> d$. This exponential decay is experimentally verified, as shown in panel b) of Fig.2.6. If the temperature is known, the only fitting parameter is the electron diffusion length $L_e = \sqrt{D_e\tau_e}$. The product $\mu_e\tau_e$, where $\mu_e$ is the minority electron mobility, is then obtained via the Einstein relation

$$D_e = \mu_e k_B T/q \tag{2.6}$$

and shown on panel c) of Fig.2.6, as well as the measured diffusion length as a function of sample temperature. At room temperature, Luber and co-workers found an electronic diffusion length of $L_e = 3.6$ $\mu$m at zero electric field that gradually decreases down to $L_e = 3.1$ $\mu$m for an electric field of $E = 522$ V/cm, attributed to heating of the electron gas.

This technique can be combined with time-resolved measurements, such as time-resolved photoluminescence (TRPL), in order to obtain the electronic lifetime and the diffusion constant. This was used by Luber et al. (2006) to determine the electron mobility for their sample, $\mu_e = 1150$ cm$^2$/Vs at 300 K. This value is close to previous measurements on bulk GaAs for similar doping (Harmon et al. (1993); Beyzavi et al. (1991); Colomb et al. (1992)), and as I will show on sec.4.2.5, slightly lower than the mobility obtained for our 3 $\mu$m thick p-GaAs sample which has a lower doping of $p = 10^{18}$ cm$^{-3}$. Notice also that since holes do not freezeout for this doping levels (Lovejoy et al. (1995)), the temperature dependence of $\tau_e$ should be weak and therefore the dramatic increase of the $\mu_e\tau_e$ product shown on panel c) of Fig.2.6 reveals a $\sim 1/T$ dependence of the mobility, a similar result to that observed by Beyzavi et al. (1991). As I will discuss later in sec.4.2.5, this behaviour is not completely understood.

## 2.6 Conclusions of this chapter

A non-equilibrium, spin-polarized electron density can be injected in a non-magnetic semiconductor by either electrical or optical means (optical pumping). In order to study the transport properties of these electrons, different techniques may be used.

Despite being the most commonly used, none of the optical techniques presented in this chapter is particularly adapted to a simultaneous study of charge and spin diffusion and, therefore, to the observation of the novel charge-spin coupling mechanism induced by the Pauli principle. For example, Kerr/Faraday microscopy is only sensitive to the spin density, lacking spatial information of the charge density, whereas luminescence imaging, as described above, gives the exact opposite situation. While the transient grating technique, which is an optical analog similar to the Shockley-Haynes experiment, allows for the lifetime and diffusion constants of each species to be determined, charge and spin diffusion are resolved in separate measurements, with either charge or spin spatial gradients, but not both at the same time. It is seen therefore from Eq.(2.2) that the non diagonal diffusion terms vanish in these grating experiments, making it difficult to experimentally detect such couplings.

In the next chapter I present a polarized luminescence microscopy technique that, despite its simplicity, is well adapted to study charge and spin couplings in semiconductors.

# Chapter 3

# Experimental technique: polarized microluminescence imaging

In this chapter I will present our experimental technique which will be used to create and spatially monitor a charge and a spin density in steady state. This is an advantage with respect to luminescence imaging or Kerr/Faraday microscopy, both discussed in Chapter 2, since with these techniques either charge or spin are resolved, but not both at the same time. While our technique does not have temporal resolution, it can be combined with time-resolved measurements in order to determine the relevant charge and spin lifetimes and diffusivities. Even if the transient grating technique allows, in principle, to determine all the relevant transport parameters (except from mobilities), the experimental setup presented here has the advantage of being significantly simpler and, moreover, charge and spin gradients can be studied at the same time under the same experimental conditions. This is of crucial importance to study charge and spin coupling mechanisms.

## 3.1 Optical spin detection

Since the selection rules for optical pumping shown in Fig.2.2 also apply for emission of photons by the electrons in the conduction band, the degree of circular polarization of the luminescence provides a means of monitoring the ensemble electron spin polarization $\mathscr{P}$. For example, a $n_{\pm}$ electron in the conduction band will emit a $\sigma_{\mp}$ photon with a probability 3 times larger than that of emitting a photon of opposite helicity. It is easy to show then that if the luminescence is analyzed into its $\sigma^+$ and $\sigma^-$ components, then,

the charge and the spin density can be written in terms of the measured intensities $I^{\pm}$ of the $\sigma^{\pm}$ components of the luminescence [1]:

$$\begin{aligned} I_s &= (I^+ + I^-) = Kn \\ I_d &= (I^+ - I^-) = 0.5Ks \end{aligned} \tag{3.1}$$

where $K$ is a constant, and $I_s$ ($I_d$) stands for sum (difference) image. From Eq.(3.1), it is seen that the degree of circular polarization of the luminesence $\mathscr{P}^{\text{lum}}$ will be related to the electron spin polarization $\mathscr{P} = s/n$ according to:

$$\mathscr{P}^{\text{lum}} = \frac{I_d}{I_s} = \frac{I^+ - I^-}{I^+ + I^-} = \mp 0.5\ \mathscr{P} \tag{3.2}$$

## 3.2 Principle of the method

The experimental procedure used in this work is the steady-state optical orientation (or optical pumping) of spin polarized conduction electrons and the spatial resolution of the resulting polarized luminescence in p-GaAs (Favorskiy et al. (2010)). The transport measurement can be divided into three main processes: i) under conditions of tightly focused optical excitation with circularly polarized light (typical radius of $\omega = 0.5\ \mu$m), an inhomogeneous distribution of spin-polarized photo-electrons is promoted to the conduction band near a point that we call $r = 0$. Light excitation is represented by the red arrow in Fig.3.1 and the initially photoexcited electron density is represented by the red profile; ii) these electrons diffuse laterally to regions of lower concentration. In consequence, the charge and the spin densities will spread outwards from the excitation spot, as represented by the blue curves (full and dotted, respectively) in Fig.3.1, iii) the electrons eventually relax to equilibrium by spontaneous emission of light, represented by the blue arrows in Fig.3.1. The total luminescence intensity as a function of position $r$ is proportional to $n(r)$, whereas the difference image defined in Eq.(3.1) is proportional to $s(r)$.

[1] Because of the bimolecular nature of the luminescence, this is true provided that the photoelectron concentration is smaller than $N_A$, the volume density of dopants in a p-type sample

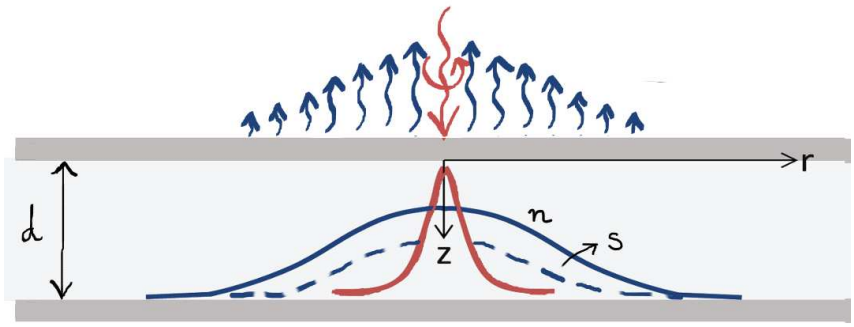


**Figure 3.1:** Principle of the experiment: A thin sample (thickness $d$ comparable to the charge and spin diffusion lengths) is excited at $r = 0$ by tightly focused, above bandgap light ($+z$ facing arrow). An image of the bandgap emission is monitored ($-z$ facing arrows). Combinations of the $\sigma^+$ and $\sigma^-$ components of this image reveals charge and spin diffusion within the sample, whose spatial distribution in steady state is represented by the full and dotted blue curves, respectively.

### 3.2.1 Remarks

- In order to reveal diffusion of charge and spin densities, it is necessary to create a local imbalance of $n$ and $s$ in a radius smaller than the diffusion lengths $L_e$ and $L_s$. This can be done by optically injecting electrons with a laser beam of Gaussian radius $\omega$, such that $\omega < L_e, L_s$. Typical spin diffusion lengths in doped GaAs are of the order of several $\mu$m, so a sub $\mu$m excitation is necessary. This is close to the diffraction limit $\lambda/(2\text{NA})$, where NA is the numerical aperture of the system. By using near infrared light with energy $h\nu = 1.59$ eV (slightly larger than the bandgap energy of GaAs, as mentioned in sec.2.2) and an objective of numerical aperture NA $= 0.6$, one finds $\lambda/(2\text{NA}) = 0.65$ $\mu$m. The resolution is comparable to that achieved in Faraday or Kerr microscopy.

- Since vertical diffusion over a distance larger than the effective depth of field $f'$ will cause a defocused luminescence image, this technique is clearly limited to sufficiently thin samples whose thickness $d$ is such that $d \leq f'$. The depth of field of a high numerical aperture ojective is given by $f = \lambda/\text{NA}^2$, so that $f' = fn$, where $n \approx 3.29$ is the refractive index of GaAs. For a NA$= 0.6$ objective one obtains $f' \sim 7.1$ $\mu$m, which is more than two times larger than the thickness $d = 3$ $\mu$m of our samples, which are discussed in sec.4.1.

- An electron inside the sample will emit light in all possible directions. However, only those photons emitted at an angle $\vartheta_{max}$ respect to the normal will manage to escape the sample. This angle is determined by total internal reflection at the GaAs-air interface, so that $\vartheta_{max} = \sin^{-1}(1/n) \approx 18°$. Since this is a small angle, at a given point on the sample surface it is supposed that the total charge and spin intensities defined by Eq.(3.1) are actually vertical averages of the form:

$$I_s(r) = K \int_0^d n(r,z) e^{-\alpha_l z} dz \tag{3.3}$$

$$I_d(r) = 0.5K \int_0^d s(r,z) e^{-\alpha_l z} dz \tag{3.4}$$

where $r$ is the radial coordinate on the image plane, $z \leq d$ is the depth coordinate (see Fig.3.1) and $\alpha_l \approx (1/3\ \mu\text{m})^{-1}$ is the absorption coefficient at the luminescence energy (Blakemore (1982)).

## 3.3 Experimental setup

Fig.3.2 shows an artist's rendition of a modified Nikon commercial microscope, whose first implementation was reported by Favorskiy et al. (2010). It has significantly evolved since. An externally collimated laser beam enters the excitation arm (left side of the microscope) and its size is adjusted by a beam expander in order to cover the entirety of the rear aperture objective and to minimize the size of the laser spot on the sample. The laser intensity may be adjusted by selecting an appropiate optical density filter, and is linearly polarized ($\pi_s$ polarization with respect to the beamsplitter surface) before passing through a variable retarder ($0 - \lambda$ range). The incident linear polarization plane forms an angle of 45° with respect to the fast and slow axes of the retarder. By choosing an appropriate retardation, the laser polarization at the sample can be switched between $\pi_s$, $\sigma^+$, $\pi_p$ and $\sigma^-$ polarization. The passage between circularly ($\sigma$) and linearly ($\pi$) polarized light is important because it permits a comparision of electron diffusion of polarized and un-polarized electrons, respectively, under the same excitation conditions. This will be discussed in sec. 6.2.

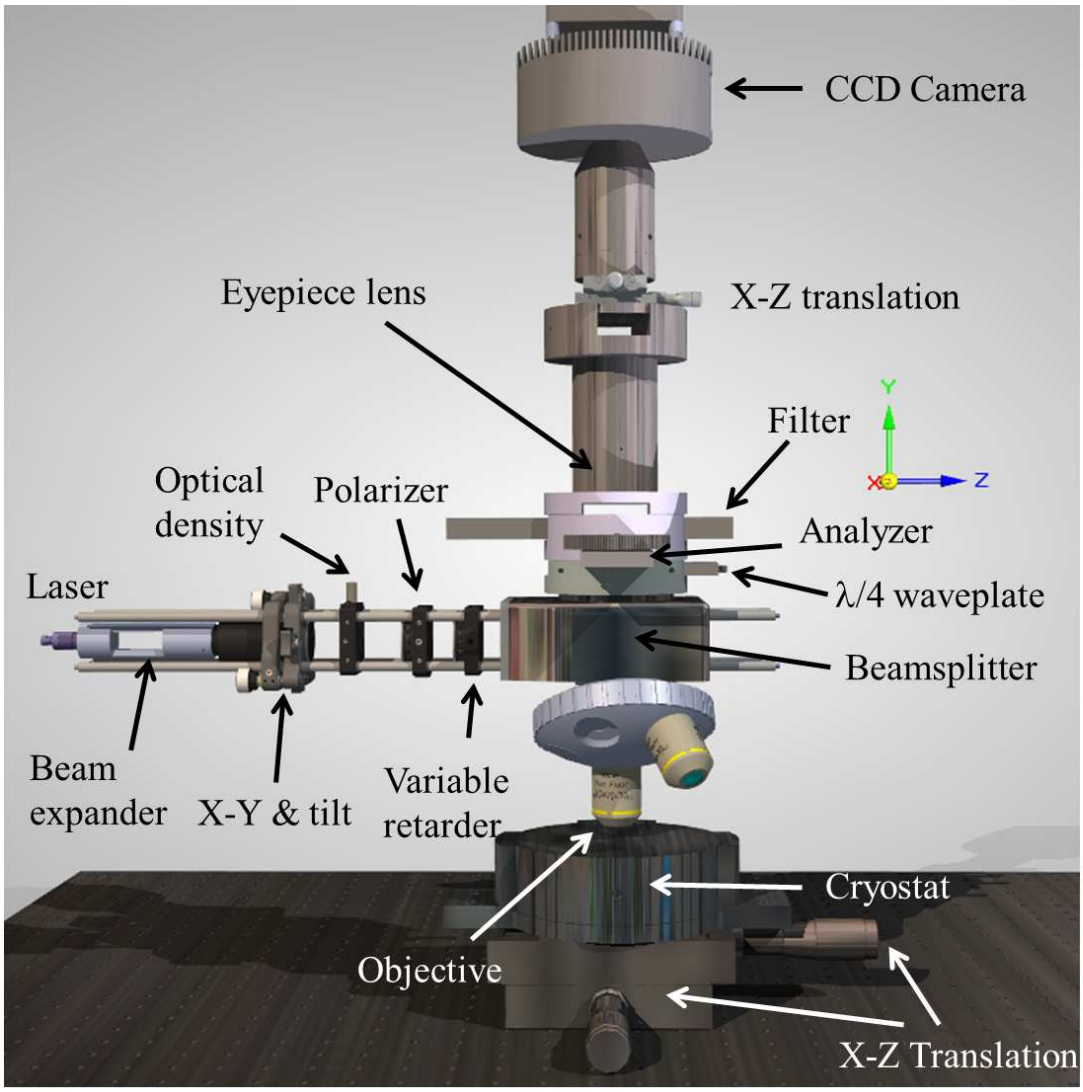


**Figure 3.2:** Schematic of the microscope used for imaging polarized luminescence. The excitation arm allows for a linearly or circularly-polarized laser beam to be focussed to a diffraction limited Gaussian spot of radius $\omega = 0.6$ $\mu$m by a x50 objective. The luminescence, which is analyzed into its $\sigma^+$ and $\sigma^-$-polarization components thanks to the rotation of a $\lambda/4$ waveplate followed by a fixed analyzer, is imaged with a CCD camera once the laser is properly filtered.

After reflection by the beamsplitter, the laser is focused by a x50 objective into a diffraction limited gaussian spot of radius $\omega = 0.6$ $\mu$m. The sample is kept in a cryostat where the controlled transfer of liquid Helium from a dewar into a heat exchanger adjacent to the sample holder is used to vary the temperature in the range $5 - 300$ K. The objective has a compensation ring in order to correct the aberrations caused by the 1 mm thick BK7 window of the cryostat. Luminescence coming from the sample is analyzed by a quarter wave plate followed by an analyzer. The mounting in which the quarter waveplate is fixed can be manually removed, turned around, and reinserted in order to obtain the $\sigma^+$

and $\sigma^-$ components of the luminescence. Once the reflected laser beam is removed by an appropiate filter, the resulting image is focused by the eyepiece into a CCD camera placed in the ocular focal plane (focal length of 200 mm). Since the size of a pixel is 9 $\mu$m, the spatial resolution obtained with the X50 objective is of 0.16 $\mu$m/pixel. There is also the possibility to replace the CCD camera by a multimode optical fiber connected to a spectrometer, which permits to monitor the polarized luminescence spectrum as a function of position in the image plane, with a maximum resolution of $\sim 1\ \mu m$. The main optical properties of the different components of this setup is presented in Table.3.4.4.
In order to get rid of residual birefringence in the optical path, both $\sigma^+$ and $\sigma^-$ polarized components are, in turn, used to excite the sample and the resulting four images, denoted by $\sigma^{++}$,$\sigma^{+-}$,$\sigma^{--}$, and $\sigma^{-+}$, are combined to form a sum image

$$I_s = [\sigma^{++} + \sigma^{+-} + \sigma^{--} + \sigma^{-+}]/2 \tag{3.5}$$

and a difference image

$$I_d = [\sigma^{++} - \sigma^{+-} + \sigma^{--} - \sigma^{-+}]/2 \tag{3.6}$$

that correspond to Eqs.(3.3) and (3.4), respectively. A spatial profile of the luminescence polarization is obtained by the ratio of these two images (Eq.(3.2)).

### 3.3.1 Key improvements

I spent a significant part of my first months of work in the lab in characterizing and improving the optical performance of the microscope. At the moment of its first setup (Favorskiy et al. (2010)), it was possible to estimate charge and spin diffusion lengths, but polarization measurements were badly affected by birefringent components in the optical path of the luminescence. I noticed that the main problem arised from the beamsplitter cube, which needed to be replaced. This is discussed in detail in sec.3.4.4.

The system was not adapted either for imaging at cyrogenic temperatures, since an objective with numerical aperture of $\sim 0.6$ is subjected to significant aberrations due to the presence of the 1 mm thick, BK7 cryostat window. This was solved by using a x50, near-infrared adapted objective with a correction ring that compensates for glass of thickness up to 1.2 mm.

The excitation arm was completely changed by an open 30 mm cage system (visible in Fig.3.2), enabling easier access to all the optics involved in the laser polarization and alignment. This is important because it makes the microscope compatible with different laser sources, something that was extremely difficult with the previously closed, difficult-to-acess excitation arm. This will be discussed in more detail in Sec. 3.4.

Finally, it was not possible to easily switch between $\sigma$ and $\pi$ polarized excitation while exciting the exact same point at the sample with the same power density. To solve this, the original $\lambda/4$ waveplate at the excitation arm (as shown in Favorskiy et al. (2010)) was replaced by the liquid crystal variable waveplate shown in Fig.3.2. This variable waveplate is controlled by an external voltage, thus avoiding a manual rotation of the optical components in the excitation arm, which induces mechanical vibrations and small but non negligible displacements of the laser spot.

### 3.3.2 Determining charge and spin diffusion lengths in a p-GaAs sample

Here I present an example of the results that can be obtained with this optical technique. In Fig.3.3, the charge and spin density obtained via the sum image defined by Eq.(3.5) and the difference image of Eq.(3.6) are shown as a function of space for a 3 $\mu$m thick, p-GaAs ($p = 1.5 \times 10^{17}$ cm$^{-3}$) sample under weak excitation power (0.03 mW) at room temperature. In the bottom panel of Fig.3.3, the spatially averaged profiles of these images are shown (red full circles), together with the measured laser excitation profile (green dashed line), which can be fitted with a Gaussian function of the form $g(r) = g_0 e^{-r^2/\omega^2}$, with $\omega = 0.6$ $\mu$m.

It is seen that both the electron and the spin density profiles extend to distances much larger than the laser spot, revealing lateral diffusion. It is also evident from the profiles that $L_e \gg L_s$ in this sample. The charge and spin diffusion equations, in the absence of an external electric field, are given by Eq.(2.3), which we reproduce here:

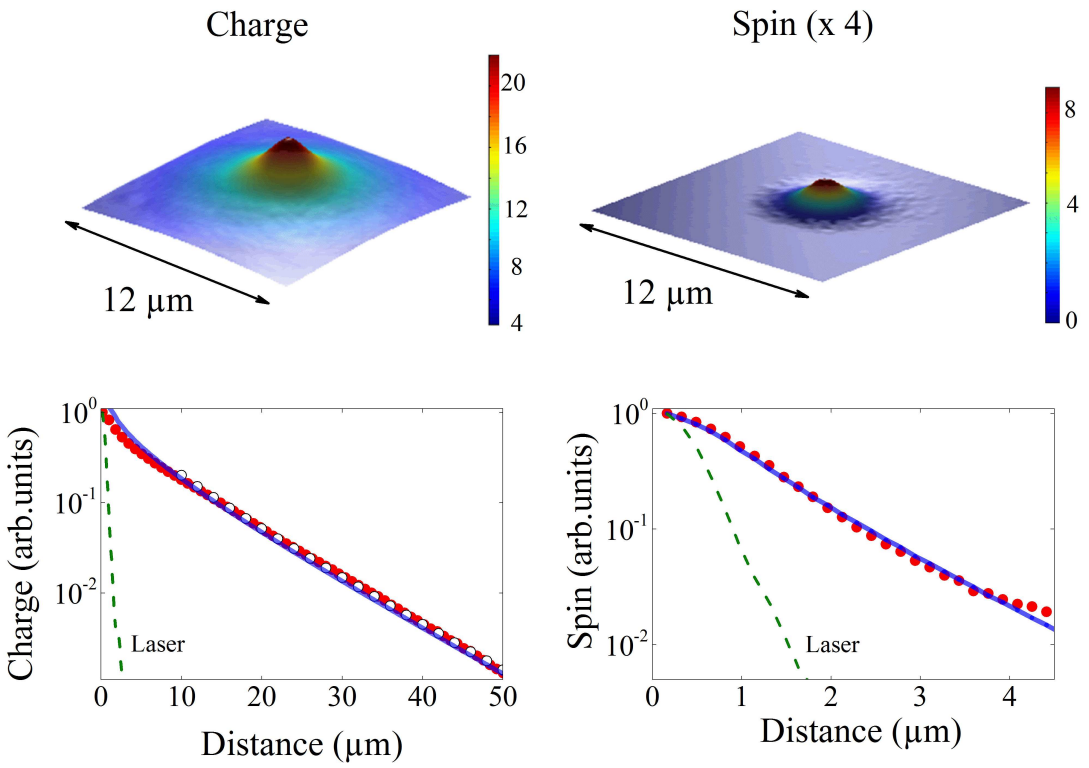


**Figure 3.3:** Top: Measured charge and spin density images obtained under circularly polarized excitation for a p-GaAs ($p = 1.4\times10^{17}$ cm$^{-3}$) sample at room temperature. At the bottom, the corresponding spatially averaged profiles as a function of distance to the laser excitation spot are represented by red full circles. The green dashed-line is the laser profile. The black open circles are a fit for the electronic profile using a modified bessel function of the form of Eq.(3.8), giving an electron diffusion length $L_e = 9.46$ $\mu$m. Blue solid lines are fits using the exact solution of the diffusion equation given by Eq.(3.9), using the same value for $L_e$ mentioned before and a spin diffusion length of $L_s = 1.2$ $\mu$m.

$$\begin{aligned} g(r)e^{-\alpha z}\tau_e - n(r,z) + L_e^2\Delta n(r,z) &= 0 \\ \mathscr{P}_i\, g(r)e^{-\alpha z}\tau_s - s(r,z) + L_s^2\Delta s(r,z) &= 0 \end{aligned} \tag{3.7}$$

where $\alpha^{-1}$ is the absorption length at the laser energy. It can be shown that if $L_e \gg d$, where $d$ is the sample thickness, diffusion is bi-dimensional (independent of depth $z$), and the solution of the charge diffusion equation [Eq.(3.7)] far from the excitation spot can be written as a modified Bessel function of the second kind (see appendix 8.1.1):

$$n(r) \propto K_0(r/L_e) \approx \frac{1}{\sqrt{r}}e^{-r/L_e} \quad r \gg L_e \tag{3.8}$$

Fitting the charge profile with a function of the form of Eq.(3.8) gives an electronic diffusion length $L_e = 9.46\ \mu$m which is indeed much larger than the sample thickness. The fit is shown as the black open circles superposed to the charge density profile of Fig.3.8.

When the diffusion length is smaller or comparable to the sample thickness, the approximation given by Eq.(3.8) is no longer valid. This is the case for spin diffusion in this sample, and therefore the spin diffusion equation needs to be solved exactly. This difficulty can be overcome by using a numerical method, for example, using finite elements, or by using a linear combination of the functions of the form given by Eq.(3.8). I present here an alternative. I have solved the diffusion equation [Eq.(3.7)] for a radially symmetrical excitation using the Green formalism. The details can be found in the appendix 8.1.2. The solution can be written:

$$c(r,z) = 2\pi \int_0^\infty \xi\varphi(\xi)J_0(\xi r)[\int_0^d e^{-\alpha z'}G(\xi, z-z')dz']d\xi \tag{3.9}$$

where $c$ is a concentration (charge or spin), $\varphi(\xi) \propto e^{-\xi^2\omega^2/4}$ is the Fourier transform of a Gaussian excitation profile of radius $\omega$, and $J_0(\xi r)$ is a Bessel function of the first kind. The function $G$ depends on the diffusion length and on the boundary conditions and its analytical form can be found in the appendix 8.1.2. Eq.(3.9) gives the solution in an integral form than can be easily implemented numerically. A fit of the spin profile gives a spin diffusion length of $L_s = 1.2\ \mu\text{m} < d$. Eq.(3.9) can also be used to calculate the charge profile using a diffusion length of $L_e = 9.46\ \mu$m in order to compare with the Bessel function approximation of Eq.(3.8). The profiles obtained with the analytical solution given by Eq.(3.9) for both charge and spin are shown as blue solid lines in Fig.3.3. It is seen that the agreement with Eq.(3.8) is excellent for the charge profile, validating thus the approximation when $L_e >> d$.

### 3.3.3 Spatially-resolved luminescence spectra

The optical setup described in sec.3.3 has the interesting property of being able to monitor the spatial dependence of the luminescence spectra by using a scanned multimode optical fiber that captures the photoluminescence within a spot of size 0.9 $\mu m$ in the sample plane. The fiber is then coupled to a spectrometer to yield a local spectrum, enabling

a study of the energy-resolved spin transport and to monitor the electronic temperature of the photoexcited carriers. In general, three different temperatures are relevant in any minority carrier transport measurement in semiconductors; the temperature $T_L$ of the crystal lattice, the majority hole temperature $T_h$, and the electronic temperature $T_e$. In a highly doped $p^+$-GaAs sample, the photoexcited hole density is in general much smaller than the background hole concentration $N_A^-$. It is supposed therefore that the photoholes are thermalized with the background hole gas, which is in thermal equilibrium with the lattice, i.e, $T_h = T_L$.

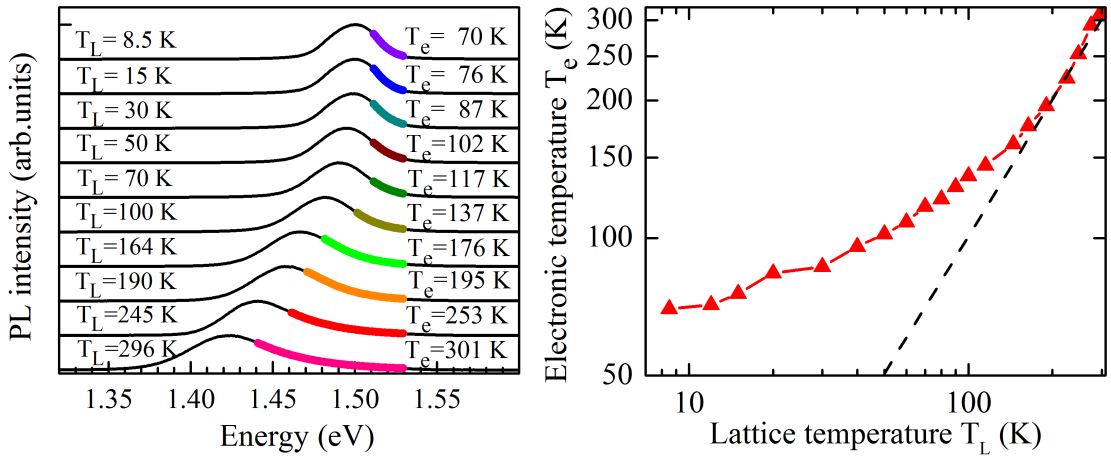


**Figure 3.4:** Left: normalized spatially-averaged luminescence spectra for different lattice temperatures at low excitation power. Fits of the high energy tail of the spectra (shown by thicker lines) are used to estimate the electronic temperature $T_e$. Right: Electron temperature as a function of lattice temperature. $T_e \approx T_L$ above 100 K, while at lower temperatures $T_e$ varies much more slowly, so that $T_e > T_L$. This is because the energy exchange rate between the electron gas and the lattice decreases with temperature.

Figure 3.4 shows the luminescence spectra of a $p^+$ ($10^{18}$ cm$^{-3}$) GaAs sample for different values of the lattice temperature $T_L$. The electronic temperature is shown to significantly differ from $T_L$ due to inefficient scattering by phonons as the temperature is lowered (Ulbrich (1973); Kiessling et al. (2012); Quast et al. (2013)). The lattice temperature $T_L$ is supposed to be equal to the temperature of a Si diode in contact with the sample mounting (see sec.4.1.1), and it can be monitored by the peak wavelength of the luminescence. The electronic temperature $T_e$ can be measured by fitting the high energy tail of

the spectra in Fig.3.4 with a function of the form (Ulrich et al. (2007)):

$$I(h\nu) \propto \sqrt{h\nu - E^*}\,[h\nu]^2 e^{(h\nu - E^*)/(k_B T_e)}. \tag{3.10}$$

where $E^*$ depends on the position of the bandgap, and $h\nu$ is the energy of the luminescence at frecquency $\nu$. When a low excitation power of 0.01 mW is used, the spatially resolved spectra reveals that the electronic temperature is uniform in space and the spectra shown in Fig.3.4 are spatially averaged over a typical radius of $\sim 9$ $\mu$m in the image plane. The right panel of Fig.3.4 shows that $T_e \approx T_L$ above 100 K, and that at lower temperatures $T_e$ is larger than $T_L$. This is in agreement with the behaviour observed by Zerrouati et al. (1988).

As shown in Fig.3.4, when the lattice temperature is kept at 15 K, the electronic temperature is significantly higher, with $T_e$ ranging from 40 K to 75 K between different experiments. These differences may be attributed to changes in the efficiency of the thermal coupling between the sample and the copper sample holder, which will be described in sec.4.1.1, so that the real lattice temperature may not be always that of the Si diode. It is seen from the left panel of Fig.3.4 that below $T_L = 50$ K, the peak wavelength is insensitive to the lattice temperature, so that variations in $T_L$ up to 30 K may explain the different temperatures of the electron gas obtained in different experiments.

The increase of the local temperature of the photoelectron gas caused by an increase of excitation power has been characterized. Shown in the left panel of Fig.3.5 are local luminescence spectra at high excitation power and $T_L = 15$ K, as a function of distance to the excitation spot. The spectra exhibit a change in the shape of the high temperature tail, thus revealing a local heating of the electron gas near $r = 0$. The right panel in Fig. 3.5 shows the spatial dependence of $T_e$ at a lattice temperature of 15 K, for several excitation powers. At low power, the electronic temperature is constant in space and equal to 40 K. Conversely, at the maximum power, $T_e = 80$ K at $r = 0$ and decreases to 50 K over a characteristic distance slightly larger than the radius of the laser excitation spot. The electronic temperature as a function of $r$ can be modelled by a Gaussian function of the form

$$T_e(r, z) = [T_e(0) - T_e^0]e^{-r^2/(\omega_T^2)} + T_e^0, \tag{3.11}$$

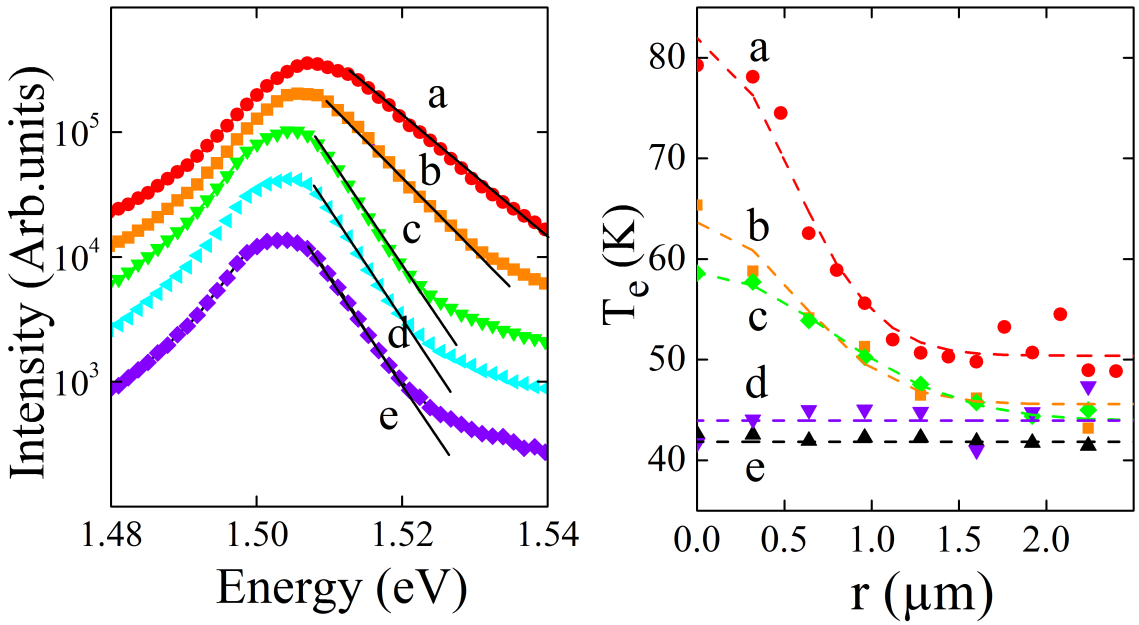


**Figure 3.5:** The left panel shows, for a large excitation power of 2.55 mW at $T = 15$ K, the spatially-resolved luminescence spectra at the place of excitation ($r = 0$) (a) and at a distance of 0.64 $\mu$m (b), 2.7 $\mu$m (c), 4 $\mu$m (d), and 9.6 $\mu$m (e). The larger electronic temperature $T_e$ at $r = 0$ is evidenced from the high-energy side of the spectra. The right panel shows $T_e$ as a function of distance for different excitation powers : 2.55 mW(a), 1.89 mW(b), 1.03 mW(c), 0.45 mW(d) and 1.5 $\mu$W (e). The sample is kept at $T_L = 15$ K.

where $T_e^0$ is the temperature far from the excitation spot, and where $\omega_T$ is of the order of 1 $\mu$m. The dashed lines appearing in the right panel of Fig.3.11 corresponds to fits of the form of Eq.(3.11) for a), b) and c). The characteristic decay length $\omega_T$, of 0.8 $\mu$m, is slightly larger than the Gaussian radius of the laser spot, but significantly smaller than the diffusion length, as will be shown in Chapter 4.

## 3.4 Optical alignment

### 3.4.1 Alignment of the laser beam

It is important to correctly align the laser beam along the vertical axis of the microscope, otherwise the laser spot on the sample will not be limited by diffraction. For this, I used the following setup, where only the relevant optical elements are shown. As indicated in the left panel of Fig.3.6, alignment disks 1 and 2 are positioned such that their $\phi = 1.5$ mm central holes are aligned with the exact center of the 30 mm cage system of the

### 3.4. Optical alignment

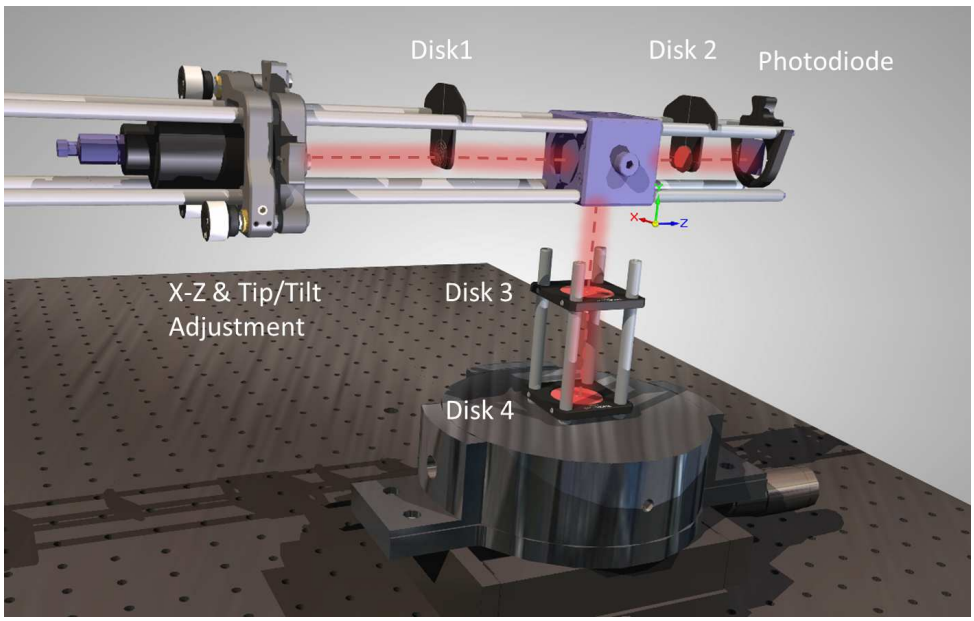


**Figure 3.6:** Schematic of the alignment procedure used to correctly align the laser beam along the vertical axis $\vec{e}_y$ of the microscope after reflection by the beamsplitter. IR fluorescent disks and a Si photodiode can be used in order to quantify the beam's alignment.

beamsplitter. These disks are made of an IR fluorescent material that provides a visual help to see the infrared beam. We define the axes $\vec{e}_x$,$\vec{e}_y$,$\vec{e}_z$ as those of the beamsplitter cube.

To make sure that the laser beam is paralel to $\vec{e}_z$ and that it passes through the center of the beamsplitter, the following iterative method can be used

- Step 1: The photodiode should be placed just after alignment disk 1. Then the intensity that passes through the disk should be maximized by adjusting the X-Z knobs of the laser mount.
- Step 2: Remove the alignment disk 1 and put the photodiode after alignment disk 2. Again, maximize the measured intensity by adjusting this time the Tip/Tilt.
- Step 3: Put back alignment disk 1 and maximize the power that passes through its hole by adjusting the Tip/Tilt.
- Step 4: Repeat Step 2 and 3. Stop when the power measured does not vary significantly between the steps.

Even if the beam passes through the center of the beamsplitter and is parallel to $\vec{e}_z$, it could be that the beamsplitter is slightly tilted with respect to the optical table. For

example, it could be that the $\vec{e}_y$ axis on Fig.3.6 is not exactly perpendicular to the cryostat (and to the sample). To verify this, alignment disks 3 and 4 can be used. The beam should pass through both holes. If is not the case, the Tip/Tilt should be adjusted in order to compensate for this. By repeating the same iterative method mentioned before with disks 3 and 4, the laser should be perpendicularly incident to the sample surface. A further check consists in inserting the X50 objective and to measure the output power with the photodiode. It should be very close to its maximum possible value, which can be determined by measuring the laser power at the exit of the optical fiber and the reflection and transmission coefficients of the beamsplitter and the objective, respectively (see sec.3.4.4).

### 3.4.2 Alignment for the laser polarization

As discussed in 3.3 we need the possibility of switching the laser polarization from right ($\sigma^+$) to left ($\sigma^-$) circular polarization. Also, in order to study charge and spin couplings (see sec.6.2), it is also necessary to switch from a circularly polarized excitation to a linearly polarized one ($\pi$). I tried different setups that involved a manual rotation of an optical component on the excitation arm. For example, if the laser is linearly-polarized, then by using a $\lambda/2$ plate in a mounted rotation followed by a fixed $\lambda/4$ waveplate one can easily control the angle between the linearly polarized laser and the two principal axis of the $\lambda/4$ waveplate, allowing to obtain both $\pi$ and $\sigma$ polarizations. However, this was not optimal since the manual rotation of the $\lambda/2$, along with the subsequent mechanical vibrations of the system, introduces small changes in the position of the beam on the sample. To solve this problem we decided to use an electrically controlled liquid crystal full wave variable retarder, that can introduce a retardation from $\sim 0$ to $\lambda$, as shown in Fig. 3.7. In this way, moving optical elements are removed from the excitation arm.

The procedure used is the following:

- Step 1: In order to better define the linear polarization of the laser,a polarizer is put first, that will be then fixed with respect to all of the other optical components. To adjust the axis of polarization, an analyzer, whose axis is already calibrated, is mounted on a plane parallel to the cryostat. The analyzer is fixed along the

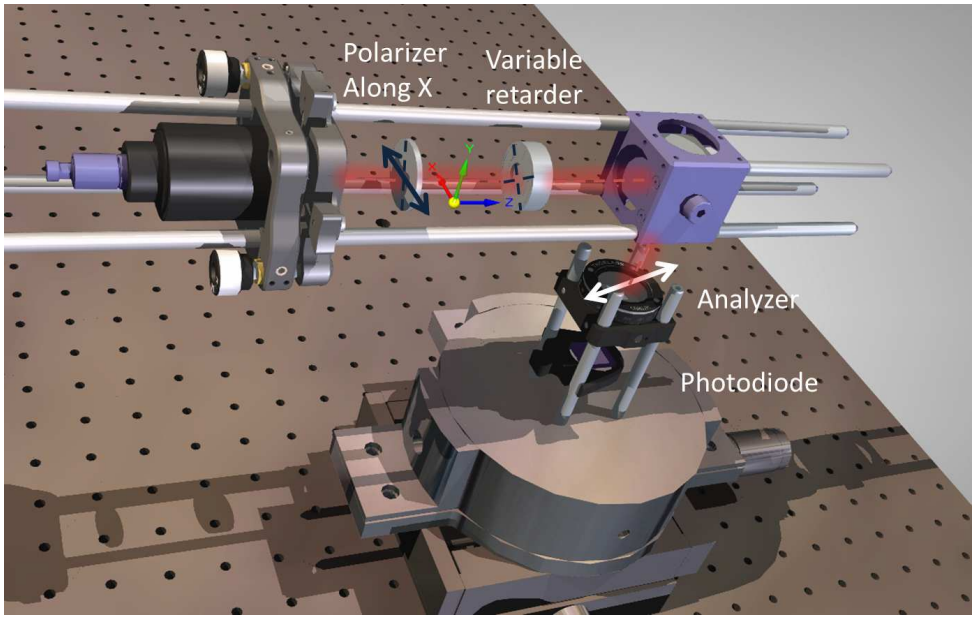


**Figure 3.7:** Schematics of the alignment procedure used to calibrate the variable retarder that controls the laser polarization at the sample. An analyzer and a Si photodiode are used in order to measure the ellipticity of the beam.

$\vec{e}_z$ axis and the polarizer is rotated in order to cross it and minimize the power measured at the photodiode positioned just after the analyzer. At this stage of the alignmnet,the laser is polarized along the $\vec{e}_x$ direction ($\pi_s$-polarization). A typical measured extinction ratio obtained this way is about 14000, which corresponds to a circular degree of polarization of 0.017.

- Step 2: Now the liquid crystal variable retarder must be inserted. First, one of its principal axes should be aligned along the s-polarization of the laser. To do this, the retarder is rotated in order to cross the polarization when the analyzer is along $\vec{e}_z$, as in step 1. When the power is minimized, the axes of the retarder will be aligned with the $\vec{e}_x$ and $\vec{e}_y$ axes of the microscope. Then, by rotating exactly by 45°, the laser beam will sample equally the fast and the slow axis of the retarder.

- Step 3: Now a voltage is applied to the variable retarder and the degree of circular polarization at the position of the sample is measured. This can be done by rotating the analyzer over the entire 360° range and measuring the maximum $P_{max}$ and minimum $P_{min}$ power obtained on the photodiode. The degree of circular polarization

of the laser will be

$$\mathscr{P}^{\text{laser}} = \frac{2\sqrt{\frac{P_{min}}{P_{max}}}}{1+\frac{P_{min}}{P_{max}}} \tag{3.12}$$

Once this calibration is done, the 2 values of the applied voltage that maximize $\mathscr{P}^{\text{laser}}$ (defining the $\sigma^+$ and $\sigma^-$ states) are kept, as well as the 2 values that minimize $\mathscr{P}^{\text{laser}}$ ($\pi_s$ and $\pi_p$ linear polarization states).

With this procedure, a good alignment permits to switch between a circularly-polarized laser with polarization $\mathscr{P} \sim 0.99$ to a linearly polarized laser, with $\mathscr{P} \sim 0.10$ in the best case. I have measured the polarization just after the objective and after the cryostat's window and in both cases I have noticed very small changes in the laser polarization (of the order of $\Delta\mathscr{P} \sim 0.01$). This justifies an alignment without both components, which is much more easy to implement.

### 3.4.3 Alignment for the detection of polarized luminescence

To measure the $\sigma^+$ and $\sigma^-$ components of the luminescence, a fixed analyzer followed by a $\lambda/4$ waveplate that can be rotated manually are used. The schematics is shown in Fig.3.8, and the alignment procedure is the following:

- Step 1: Focus the laser with the X50 (or X10) objective on a sufficiently polished surface. In this way, a significant part of the laser beam will be specularly reflected. Adjust its polarization so that it is $\pi_s$-polarized.

- Step 2: Put the analyzer first (without the $\lambda/4$) and fix its position such that it is crossed (along $\vec{e}_z$) with the polarization of the reflected beam.

- Step 3: Now the laser must be switched to $\sigma^+$ polarization. Then, insert the $\lambda/4$ and adjust its position such that the power after the analyzer is minimized. Define this configuration as $\sigma^{+-}$.

- Step 4: Since the fast and slow axes of the $\lambda/4$ will be approximately at 45° with respect to the $\vec{e}_x$ and $\vec{e}_z$ axes, then a rotation of the waveplate by 180° along the $\vec{e}_z$ direction will now maximize the power through the analyzer. This defines the $\sigma^{++}$ configuration.

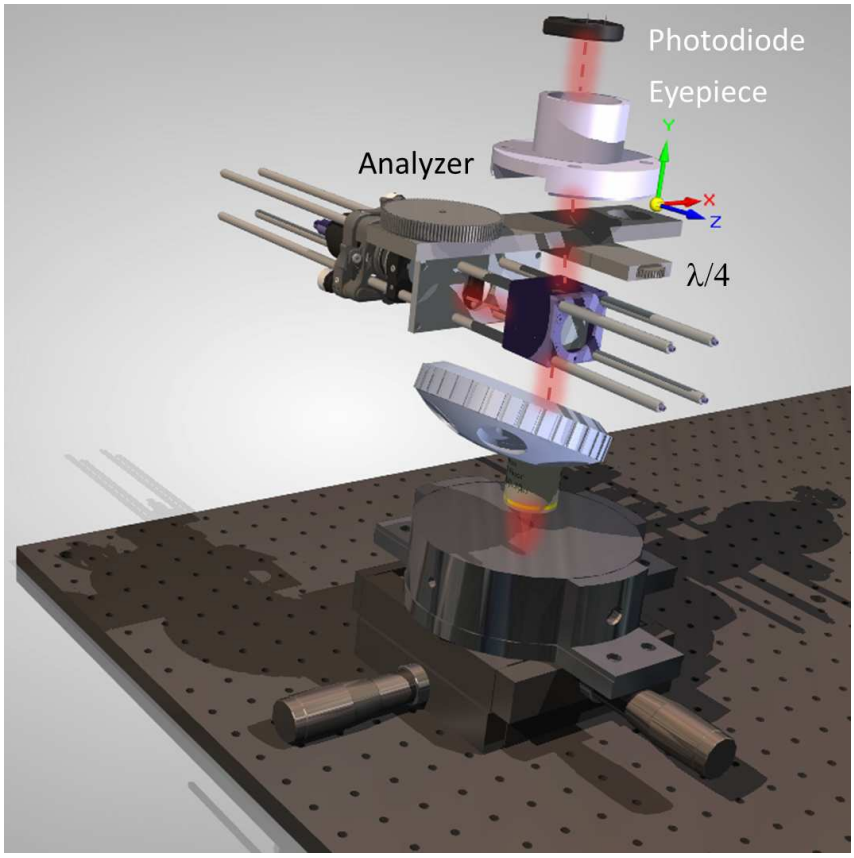


**Figure 3.8:** Schematics of the main optical components that are present in the luminescence path. An alignment of the $\lambda/4$ and of the analyzer is required in order to properly measure the luminescence's circular degree of polarization.

Then, a measurement of the power after the analyzer under the two possible, right and left circular polarizations of the laser will give 4 values, corresponding to the configurations $\sigma^{++}$,$\sigma^{+-}$,$\sigma^{--}$, and $\sigma^{-+}$. A good alignment should give very symmetrical values for $\sigma^{++}$ and $\sigma^{--}$, and equally for $\sigma^{+-}$ and $\sigma^{-+}$. If there is a little asymmetry, it can be corrected by rotating the analyzer by a fraction of a degree. A good alignment usually gives differences smaller than 5 % between the $\sigma^{++}$ and $\sigma^{--}$ configurations.

### 3.4.4 Characterization of the beamsplitter

The microscope as it was reported by Favorskiy et al. (2010) had problems of birefringence, that is, the polarization of the luminescence was highly distorted by the optics. The main symptom was a large asymmetry between the $\sigma^{++}$ and the $\sigma^{--}$ (and between $\sigma^{+-}$ and the $\sigma^{-+}$) images. This resulted in poor images for the spin density and a systematic error on the measurement of the luminescence polarization. Also, since both the

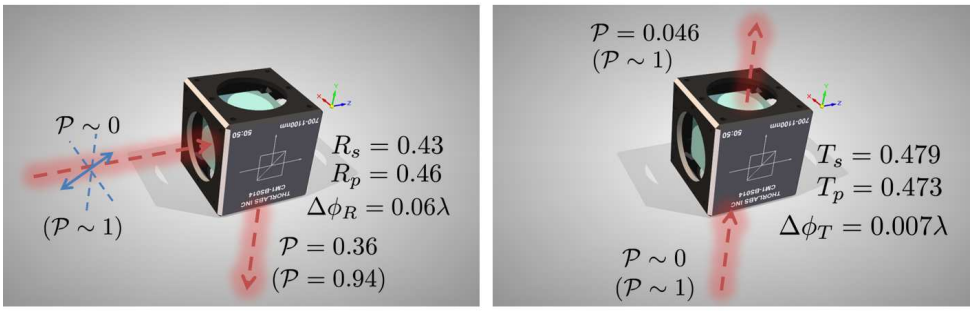


**Figure 3.9:** Characterization of the optical properties of the beamsplitter in reflection (left) and transmission (right) configurations.

excitation and the luminescence paths had moving parts, the images shifted between measurements and this resulted in many cases in an asymmetrical luminescence image. A lot of effort was put into identifying the different sources of aberrations. One of them was the beamsplitter that came with the original Nikon microscope, which was not optimized for IR light, and, more importantly, did not conserve light polarization. It was replaced with a Thorlabs non polarizing cube, made from NBK7 which, as I will show in this section, significantly improves the measurement of the luminescence polarization.

The beamsplitter is a key component of the microscope since it acts on both the laser and the luminescence polarization. A detailed study of its optical properties was performed. Figure 3.9 shows the reflexion and transmission coefficients of the cube at $\lambda = 780$ nm when oriented in its best possible configuration (the one that minimizes the retardarion along the luminescence path).

By sending a linearly-polarized beam ($\mathscr{P} \sim 0$) whose axis is at 45° with respect to the cube's principal axes, a degree of circular polarization of $\mathscr{P} = 0.364$ after reflexion is measured. Using a simple model where the only parameters are the measured reflectivity coefficients along the two axes, $R_s = 0.435$ and $R_p = 0.457$, and the retardation between the two components of the electric field, $\Delta\phi_R$, it is possible to explain the measured polarization after reflection by a retardation of $\Delta\phi_R = 0.119\lambda$. This model predicts that a circularly polarized beam will have a polarization of $\mathscr{P} = 0.93$ with principal axes at 133.2° and 45.2° after reflection. The actual measurement with a circularly polarized beam gives $\mathscr{P} = 0.936$ with principal axes at $134 \pm 1°$ and $44 \pm 1°$. It is therefore desir-

able that when the laser is linearly-polarized, its polarization should be aligned with the principal axes of the cube ($\pi_s$ or $\pi_p$ polarization). Otherwise, the beamsplitter introduces an unavoidable retardation between the $\vec{e}_x$ and $\vec{e}_y$ components of the electric field and the laser at the position of the sample will be elliptically (instead of linearly) polarized.

In the luminescence path, both transmission coefficients for $\pi_s$ and $\pi_p$ polarizations are almost identical (1 % difference), and the measured retardation, of $\Delta\Phi_T = 0.014\lambda$, is very small. This, again, was obtained by measuring the polarization after transmission of a linearly-polarized light with an axis at 45° respect to the axes of the cube. This $\Delta\Phi_T$ predicts a polarization of $\mathscr{P} = 0.999$ when perfectly circularly polarized light is incident. The measured value is $\mathscr{P} = 0.9988$. This is very good for a clean and accurate measurement of the luminescence polarization. As a comparision, the original beamsplitter had $R_p = 0.447$, $R_s = 0.409$, $\Delta\phi_R = 0.05\lambda$, $T_s = 0.469$ , $T_p = 0.463$ and $\Delta\phi_T = 0.069\lambda$. It is seen that the retardance in the luminescence path was a factor of 10 larger with the previous cube.

Although asymmetries can be accounted for by changing the sign of the excitation helicity from $\sigma^+$ to $\sigma^-$ and using Eqs.(3.5) and (3.6), the additional phase shift in the luminescence path introduces an error on the measured polarization that cannot be perfectly compensated. This is because in our system, the $\lambda/4$ waveplate is restricted to be aligned at 45° with respect to the cube's axes. Otherwise, the manual rotation of the waveplate holder used to pass from the $\sigma^+$ to the $\sigma^-$ components of the luminescence will not work. It is easy to see that, with this restriction, and for a extreme case where the beamsplitter acts as a $\lambda/4$ or as an analyzer, then a $\sigma^+$ photon will be always detected with the same probability as a $\sigma^-$ photon and the measured polarization will be always zero.

| Microscope's optics | | |
|---|---|---|
| Optical component | Reference | Main properties |
| Linear Polarizer | LPNIR100 Thorlabs | Extinction ratio $> 10000$ for 750-1600 nm, $T = 0.85$ at 780 nm |
| Variable retarder | LCC1113-B Thorlabs | Liquid crystal, retardance range $30$ nm to $\lambda$ |
| Beamsplitter | CM1-BS014 Thorlabs | $R_s = 0.435$,$R_p = 0.457$,$T_s = 0.469$,$T_p = 0.463$ |
| Cryostat window | Fichou | BK7, $T_s = .989$, $T_p = 0.992$ at 780 nm. |
| Microscope objective | LCPLN50XIR Olympus | NA=0.65, Working distance 4.5 mm, Glass thickness correction 0-1.2 mm, $T = 0.65$ at 780 nm |
| Quarter waveplate | AQWP05M-980 Thorlabs | Retardation $0.258$ $\lambda$ at 780-866 nm, $T = 0.97$ at 780 nm |
| Analyzer | U-AN360P Olympus | $T = 0.7$ at 780 nm |
| Filter | FF01-800/LP Semrock | $T = 1.17 \times 10^{-7}$ at 780 nm, $T > 0.95$ for 815-870 nm |
| Eyepiece | Nikon | f=200 mm |
| CCD | KAF-1600 Kodak | Quantum efficiency: $35$ % at $850$ nm, 16 bits, pixel dimension $9$ $\mu$m, $1534 \times 1020$ pixels |
| Optical fiber 1 | M14L05 Thorlabs | Multimode, diameter $\phi = 50$ $\mu$m |
| Optical fiber 2 | M35L02 Thorlabs | Multimode, diameter $\phi = 1000$ $\mu$m |
| Spectrograph | Princeton instruments | $0.2$ nm/pixel |

## 3.5 Conclusions of this chapter

In conclusion, a polarized imaging technique for investigating charge and spin transport has been described. At high excitation power, the tightly-focused circularly-polarized light generates strongly inhomogeneous charge,spin and temperature distributions which are monitored using imaging and spectroscopic techniques. It will be shown with the two following chapters that this technique is very well adapted for investigating spin transport.

## 3.5. Conclusions of this chapter

# Chapter 4

# Charge and spin transport in $p^+$ GaAs in non degenerate conditions

In this chapter I will present experimental results on drift and diffusion of spin-polarized photoelectrons at low injection density where the Pauli-principle couplings between charge and spin are negligible. This investigation will permit to determine the key parameters for charge and spin transport as a function of temperature and appears very important for interpreting the effects of the Pauli principle, to be explained in Chapter 6. The drift-diffusion equations for the charge and spin density can be written in the simple form [Eq.(2.3)], which is reproduced here:

$$(g_+ + g_-)\tau_e - n + \vec{\nabla} \cdot [n\mu_e\tau_e\vec{E}] + L_e^2\Delta n = 0$$
$$(g_+ - g_-)\tau_s - s + \vec{\nabla} \cdot [s\mu_s\tau_s\vec{E}] + L_s^2\Delta s = 0$$

where $\vec{E}$ is an external electric field. Our experimental technique (Chapter 3) is used to determine, as a function of temperature, $L_e = \sqrt{D_e\tau_e}$ and $L_s = \sqrt{L_s\tau_s}$ as well as the products $\mu_e\tau_e$ and $\mu_s\tau_s$ when an electric field is applied. A careful distinction is made between the lattice temperature, assumed to be in equilibrium with the hole gas, $T_L = T_h$, and the electron temperature $T_e$, which differ significantly from each other (as discussed in sec.3.3.3). The temperature dependence reveals that the electron mobility $\mu_e$ depends strongly on $T_e$ and only weakly on $T_L$. To my knowledge, this is the first experimental study that separates the effect of $T_e$ and $T_L$ on the minority electron mobility. Current theoretical calculations do not explain these results, since they have largely assumed that

it is $T_L$ that determines the mobility.

## 4.1 About the GaAs samples

The samples studied here are 3 $\mu$m films of $p^+$-doped GaAs grown by using gas source molecular beam epitaxy on top of a (100) semi insulating GaAs wafer (470 $\mu$m thick) at the Institut d'Electronique, de Microelectronique et de Nanotechnologie (IEMN). The film was uniformly doped with carbon with a nominal doping level of $p = 10^{18}$ cm$^{-3}$, confirmed by Hall measurements (see Sec.4.2.5). Optical and SEM images of one cleaved piece of the sample are shown in Fig.4.1. The thickness of the p-region was chosen to be smaller than the microscope's depth of field but large enough so that most of the incident light excitation is absorbed within (absorption length at 780 nm is $\alpha^{-1} \approx 1$ $\mu$m (Blakemore (1982))). During the epitaxial growth, firstly a 100 nm thick, lattice matched $Ga_{0.51}In_{0.49}P$ layer was grown on top of the semi insulating GaAs wafer, as can be seen in Fig.4.1. This acts as a barrier that confines photoelectrons to the active $p^+$-layer, and also ensures a negligible recombination velocity at the interface. Fig.4.1b) shows a schematic of the sample. An X-ray diffraction analysis shows that the grown $p^+$-GaAs layer is unstrained, monocrystalline with a (001) texture, and that the $Ga_{0.51}In_{0.49}P$ layer has an exact thickness of 93 nm and a lattice constant in the growth direction which is 0.16 % larger than that of the substrate and of the p-layer.

In addition, Hall bars were fabricated using electron beam lithography and dry etching techniques on cleaved 8 mm $\times$8 mm pieces of this sample. Platinum-based ohmic contacts were formed using evaporation, liftoff and subsequent annealing. One resulting sample is shown in panel a) of Fig. 4.2. In the naked eye image, metal pads of approximately 2 mm by 2 mm, are clearly visible.

They are covered by a 200 nm thick gold layer to enable wire bonding (see sec.4.1.1). The GaAs mesa was defined using chlorine-based reactive ion etching which enables the formation of vertical side walls for the hall bars. The lateral dimensions of the hall bar are 50 $\mu$m long and 10 $\mu$m width, as shown on the SEM image of panel a) in Fig.4.2. Shown in panel b) are images (from left to right) of the reflected laser spot, and of the luminescence without and under an applied electric field.

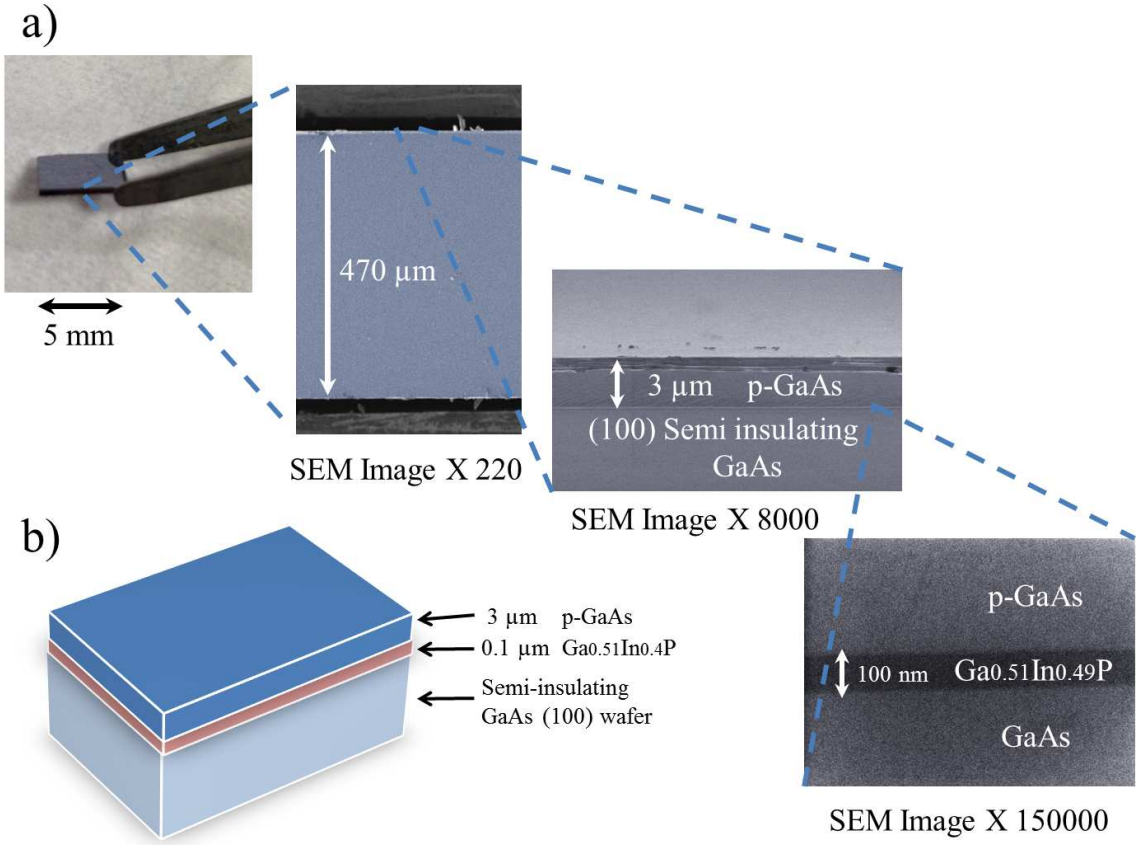


**Figure 4.1:** a) Optical (left) and SEM images of a $p^+$-GaAs sample grown by molecular beam epitaxy over a semi-insulating GaAs wafer (470 $\mu$m). The thickness of the p-region is 3 $\mu$m, and a $\sim$ 100 nm thick, $Ga_{0.51}In_{0.49}P$ barrier was also grown between the substrate and the active layer in order to confine photoelectrons and to ensure a small surface recombination velocity at the back interface. b) Schematic of the layered structure of the sample.

### 4.1.1 Wire bonding and sample cooling

The possibility of applying an electric field to monitor drift and diffusion of spin-polarized photoelectrons at low temperatures necessitates external contacts to the Hall bar sample with external wires that can be manipulated from outside the cryostat. This was done in two steps. First, by using a ultrasonic wedge bonding machine we have contacted Al/Si flexible wires between the Au/Ti pads of the sample and a 0.4 mm thick printed circuit board (PCB) that has a $10 \times 10$ mm square hole at its centre for the sample. This allows for the pads on the sample and the copper contacts at the PCB to be at almost the same height (thickness of the sample is $\sim$ 0.5 mm. This is shown on panel a) of Fig.4.3. The sample and the PCB are glued with a GE varnish solution that makes a very thin layer with a good thermal contact between the sample and the copper sample holder. Drops

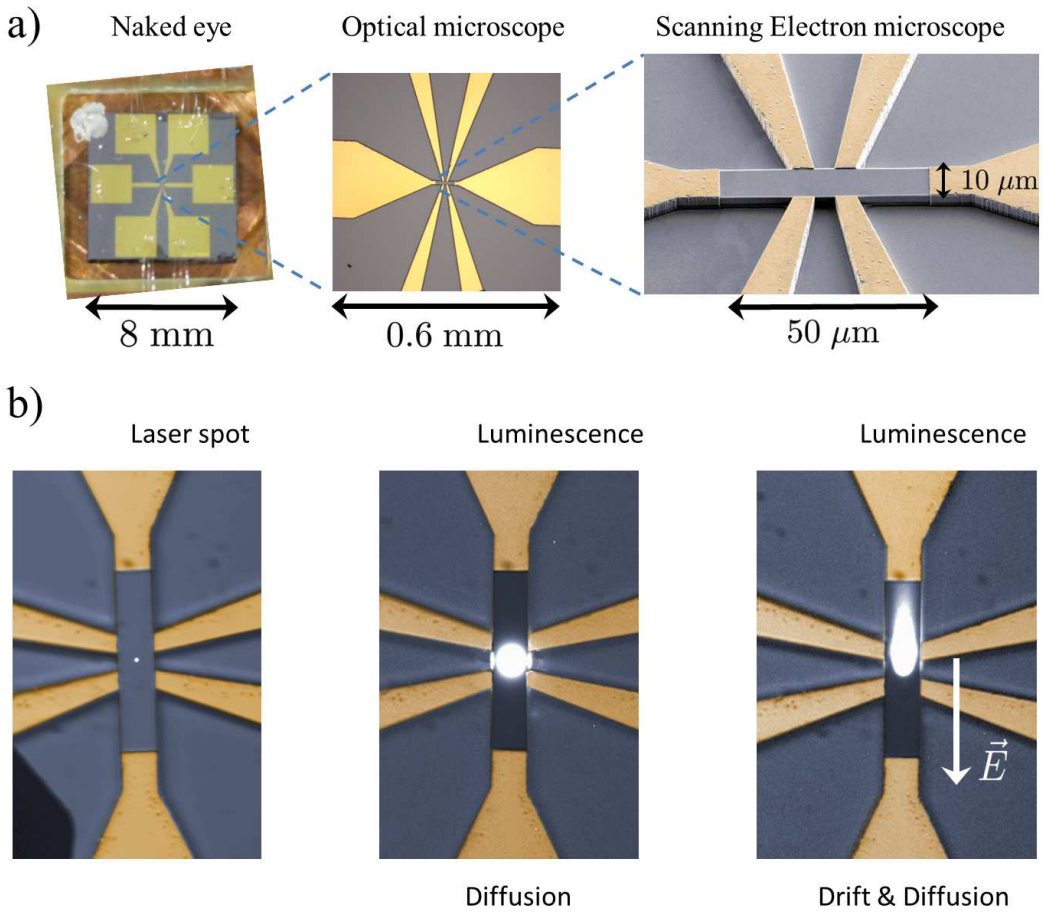


**Figure 4.2:** a) Samples were cleaved into a 8 mm by 8 mm squares, with the $p^+$-GaAs film shaped using electron beam lithography and dry etching techniques into a Hall bar with Platinium-based ohmic contacts. b) Images obtained with the experimental setup described in 3.3 of the reflected laser spot, of the resulting luminescence without electric field, revealing lateral diffusion of photoelectrons, and with an applied electric field, revealing both drift and diffusion (left to right).

of silver paint at the corners can be used to provide additional thermal conductivity and mechanical stability.

As shown in panel b) of Fig. 4.3, the sample holder is mounted on a Oxygen-free high thermal conductivity (OFHC) copper sample mount that is surrounded by a heat exchanger. Tin-lead solder is then used to contact the PCB's Cu pads with wires that are connected to the exterior. Since these wires ends are located outside the cryostat, it is important to evacuate the heat on them before they arrive at the PCB, otherwise they can modify the sample's temperature. To do this, the wires are wrapped around the stainless steel joint that links the sample holder and the external structure of the cryo-

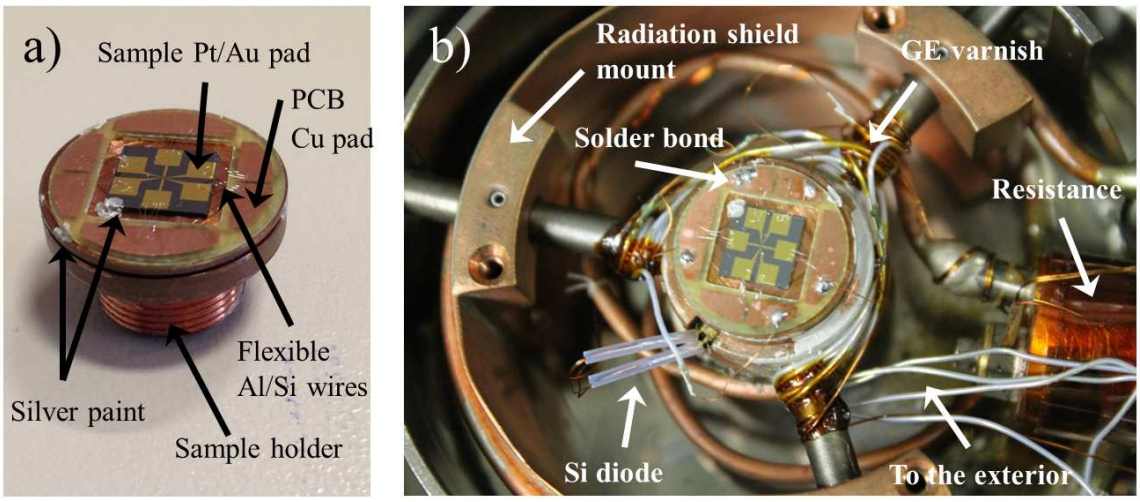


**Figure 4.3:** a) The sample is surrounded by a PCB which has printed Cu pads on it. Electrical connection between the PCB pads and the Au/Pt pads of the sample is achieved by wedge ultrasonic bonding of flexible Al/Si wires. Both the sample and the PCB are glued to the Cu sample holder with GE varnish. Additional drops of silver paint may be used to improve thermal contact. b) The internal wires of the cryostat, which can be accessed from the exterior, are connected to the PCB by using a standard Sn-Pb solder. They are wrapped and glued with GE varnish around the stainless steel joints in order to keep them at the same temperature of the sample.

stat. Since stainless steel has a low thermal conductivity, the wrapping was done near the cooling stage. A viscous solution of GE varnish is used to glue them and improve thermal contact. A DT-670 Si photodiode is used as thermometer, and the temperature of the sample can be controlled by an Oxford Instrument closed loop system that applies a current through a 18 Ω resistor that heats the outside of the tube carrying the liquid He flow.

As shown on panel a) of Fig. 4.4, a nickel (Ni) plated, OFHC Cu radiation shield is used to prevent thermal radiative coupling with higher temperature surfaces. This shielding is very important since the cooling power of this system is about 3 Watts and I estimate the radiation power emitted by the 25 mm window at 300 K to be 0.5 W. This shield is cooled by helium exhausting from the heat exhanger. The cryostat is pumped down to $10^{-5}$ Torr, and a continous helium flow is supplied by a pressurized dewar (200 mbar) that is connected through a transfer line to the cryostat's heat exchanger, as shown on panel b) of Fig.4.4. The Helium flow can be monitored and regulated by a flow meter panel that has control valves in it. Nominal Helium transfer is 0.7 lt/hour corresponding to a cooling power of 3 Watts at 20 K.

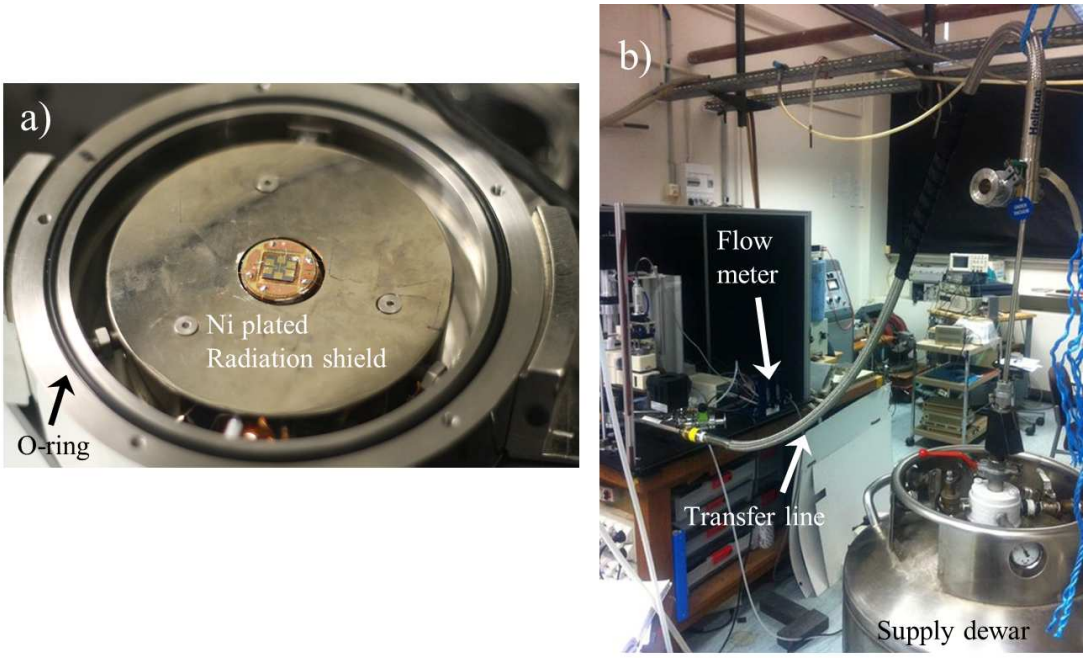


**Figure 4.4:** a) The sample is protected from radiative thermal couplings by using a Ni plated radiation shield. b) The He flow is provided by a transfer line connected to a pressurized He supply dewar. The flow meter allows to measure and control the cooling rate.

A bad thermal contact between the sample and the Cu mount can be detected by comparing the temperature of the Si photodiode and the luminescence spectra at low excitation intensity, since the peak wavelength at low temperatures is known. Another possibility is to perform a 4 terminal resistivity measurement when the Hall bar sample is inside the cryostat. The temperature stability is, in the best conditions, of 0.01 K at 15 K and of about 5 K above 150 K. This is obtained with a PI feedback control with parameters $K_p = 15$ (proportional gain) and $T_I = 2$ minutes (integration time constant), which I've obtained by following the Nyquist criterion at 15 K. Of course, the best parameters depend on the He flow rate and temperature, which is not always easy to control precisely. In practice, I only change the integral time when the set temperature is increased.

## 4.2 Charge and spin transport by polarized luminescence microscopy

### 4.2.1 Measurement of the charge and spin diffusion lengths

The spatially-resolved luminescence of a $p^+$ GaAs sample (detailed in sec.4.1) was studied as a function of temperature. The laser excitation spot has a Gaussian radius of $\omega \approx 0.6\ \mu m$ and energy 1.59 eV. Figure 4.5 shows the measured charge and spin profiles at $T_L = 300$ K and $T_L = 15$ K for different excitation powers. At room temperature, no difference is observed in the charge and spin profile when the power spans 5 orders of magnitude between $\sim 10^{-5}$ mW and $\sim 1$ mW. At low temperature and below 1 mW, the profiles, and therefore, the effective charge and spin diffusion lengths are independent of photoelectron density. Conversely, at high excitation power a difference is observed in the region $r \leq 2\ \mu$m, beyond which the charge and spin profiles decay with the same caracteristic length as in the low power regime. We will see that at $\sim 1$ mW and near $r = 0$, photoelectrons are degenerate at $T_L = 15$ K, which modifies diffusion transport, as will be discussed in the following chapters. Also shown in the bottom panel of Fig.4.5 is the total, spatially-integrated luminescence intensity as a function of power. Lines represent unit slope, indicating that the total luminescence is perfectly linear in power at room and low temperature. Since the total luminescence intensity should not depend on diffusion, this suggests a constant effective electron lifetime within the power range explored.

The spatially-averaged spin polarization, which is also shown in the bottom panel of Fig.4.5, is calculated as :

$$\langle \mathscr{P} \rangle = 2 \frac{\int_0^\infty r I_d(r) dr}{\int_0^\infty r I_s(r) dr} \tag{4.1}$$

with $I_s$ and $I_d$ defined by Eq.(3.3) and Eq.(3.4), respectively. It exhibits a 4-fold increase, passing from $\mathscr{P} \sim 10$ % at room temperature to $\mathscr{P} \sim 40$ % at low temperature and low power densities. At room temperature, the decrease of $\langle \mathscr{P} \rangle$ at high density may reflect a moderate decrease of the spin relaxation time $T_1$, whereas at low temperature the decrease of $\langle \mathscr{P} \rangle$ is mainly related to a spin-dependent diffusion, as will be discussed in Chapter 6.

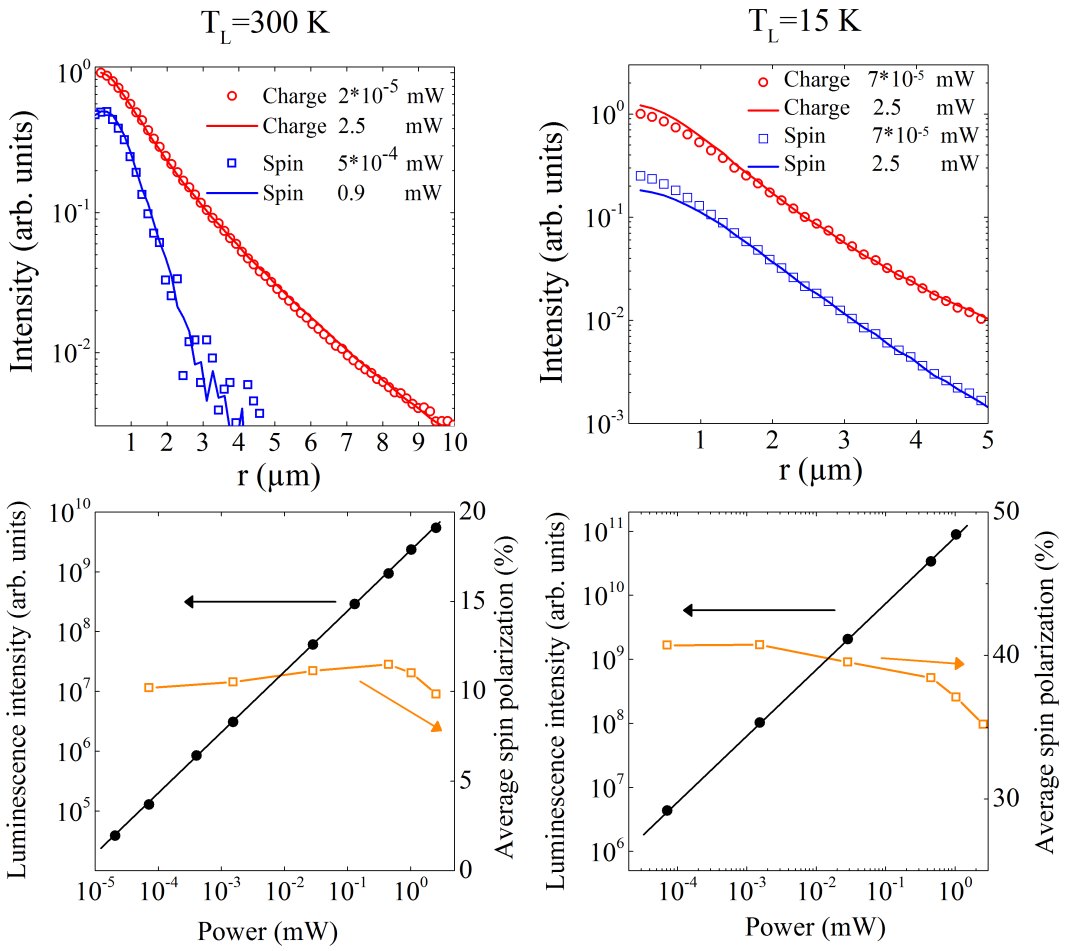


**Figure 4.5:** Top: charge and spin profiles at room and low temperature for excitation powers of $\sim$ 2 mW (full lines) and $\sim 2 \times 10^{-5}$ mW (open circles and open squares, respectively). No change is observed at room temperature, whereas at $T_L = 15$ K, a change is visible over the first $2\mu$m, where the photoelectrons are shown to be degenerate (see Chapter 6). Bottom: total luminescence intensity and spatially averaged spin polarization as a function of excitation power. The luminescence is a linear function of the excitation power at room and low temperatures, whereas the averaged spin polarization increases by a factor of 4 when the temperature is lowered.

In the rest of this chapter, the results obtained at weak photoelectron concentration are presented (excitation power of 10 $\mu$W, which produces a non degenerate photoelectron concentration of $\sim 5 \times 10^{14}$ cm$^{-3}$ at $r = 0$ in the steady state). Figure 4.6 shows the angular-averaged cross sections of the sum (Eq.(3.3)) and difference (Eq.(3.4)) images obtained at different electronic temperatures. As discussed in sec.4.1, this sample has a GaInP passivation layer at the rear surface so that recombination is negligible at the GaAs/GaInP interface. However, the front surface is naturally oxidized. In consequence,

the slope of the profile will depend on the bulk lifetime, $\tau$ and on the diffusion constant, $D$, but also on the recombination velocity at the front surface, $S$. It may seem therefore necessary to measure $S$ in order to obtain the intrinsic diffusion length $L = \sqrt{D\tau}$ from the profiles of Fig.4.6. However, it is possible to show that the analytical solution of the diffusion equation [Eq.(8.1.2)], is equivalent to the solution obtained by taking $S = 0$ and an effective bulk lifetime $\tau^{\text{eff}}$ such that the profiles of Fig.4.6 may be fitted with an effective diffusion length, given by $L^{\text{eff}} = \sqrt{D\tau^{\text{eff}}}$ . In this way, the effective charge lifetime $\tau_e^{\text{eff}}$ and the effective spin lifetime $\tau_s^{\text{eff}} = (1/\tau_e^{\text{eff}} + 1/T_1)^{-1}$ take into account bulk and surface recombination [Cadiz et al. (2013)].

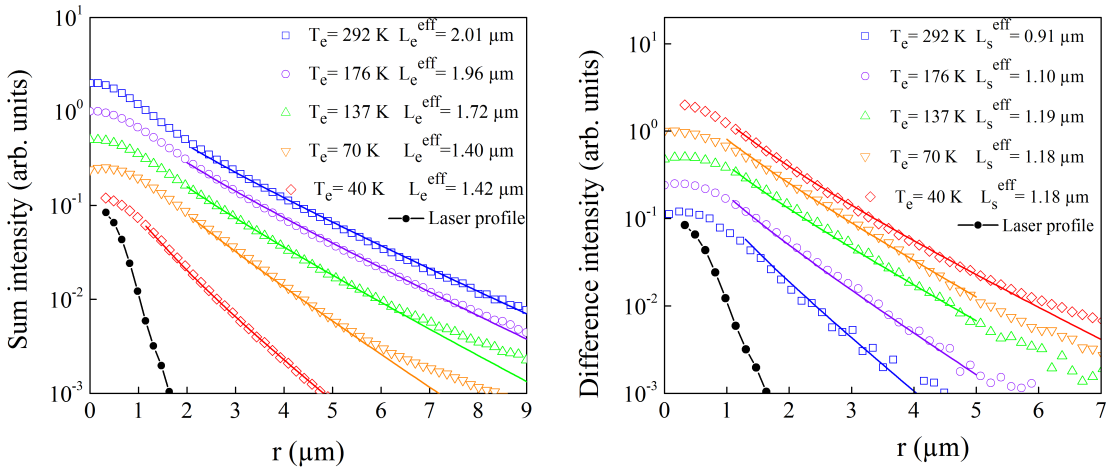


**Figure 4.6:** Sum and difference intensity profiles for a p-GaAs sample at different values of the electronic temperature. Note that for clarity, the sum (difference) profiles have been shifted upwards (downwards) with increasing temperature. It is seen that the charge effective diffusion length has a tendency to decrease when the temperature is lowered, whereas the opposite is observed for the spin effective diffusion length. This is a signature that spin relaxation is strongly supressed at low temperatures.

The measured effective diffusion lengths are shown in the right panel of Fig. 4.7, revealing that their temperature dependence is rather weak, in agreement with the results of Luber et al. (2006). In general, $L_e^{\text{eff}}$ tends to decrease with temperature $T_e$, whereas the opposite happens for $L_s^{\text{eff}}$. At the lowest temperature of $T_e = 40$ K, the measured diffusion lengths are $L_e^{\text{eff}} = 1.42 \pm 0.05$ $\mu$m and $L_s^{\text{eff}} = 1.18 \pm 0.05$ $\mu$m. The left panel of Fig. 4.7 shows the polarization profile given by Eq.(3.2) obtained from the curves of Fig.4.6. It is clearly seen that the magnitude of the electronic polarization increases when $T_e$ is

**Table 4.1:** Effective charge and spin diffusion lengths for selected temperatures.

| $T_e$ (K) | $T_L$ (K) | $L_e^{\text{eff}} \pm 0.05$ ($\mu$m) | $L_s^{\text{eff}} \pm 0.05$ ($\mu$m) | $\langle \mathscr{P} \rangle$ |
|---|---|---|---|---|
| 40 | 15 | 1.42 | 1.18 | 0.39 |
| 50 | 15 | 1.24 | 1.10 | 0.39 |
| 70 | 12 | 1.40 | 1.18 | 0.34 |
| 102 | 50 | 1.68 | 1.16 | 0.25 |
| 130 | 90 | 1.75 | 1.17 | 0.19 |
| 161 | 140 | 1.86 | 1.12 | 0.16 |
| 195 | 190 | 1.93 | 0.94 | 0.12 |
| 292 | 275 | 2.08 | 0.92 | 0.08 |

lowered, and it is close to its maximum possible value of 50 % at $r = 0$ and $T_e = 40$ K. Also, the decay length of the polarization is longer at lower temperatures. As it will be shown by time-resolved photoluminescence in sec.4.2.3, this is the consequence of two effects; i) the effective electron lifetime decreases as radiative recombination is enhanced at low temperatures, and ii) the spin relaxation time $T_1$ increases as the temperature is lowered.

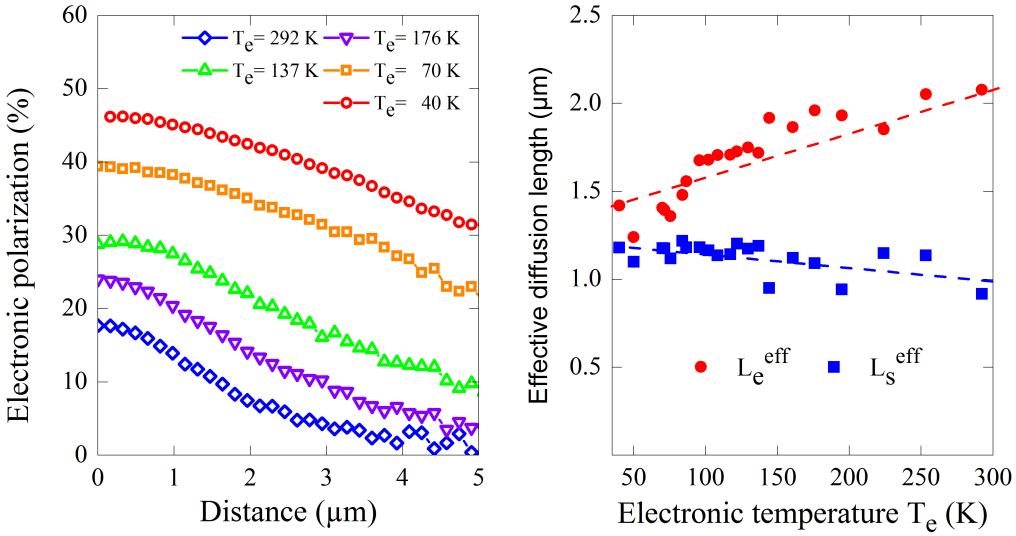


**Figure 4.7:** Left: spin polarization profiles as a function of temperature. It is seen that its value at $r = 0$ increases from $\mathscr{P}(0) = 0.18$ at room temperature to $\mathscr{P}(0) = 0.45$ at $T_e = 40$ K. Right: Effective charge and spin diffusion lengths measured as a function of electronic temperature. The dashed lines are a guide to the eye.

In Table 4.1, measured effective charge and spin diffusion lengths for different temperatures are summarized, as well as the spatially-averaged spin polarization.

### 4.2.2 Measurement of the charge and spin drift lengths

The minority carrier drift length $L_d = E\mu\tau$ is determined by imaging the spatial dependence of the luminescence, as in sec.4.2.1, as a function of the applied electric field $E$. As shown in Fig.4.8(a), the Hall bar shaped sample can be used to apply an electric field between contacts $A$ and $B$. The magnitude of the electric field in the p-GaAs region can be determined by measuring the voltage difference between contacts $C$ and $D$, which are separated by a distance of 11 $\mu$m. Also, a Hall voltage $V_F - V_D$ can be measured when a magnetic field is applied perpendicular to the plane of the sample, which permits to measure the majority hole concentration and mobility as a function of temperature. The density of ionized acceptors $N_A^-$ is only weakly temperature dependent and the hole mobility varies in the range $\mu_h = 100 - 202$ cm$^2$V$^{-1}$s$^{-1}$ when $T_L$ is varied. A detailed discussion of these results can be found in Cadiz et al. (2015b).

Fig.4.8(b) shows the sum and difference images for different values of the electric field at $T_L = 15$ K and excitation energy of $h\nu = 1.55$ eV at low power (0.1 $\mu W$). Drift of the electrons leads to a significant change of the images. The cross sections of these images in the direction of the electric field are shown in Fig.4.9. They are well approximated by the 2-dimensional diffusion result of appendix 8.1:

$$n(x) \propto e^{(\mu_e \tau_e^{\text{eff}} E x)/(2D_e \tau_e^{\text{eff}})} K_0 \left[ \frac{\sqrt{(\mu_e \tau_e^{\text{eff}} E)^2 + 4D_e \tau_e^{\text{eff}}}}{2D_e \tau_e^{\text{eff}}} \, x \right], \tag{4.2}$$

where $D_e$ and $\tau_e^{\text{eff}}$ are the electron diffusion constant and effective lifetime, respectively, and $K_0$ is a modified Bessel function of the second kind. In a nondegenerate electron gas the only fitting parameter in Eq.(4.2) is the $\mu_e \tau_e^{\text{eff}}$ product, as previously discussed in sec.2.5. The same analysis is performed for the difference image where, in Eq.(4.2), $n$, $\tau_e^{\text{eff}}$ and $D_e$ are replaced by $s$, $\tau_s^{\text{eff}}$ and $D_s$, respectively.

Figure 4.10 shows the measured $\mu\tau^{\text{eff}}$ value for the charge and spin densities as a function of the applied electric field at $h\nu = 1.55$ eV. Also shown is data obtained at a higher temperature of $T_L = 35$ K and low power excitation at an energy $h\nu = 1.59$ eV. In both cases, when the electric field is increased, a decrease of $\mu\tau^{\text{eff}}$ is observed. For $T_L = 15$ K, the decrease is very sharp for $E \leq 200$ V/cm. In order to show that this effect can have

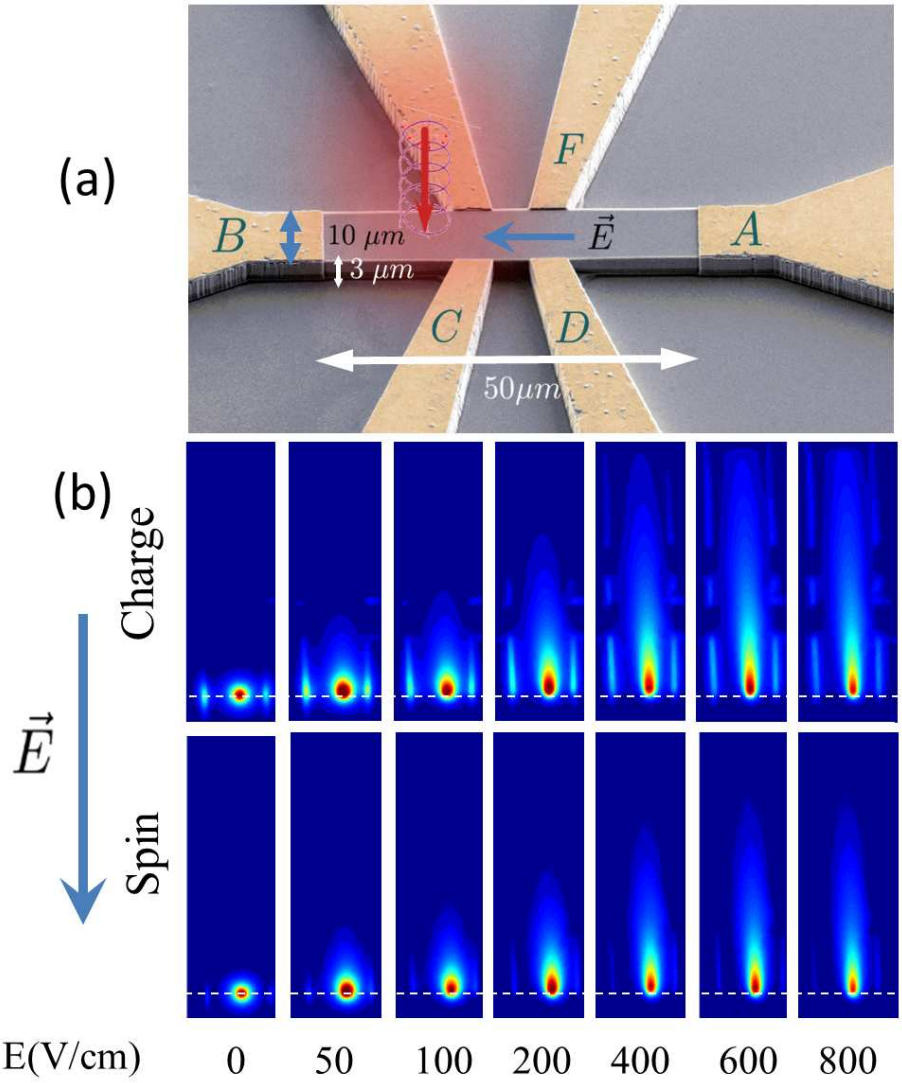


**Figure 4.8:** a) SEM image of the p-GaAs hall bar used to study minority carrier transport. b) Measured charge and spin spatial dependence at $T_L = 15$ K for different values of the applied electric field for a low power excitation of 0.1 $\mu W$ at excitation energy $h\nu = 1.55$ eV. In the direction of the electric field, the decay length is given by the drift length $L_d = E\mu\tau^{\text{eff}}$.

a sole explanation as due to the effect of electron temperature on $\mu\tau^{\text{eff}}$, we show that it is possible to tune $T_e$ without changing $T_h$ by adjusting the laser energy and the electric field.

Fig.4.11 shows the measured electron temperature $T_e(E)$ for the two laser excitation energies using the method described in sec.3.3.3. The temperature at zero field, related to the loss of energy to the phonons, is $T_e(0) = 40$ K and $T_e(0) = 92$ K for $h\nu = 1.55$ and 1.59 eV, respectively. Combination of the two excitation energies gives access to the range

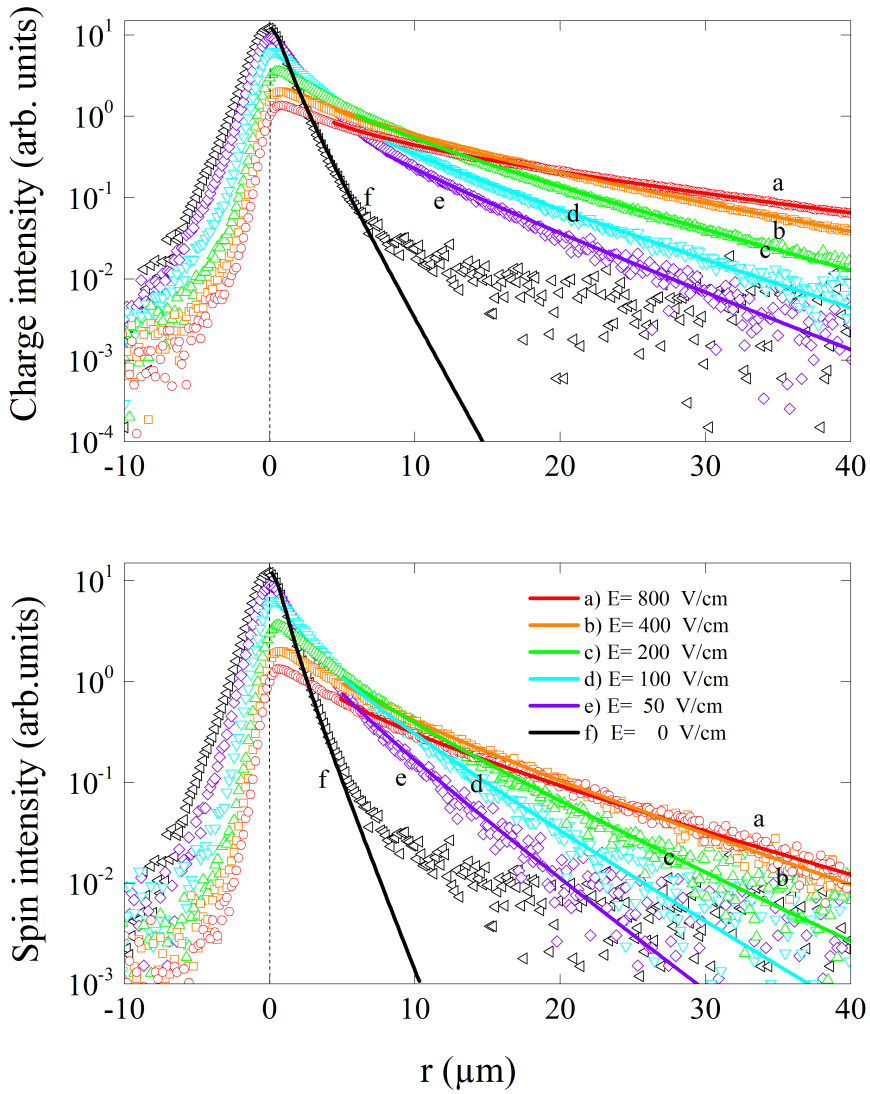


**Figure 4.9:** Charge and spin density profiles at $T_L = 15$ K obtained from the images of Fig.6.14 for selected values of the electric field. Full lines are fits obtained with Eq.(4.2) that give the $\mu_e \tau_e^{\text{eff}}$ and $\mu_s \tau_s^{\text{eff}}$ products for the charge and for the spin distribution, respectively.

40 K $< T_e <$ 130 K for $E$ between 0 and 1 kV/cm. The heating induced by the electric field can be simply explained by a competition between acceleration and relaxation of energy in a time $\tau_E$. The dashed lines in Fig. 4.11 are predictions based on the following simple balance equation for the energy delivered to the electron gas by the electric field:

$$3/2k_B[T_e(E) - T_e(0)] = qv_dE\tau_E \tag{4.3}$$

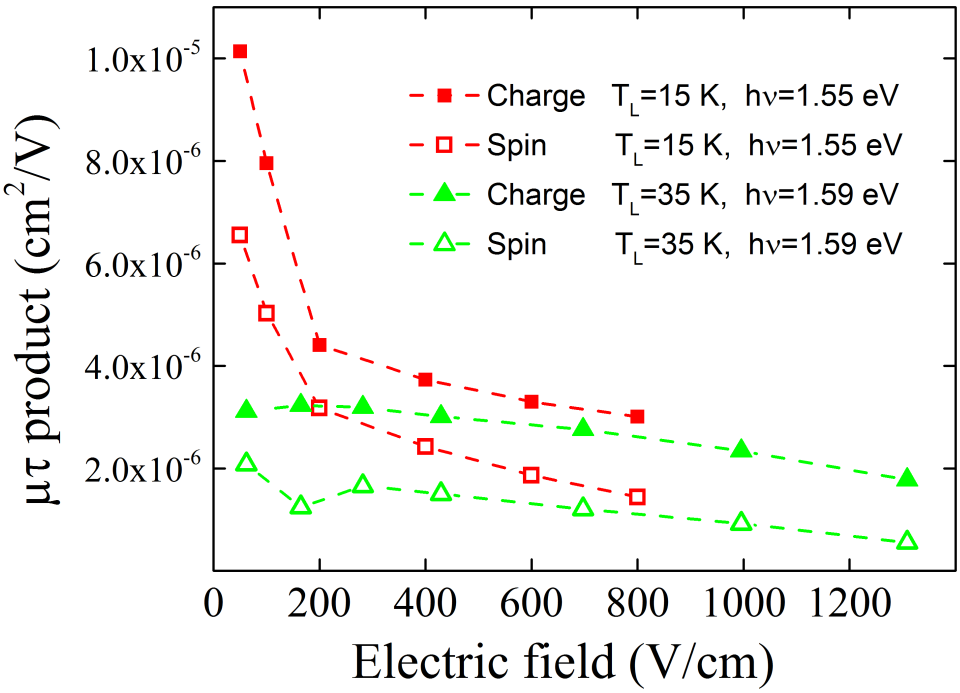


**Figure 4.10:** Measured $\mu\tau_{e(s)}^{\text{eff}}$ product for charge (spin) as a function of electric field. Full (open) squares correspond to $T_L = 15$ K and $h\nu = 1.55$ eV, whereas full (open) triangles correspond to $T_L = 35$ K and $h\nu = 1.59$ eV.

The quantity $v_d = \mu_e E$ is the drift velocity and $\tau_E$ is the energy relaxation time. The data are well explained by an energy-independent relaxation time of $\tau_E = 1.2$ ps and $\tau_E = 1.5$ ps for initial electron temperatures of $T_e(0) = 40$ K and $T_e(0) = 92$ K, respectively. These values are an order of magnitude larger than those measured at 300 K (Furuta et al. (1990)), consistent with a significant decrease of the energy relaxation rate at lower temperatures due to less efficient phonon scattering. Note that, as shown in Fig. 4.11, under the same conditions the resistivity very weakly changes, showing that the hole temperature ($T_h$) remains unchanged. This is confirmed by the low energy part and by the peak energy of the spectra, which are almost independent of the applied electric field (not shown) except for $E = 995$ V/cm at 1.59 eV excitation, where a moderate heating of the lattice is evident from the redshift of the spectrum. In contrast, the high energy tail, related to the electron distribution, is strongly perturbed by the electric field. This difference in the $E$-dependence of $T_e$ and $T_h$ is explained by a smaller hole mobility by at least two orders of magnitude and by a shorter phonon emission time (by about a factor of 2, according to Shah (1999)). Moreover, since the photogenerated hole concentration

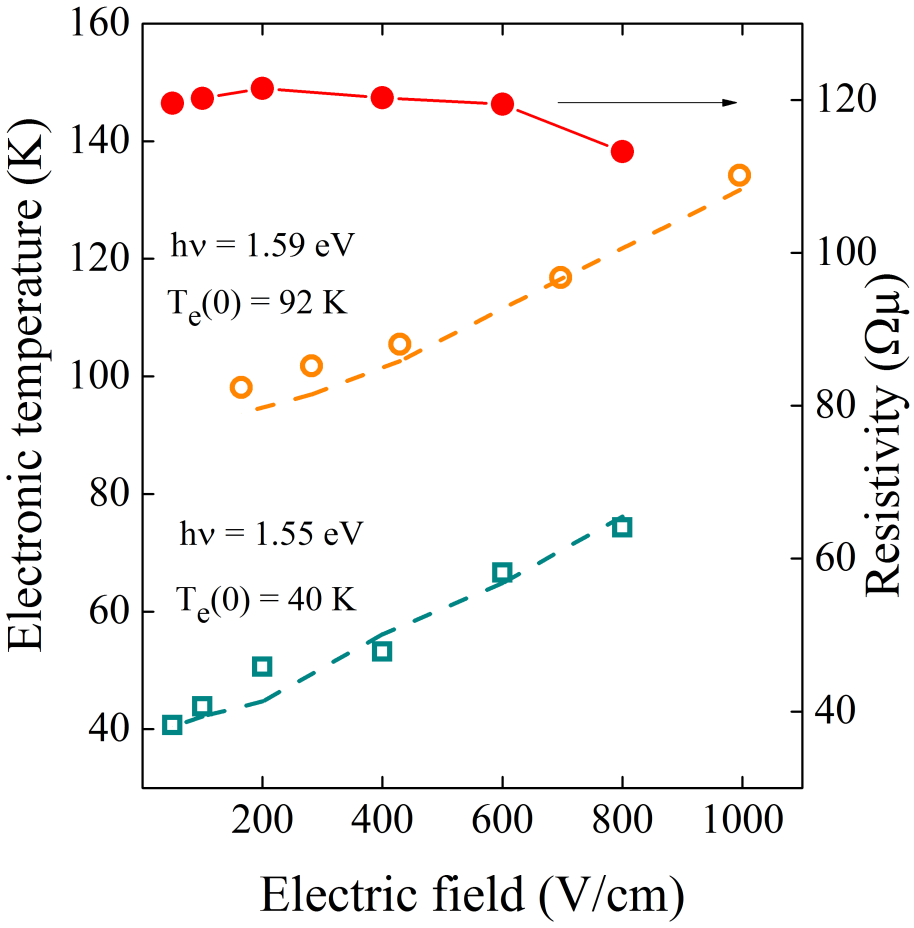


**Figure 4.11:** Measured $T_e$ as a function of applied electric field for laser excitation energies of 1.55 eV and 1.59 eV, respectively. The increase of $T_e$ a function of $E$ is well explained by Eq.(4.3) which assumes an energy-independent energy-relaxation time of 1.5 ps (dotted line) and 1.2 ps (solid line) for each case. Also shown (red dots) is the electric field dependence of the resistivity, which confirms that the hole temperature is only weakly affected by the electric field.

is much smaller than $N_A^-$, it is concluded that $T_h \approx T_L$ in all the experiments reported here.

The ability to change $T_e$ without changing $T_L$ using an applied electric field is now used to demonstrate that the charge and spin drift lengths are primarily determined by $T_e$. Figure 4.12 sumarizes the measured $\mu_e \tau_e^{\text{eff}}$ ($\mu_s \tau_s^{\text{eff}}$) product for the charge (spin) density as a function of electronic temperature. Remarkably, the values of the $\mu\tau$ product obtained when the lattice temperature varies in the range $T_L = 15 - 300$ K (full and open circles) are very similar to those obtained when the latter is fixed (full and open triangles). This striking result suggests that the lattice temperature has little influence on the electron

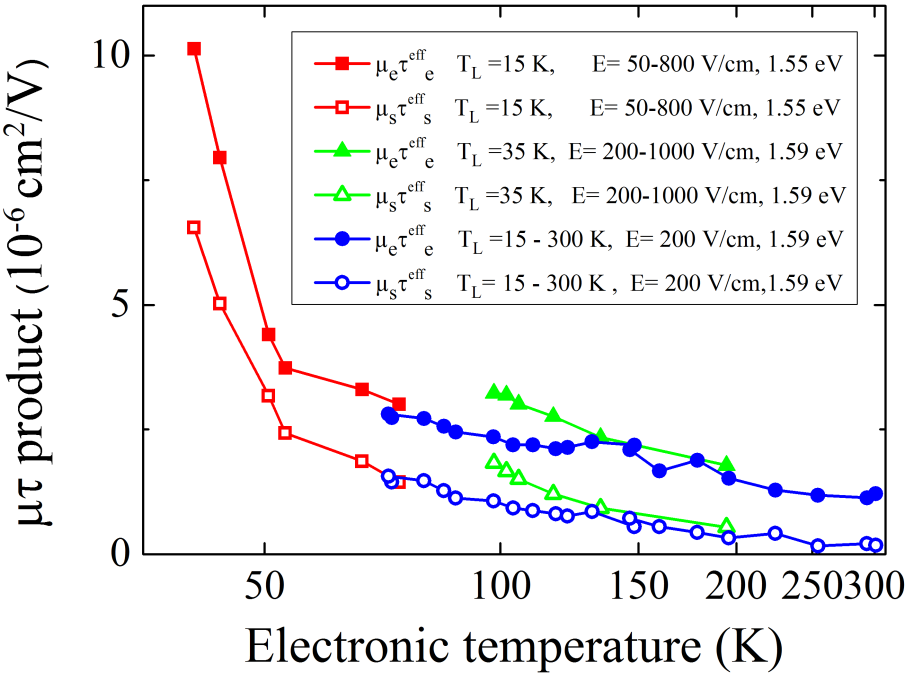


**Figure 4.12:** The $\mu\tau$ product for charge and spin as a function of electronic temperature, as obtained by fitting the luminescence profiles with Eq.(4.2). Circles were obtained at $E = 200$ V/cm and varying lattice temperature between $15 - 300$ K. Triangles correspond to $T_L \approx 35$ K and an electric field varying between $200 - 1000$ V/cm. The squares were obtained at $T_L = 15$ K and varying electric field between $50 - 800$ V/cm, and a lower excitation energy of 1.55 eV.

mobility, as will be confirmed in sec.4.2.5. Finally, the closed and open squares correspond to the case $T_L = 15$ K, excitation energy of 1.55 eV and varying electric field ($50 - 800$ V/cm). A sharp increase in the charge and spin $\mu\tau$ product is observed with decreasing electronic temperature.

Note finally that the product $\mu_s \tau_s^{\text{eff}}$ is consistently smaller than $\mu_e \tau_e^{\text{eff}}$. The analysis of sec.4.2.5 will show that $\mu_e \approx \mu_s$ and that this smaller value is entirely due to the smaller spin lifetime ($\tau_s^{\text{eff}} < \tau_e^{\text{eff}}$).

### 4.2.3 Time resolved photoluminescence measurements (TRPL)

Luminescence microscopy has been used in order to determine the effective charge and spin diffusion lengths $L^{\text{eff}} = \sqrt{D\tau^{\text{eff}}}$ (sec.4.2.1), as well as the $\mu\tau^{\text{eff}}$ product for both species

(sec.4.2.2). However, the diffusion and drift currents, described by Fick's law [Eq.(1.1)] and Ohm's law [Eq.(1.2)], respectively, depend on the diffusion constant $D$ and on the mobility $\mu$. Here, I present time-resolved measurements that will allow us, together with the results discussed in sec.4.2.1 and sec.4.2.2, to determine the effective charge and spin lifetimes, and therefore, all the relevant transport parameters.

For the TRPL measurements, performed at the Laboratoire de Physique et Chimie des Nano-objets (Toulouse), and as described in Zhang et al. (2013), the excitation source was a circularly-polarized mode-locked frequency-doubled Ti:Sa laser (1.5 ps pulse width and 80 MHz repetition frequency) and the resulting luminescence was dispersed by a spectrometer and detected by a streak camera as a function of time after the pulse. Both the total light intensity $I_s(t)$ and the difference signal $I_d(t)$ (as defined by Eq.(3.1)) were monitored. The transient charge and spin signals have been measured as a function of temperature, and are shown in Fig.4.13. After an initial increase for $t < 100$ ps after the laser pulse, probably due to electron thermalization to the bottom of the conduction band, the transient signals decay with at least 2 exponential modes. At long times, the decay is governed by a single exponential. This decay at long times corresponds to the effective lifetime that determines the diffusion length in the steady state luminescence imaging. As can be seen from the left panel of Fig.4.13, the time $\tau_e^{\text{eff}}$ of the long time transient increases with temperature. This shows that $\tau_e^{\text{eff}}$ is dominated by the decrease with temperature of the bulk recombination efficiency (Ahrenkiel (1993)) rather than by the increase of surface recombination velocity $S$.

The right panel of Fig. 4.13 shows the temperature dependence of the difference signal. Up to about 80 K, the time $\tau_s^{\text{eff}}$ of the long time transient increases with temperature, in the same way as for the sum transient. Further temperature increase induces a decrease of $\tau_s^{\text{eff}}$, which reveals a temperature decrease of the spin relaxation time $T_1$. It is noted that, in agreement with independent observations (Horinaka et al. (1995)), the characteristic time for the rise of the two signals weakly depends on temperature. The values of the characteristic times for the slowest decay of the transient signals, $\tau_e^{\text{eff}}$ and $\tau_s^{\text{eff}}$, as obtained from an inverse Laplace analysis, are summarized in Table 4.2, together with the spin lifetime $T_1$ obtained from the single exponential decay of the circular polarization of the

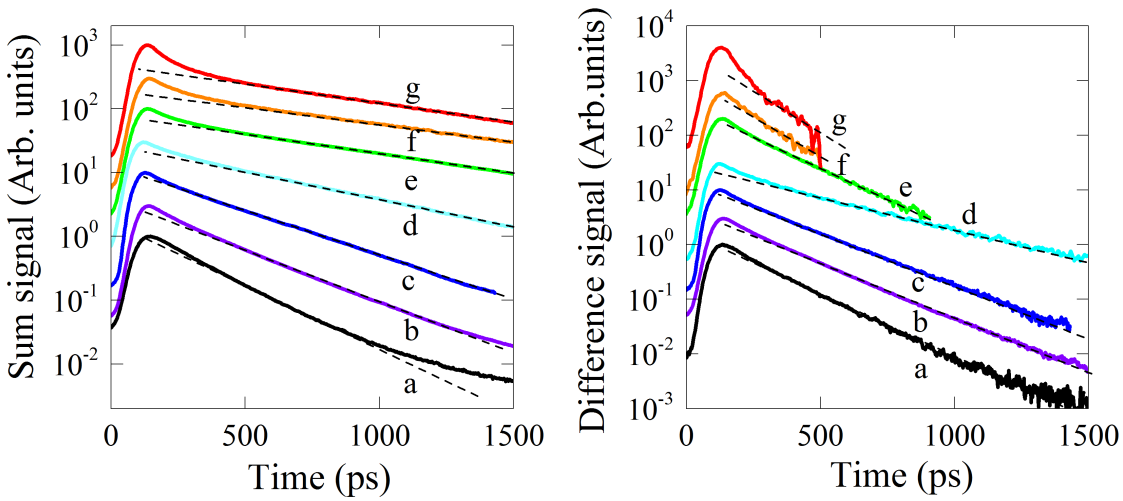


**Figure 4.13:** Temperature effects investigated using TRPL. The left panel shows the experimentally-observed transient sum signals observed for selected lattice temperatures of 9 K,(a) 20 K,(b) 40 K,(c) 80 K,(d) 150 K,(e) 225 K,(f) and 300 K (g). These curves were normalized and shifted upwards for clarity, and regions of very large noise have been omitted. The right panel shows the corresponding difference transients.

**Table 4.2:** Measured lifetimes for selected temperatures.

| $T_e$ | $T_L$ | $\tau_e^{\text{eff}} \pm 10$ (ps) | $\tau_s^{\text{eff}} \pm 10$ (ps) | $T_1 \pm 10$ (ps) |
|---|---|---|---|---|
| 22 | 9 | 189 | 163 | 1199 |
| 33 | 20 | 256 | 209 | 1147 |
| 48 | 40 | 319 | 251 | 1180 |
| 100 | 80 | 524 | 256 | 502 |
| 150 | 150 | 717 | 212 | 302 |
| 225 | 225 | 796 | 146 | 179 |
| 300 | 300 | 717 | 170 | 222 |

luminescence (not shown).

The temperature dependence of $T_1$ is shown in Fig.4.14. A power law is found, with $T_1 \propto T_e^{-1.2}$ and $T_1 \propto T_L^{-1}$. The $T_e$ dependence is close to that found using Hanle effect measurements for a similar doping by Zerrouati et al. (1988), which indicates a dominant relaxation mechanism that is determined by the interaction of the electronic spins with the hole spins known as the Bir Aronov Pikus mechanism (Bir et al. (1975)). Also shown in the inset of Fig. 4.14, is the temperature dependence of the effective charge and spin lifetimes. A detailed analysis (discussed in Cadiz et al. (2014)) shows that the difference between $\tau_e$ (bulk lifetime) and $\tau_e^{\text{eff}}$ is only significant at temperatures larger than 100 K, above which the surface recombination velocity starts to play a role. The value of $\tau_e^{\text{eff}}$ at

300 K is smaller by a factor of 3 than the bulk radiative lifetime for the present acceptor concentration (Nelson and Sobers (1978)), and the temperature increase is characterized by an exponent of the order of 0.7, which is smaller than the one found for bulk radiative recombination (Ahrenkiel (1993)). These two differences are attributed to nonradiative bulk recombination, for which the time decreases with increasing temperature. The increase of bulk nonradiative recombination may also explain the saturation in $\tau_e^{\text{eff}}$ near 300 K.

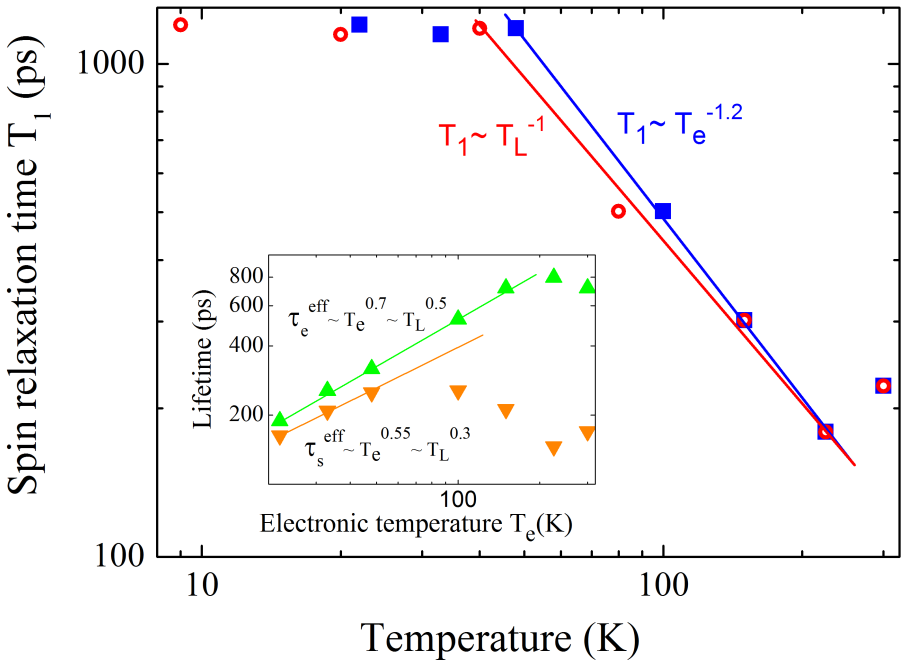


**Figure 4.14:** Dependence of the spin relaxation time $T_1$ as a function of both the lattice temperature ($T_L$) and the electronic temperature ($T_e$). $T_1$ follows a power law for temperatures above 40 K, for which the exponent as a function of $T_e$ is $-1.2$, close to the one predicted by the Bir Aronov Pikus model. Shown in the inset are the electronic temperature dependences of the long time constant for charge and spin $\tau_e^{\text{eff}}$, $\tau_s^{\text{eff}}$.

### 4.2.4 Determination of the diffusion constants

The TRPL technique alone permits, in principle, to determine all the transport parameters, by performing a detailed study of the higher order modes of the transient decay at short times, which depends on $D$, $S$ and the sample thickness $d$ (see appendix 8.1.3). Despite the potential of this technique, little information has been so far gained on charge

**Table 4.3:** Measured diffusion constants for selected temperatures.

| $T_e$ | $D_e \pm 15$ cm$^2$/s | $D_s \pm 15$ cm$^2$/s |
|---|---|---|
| 40 | 70.8 | 61 |
| 50 | 46 | 48 |
| 70 | 49 | 55 |
| 102 | 53 | 53 |
| 130 | 48 | 60 |
| 161 | 48 | 62 |
| 195 | 49 | 51 |
| 292 | 60 | 50 |

and spin diffusion since higher order modes are partly masked by the slow increase of the PL signal. The diffusion constants at 300 K are usually obtained from the values of minority carrier mobilities (Lowney and Bennett (1991)) for which investigations as a function of temperature are very scarce (Lovejoy et al. (1995); Beyzavi et al. (1991)). In this section, we combine the time-resolved measurements of sec.4.2.3 with the spatially resolved microluminescence of sec.4.2.1 in order to perform a systematic investigation of the various relevant parameters for charge and spin transport. In order to do this, it is noted that the measured effective diffusion length, determined with the microluminescence technique in sec.4.2.1, is given by

$$L_{e(s)}^{\text{eff}} = \sqrt{D_{e(s)}\tau_{e(s)}^{\text{eff}}} \tag{4.4}$$

where $\tau_{e(s)}^{\text{eff}}$ indeed corresponds the characteristic time of the decay transient at long times (see appendix 8.1.1). At $T_e = 50$ K, from table 4.1 it is found that $L_e^{\text{eff}} = 1.24 \pm 0.05$ $\mu$m and $L_s^{\text{eff}} = 1.10 \pm 0.05$ $\mu$m. By using the (interpolated) lifetimes in table 4.2, $D_e = 46 \pm 15$ cm$^2$/s, and $D_s = 48 \pm 15$ cm$^2$/s, are found. By using Eq.(8.15), one also obtains a small recombination velocity $S \sim 5 \times 10^4$ cm/sec but, since the bulk electronic lifetime $\tau_e$ is very close to $\tau_e^{\text{eff}}$ at this temperature, the uncertainty on this determination is very large, of at least one order of magnitude.

The values of $D_e$ and $D_s$ are shown in Fig.4.15, where it can be seen that they only weakly depend on temperature. Values for selected electronic temperatures are listed in Table. 4.3.

Note that, since $D_e$ is approximately constant, the Einstein relation [Eq.(2.6)] predicts a $\sim 1/T_e$ dependence of the mobility. This will be confirmed in sec.4.2.5. This is an interesting result, since until now it was largely assumed that the minority electron mobility in

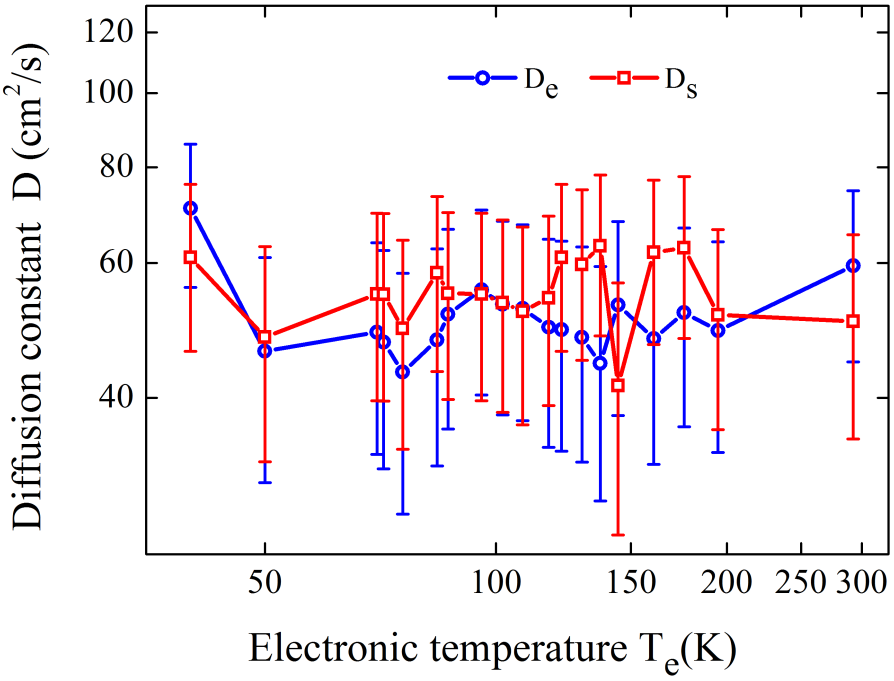


**Figure 4.15:** Measured charge and spin diffusion constants as a function of electronic temperature. Within error bars, $D_e = D_s$ so that spin coulomb drag is negligible (D'Amico and Vignale (2000)).

highly doped GaAs is mainly determined by the lattice temperature (Lovejoy et al. (1995); Kaneto et al. (1993)).

### 4.2.5 Determination of the mobility

By combining the $\mu\tau^{\text{eff}}$ product measured in sec.4.2.2 with the effective lifetimes of sec.4.2.3, an estimate of the charge, $\mu_e$, and spin, $\mu_s$, mobility is made. At $T_L = 300$ K, $\mu_e = 1560$ cm$^2$V$^{-1}$s$^{-1}$ is obtained, in excellent agreement with the theoretical value of 1643 cm$^2$V$^{-1}$s$^{-1}$ at similar doping densities predicted by Bennett (2002) and with the existing experimental data (Harmon et al. (1993); Colomb et al. (1992); Beyzavi et al. (1991); Ahrenkiel et al. (1987)). Fig.4.16 shows that, above 70 K, a clear $1/T_e$ dependence is observed for both the electron (closed circles) and spin (open circles) mobility. This suggests that what determines minority carrier mobility is mostly their own temperature, rather than that of majority carriers. This hypothesis can be tested by measuring the $T_e$-dependence of the mobilities when, as described in Fig. 4.11, $T_e$ is varied by changing the electric field while $T_L$ is held constant. The triangles in Fig. 4.16 correspond to

$T_L \approx 35$ K while the squares correspond to $T_L = 15$ K. For 100 K $< T_e <$ 200 K the charge and spin mobility dependence is well fitted by a $T_e^{-1.3}$ law. It is striking to see that the measured mobility values at fixed $T_L$ are close to those obtained when $T_L$ also varies between 50 K and 200 K (circles). This shows that, in this range, the minority carrier mobility weakly depends on $T_L$. The squares in Fig. 4.16 correspond to $T_L \approx 15$ K and $T_e < 50$ K. In this range, there is a dramatic increase of mobility, with both electron and spin mobilities being described by a $T_e^{-4.3}$ power law.

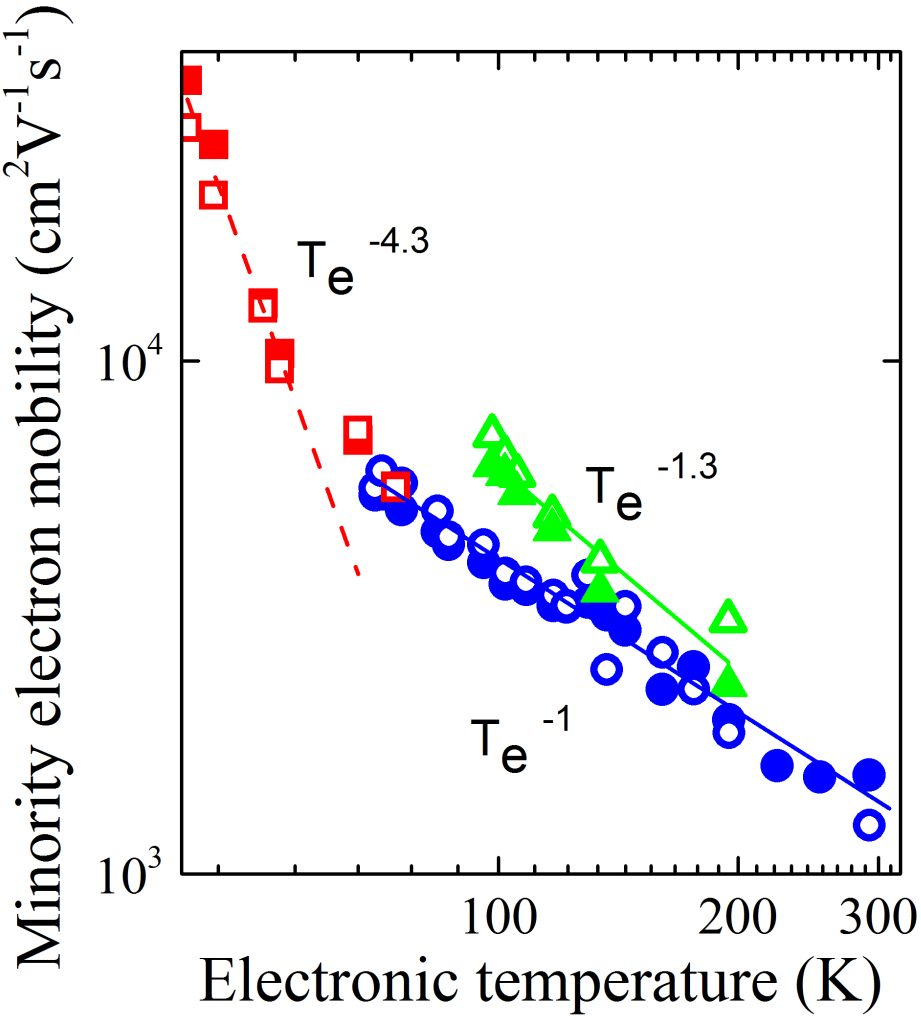


**Figure 4.16:** The measured electron (solid circles) and spin (open circles) mobilities, $\mu_e$ and $\mu_s$ for an electric field of 200 V/cm as a function of $T_L$. Both show a $1/T_e$ variation for $T_e \geq 70$ K. Also shown are the dependences of $\mu_e$ and $\mu_s$ at fixed $T_L$, found by varying $T_e$ using the electric field only. The solid and open triangles correspond to $\mu_e$ and $\mu_s$, respectively, for $T_L \approx 30 - 40$ K and an electric field varying between $200 - 1000$ V/cm. The solid and open squares correspond to $\mu_e$ and $\mu_s$, respectively, at $T_L = 15$ K. At low $T_e$ a dramatic increase of the mobility is observed, with a $1/T_e^{4.3}$ dependence.

**Table 4.4:** Measured charge and spin mobilities for selected temperatures.

| $T_e$ | $\mu_e \pm 500$ cm$^2/V$/s | $\mu_s \pm 500$ cm$^2/V$/s |
|---|---|---|
| 40 | 35200 | 28400 |
| 50 | 13370 | 12644 |
| 70 | 6740 | 5700 |
| 102 | 4120 | 3600 |
| 130 | 3530 | 3717 |
| 161 | 2290 | 2700 |
| 195 | 2000 | 1880 |
| 292 | 1560 | 1250 |

In Table 4.4, a list of the measured charge and spin mobilities for selected electronic temperatures can be found. For the $T_e > 70$ K range, the data shown as circles in Fig. 4.16 is used.

The minority electron mobility features a completely different temperature dependence than that of majority electrons in n-GaAs for a similar doping level (Beyzavi et al. (1991); Luber et al. (2006); Schultes et al. (2013)). A number of possible reasons for this have been discussed in the literature, including carrier freezeout at high hole concentrations (Kim et al. (1997); Lovejoy et al. (1995)), screening of ionized impurities (Walukiewicz et al. (1979)) and increasing hole degeneracy as temperature is lowered (Kaneto et al. (1993)). All these works simply ignore the possible difference between the electronic and the hole (lattice) temperatures, and they mention just one common temperature, $T$. The experimental results are not explained by current theoretical models. The main message is that the energy dependence of the scattering time is, at the present, not clear at all.

The weak dependence of electron mobility on $T_L$ suggests that the mechanism which limits the mobility is scattering by charged impurities and holes, whose density is $T_L$ independent (see sec.4.2.5), rather than phonon scattering. This conclusion is also supported by theoretical considerations at the high doping levels used here (Kaneto et al. (1993); Tea and Aniel (2011)). The origin of the $T_e$ dependence of the minority electron mobility is at present not understood. In the Brooks-Herring formalism which considers mostly electron-electron screening (Chattopadhyay and Queisser (1981)), $\mu_e(T_L, T_e)$ depends on the screening length, which itself depends on the temperature. At the doping levels considered here it is probable that the mobility is determined by scattering by potential fluctuations caused by the random distribution of ionized acceptors and of their

screening by valence holes rather than by individual charges. For a hole temperature of $T_h = 10$ K the maximum amplitude of the potential fluctuations is of the order of 40 meV (Efros et al. (1972)) and while some attempts have been made to include the effects of screening on transport (Kaneto et al. (1993); Chattopadhyay and Queisser (1981); Quang et al. (1993)), a complete description including the effect of disorder is still out of reach.

### 4.2.6 Verification of the Einstein relation

The Einstein relation [Eq.(2.6)], relating the electron's diffusion constant $D_e$ with the averaged momentum relaxation time $\tau_m$, is a special case of the fluctuation-dissipation theorem that can be written in the following form, assuming Boltzmann's statistics for the electron gas. It is reproduced here:

$$D_e = [\frac{k_B T_e}{q}]\mu_e = \frac{k_B T_e \tau_m}{m^*}$$

Diffusion and drift are therefore strongly related via microscopic scattering processes. The open circles of Fig.4.17 represent the averaged diffusion constant $\langle D \rangle = 1/2(D_e + D_s)$, that was obtained in sec.4.2.4 by combining the charge and spin diffusion lifetimes with their respective diffusion lengths. Also shown as full circles is the average diffusion constant obtained via the average measured mobility $\langle \mu \rangle = 1/2(\mu_e + \mu_s)$ of sec.4.2.5 and by using the Einstein relation. It is seen that the diffusion constant obtained by using the measured mobility is systematically smaller than the one obtained with the diffusion lengths, except at the lowest temperatures.

This difference may indicate an inherent problem when measuring the different transport parameters under different experimental conditions. While the lifetimes of TRPL and the drift/diffusion lengths of the microluminescence imaging were combined at equal electron temperature, they were measured at different lattice temperatures. This difference may be unavoidable when a steady state electron gas is compared to an electron gas created by a laser pulse. Even in the simplest possible situation in which $D_e$ and $\mu_e$ are only functions of $T_e$, a difference in $T_L$ could lead to a systematic error in the measured parameters. For example, the radiative recombination time is expected to depend on both the electron

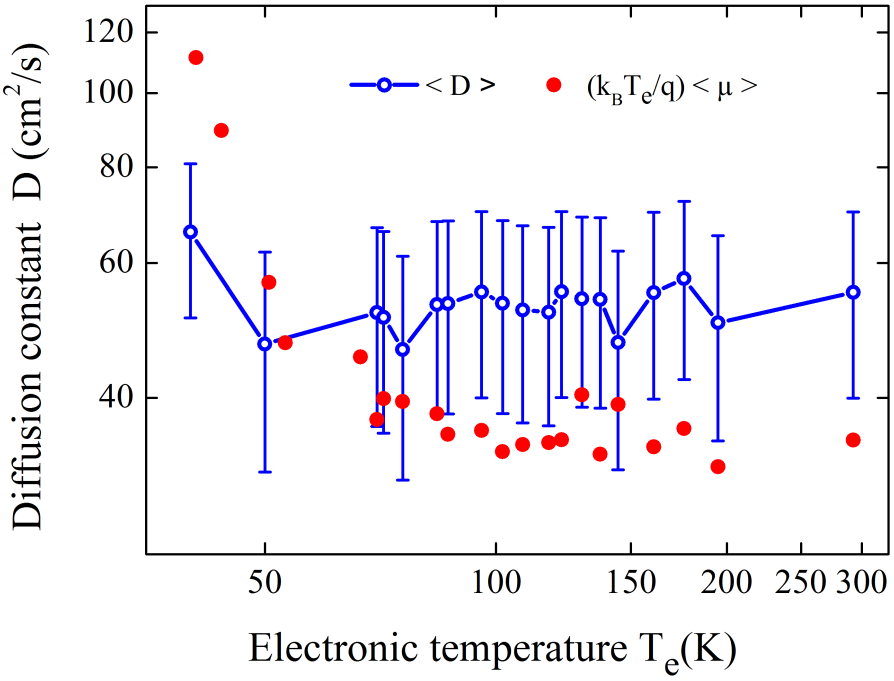


**Figure 4.17:** Measured mean diffusion constant as a function of electronic temperature. The open circles were obtained by combining the measured effective lifetimes with the effective diffusion lenght, wereas the full circles were obtained by the measured mobility and using the Einstein relation [Eq.(2.6)].

and the hole statistics, so that $\tau^{\text{eff}}_{e(s)} = \tau^{\text{eff}}_{e(s)}(T_e, T_L)$. The same electronic temperature $T_e$ was obtained with a lattice temperature of $T_L$ in the microluminescence experiments, and with a different temperature $T_L^*$ in the time-resolved measurements (See Table. 4.1 and Table.4.2 for comparision). Therefore, the diffusion constant and the mobility, calculated by

$$D_{e(s)}(T_e) = [L^{\text{eff}}_{e(s)}(T_e, T_L)]^2 / \tau^{\text{eff}}_{e(s)}(T_e, T_L^*) \tag{4.5}$$

$$\mu_{e(s)}(T_e) = [\mu_{e(s)}(T_e)\tau^{\text{eff}}_{e(s)}(T_e, T_L)] / \tau^{\text{eff}}_{e(s)}(T_e, T_L^*) \tag{4.6}$$

are only approximate when $T_L^* \neq T_L$.

## 4.3 Mode structure analysis of the TRPL at short times

It is shown here that analysis of the TRPL transient at short times gives further proof that $D_e \approx D_s$. In a TRPL experiment, the photoelectron concentration depends on depth and time and is a solution of the time-dependent diffusion equation, solved in Appendix 8.1.3. It can be shown that the PL sum intensity is given by:

$$I_{\mathrm{TRPL}}(t) = K \int_0^d e^{-\alpha_l z} n(z,t) dt = K \sum_m d_m e^{-t/\tau_m} \tag{4.7}$$

where $\alpha_l$ is the absorption coefficient at the luminescence energy, $K$ is a constant, and the coefficients $d_m$ of the various modes only depend on $Sd/D_e$, $S'd/D_e$, $\alpha$ and $\alpha_l$ (see Eq.(8.30)). $S$ and $S'$ are the recombination velocities at the front and at the back surface, respectively. The characteristic times $\tau_m$ of the various modes are given by

$$1/\tau_m = 1/\tau + D_e \alpha_m^2 / d^2 \tag{4.8}$$

where the angle $\alpha_m$ is given by the nonlinear equation (8.11) shown in the Appendix 8.1.3. The difference signal $I_d(t)$ is given by Eq.(4.7) where the charge concentration $n$ is replaced by the spin concentration $s$, the quantity $K$ is replaced by $K|\mathscr{P}_i|$, and $D_e$ is replaced by the spin diffusion constant $D_s$ in Eq.(4.8). Within these changes, Eq.(4.7) also gives the expression for $I_d(t)$, as a function of the characteristic times $\tau_{sm}$ of the various modes for the decay of $s$.

Fig.4.18 shows the sum and difference transients (black curves) obtained at $T_L = 20$ K for which $T_e = 33$ K, as well as the response of the streak camera (dashed line) and the analysis of the transients using exponential decay modes. It is seen that both signals initially increase for $t \leq t_0$, where $t_0$, of the order of 100 ps, is the time required for the electron gas to cool down to the bottom of the conduction band. After $t_0$, both transient signals decrease according to Eq.(4.7) with at least 2 modes clearly identified. A convenient method to find these modes is to perform an inverse Laplace transform (Cadiz et al. (2014)). Shown in the insets of Fig. 4.18, are the two first modes of the sum and difference signals corresponding to the two well-defined peaks of the inverse Laplace

transform. It is possible to write then a two-mode expansion of the signal:

$$I_s(t-t_0) = c_1^* e^{(t-t_0)/\tau_1} + (1-c_1^*)e^{(t-t_0)/\tau_2} \tag{4.9}$$

with $\tau_1 = 256$ ps, $\tau_2 = 66$ ps, and $c_1^* = 0.82$. In the same way, the difference signal is described by

$$I_d(t-t_0) = c_{s1}^* e^{(t-t_0)/\tau_{s1}} + (1-c_{s1}^*)e^{(t-t_0)/\tau_{s2}} \tag{4.10}$$

with $\tau_{s1} = 215$ ps, $\tau_{s2} = 63$ ps and $c_{s1}^* = 0.725$. The data are indeed very well approximated by the sums (Curves $c$) of these two modes (Curves $d$ and $e$, respectively).

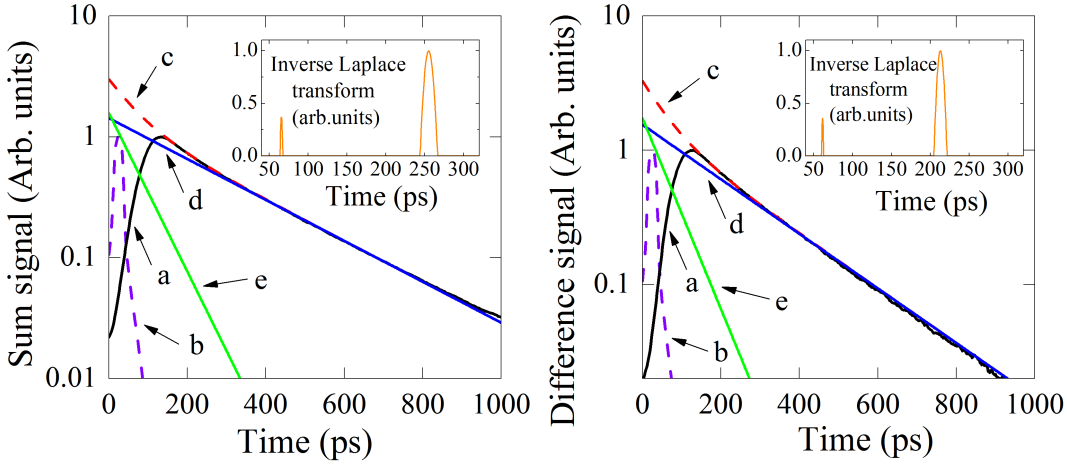


**Figure 4.18:** Sum (left panel) and difference (right panel) TRPL signals and their analysis. Curves $a$ shows the measured transient at $T_L = 20$ K ($T_e = 33$ K), normalized at its maximum, to be compared with the detector response shown in Curves $b$. The inset reveals two exponential decay modes and gives their characteristic times and weights. The sum of these exponentials, shown in Curves $c$, gives a very good approximation to the decay signal at times larger than about 100 ps after the laser pulse. These exponentials are shown individually in Curves $d$ and $e$.

Alternative interpretations implying ambipolar diffusion (Paget et al. (2012)), Auger recombination at high density, change of recombination time caused by temperature dependence of the bimolecular recombination (Ahrenkiel (1993); Dumke (1963)), or stimulated emission by the photoexcited carriers, can be ruled out based on the very weak dependence of the transient on excitation power. In the same way, transient dielectric screening of carriers can also be ruled out since the dielectric relaxation time is 7 ps for an electron concentration of $10^{15}$ cm$^{-3}$, and is smaller at larger concentrations.

### 4.3. Mode structure analysis of the TRPL at short times

The relatively slow increase of the sum and difference signals appearing in Fig.4.13, on a time of the order of 100 ps, is comparable with $\tau_2$. Increases with similar time constants, which mask higher order modes, have been attributed to the screening of the electron-phonon interaction (Seymour et al. (1982),Horinaka et al. (1995)). Moreover, it is difficult to determine the values of the amplitudes $c_1$ and $c_2$ and therefore $\gamma = Sd/D$ according to Fig.8.5, since they obviously depend on the origin $t_0$ which is chosen. It is thus concluded that the sole determination of $\tau_1$ and $\tau_2$ is not sufficient to determine intrinsic dynamic parameters.

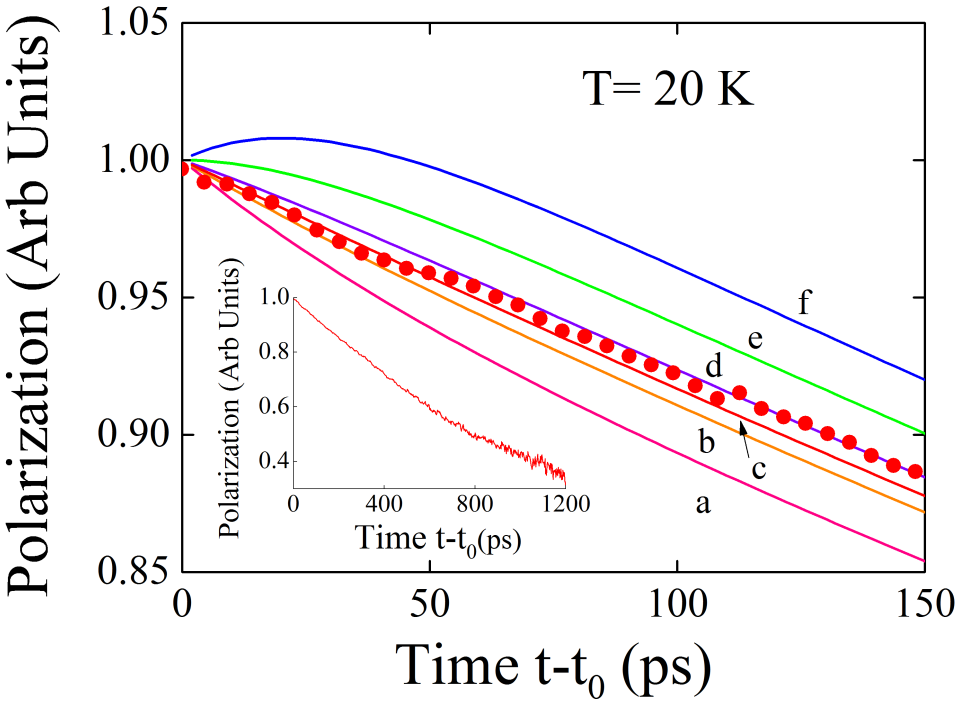


**Figure 4.19:** The inset shows the light polarization transient taking the time of the maximum $t_0$ in the TRPL signals as the time origin. This transient mostly exhibits a single exponential. The dots show the same transient at short times. The curves are calculated using Eq.(4.7) taking a ratio $D_s/D_e$ of the spin to charge diffusion constants equal to 0.3 (a), 0.9 (b), 1 (c), 1.1 (d), 1.3 (e), and 1.5 (f). From the almost ideal exponential behavior of the transient, it is concluded that $D_s/D_e = 1 \pm 0.1$.

However, comparison between the sum and difference transients permits to show that $D_e = D_s$. This is performed by calculating their ratio, which is the transient spin polarization $\mathscr{P}(t) = s(t)/n(t)$. This transient is shown in the inset of Fig.4.19, taking the time

origin at $t_0 = 150$ ps in order to avoid the effects of the slow signal increase. The fast decay has almost completely disappeared and the transient is described by a single slow exponential of characteristic time $T_1 \approx 1050$ ps. It can be shown using Eqs.(4.7),(4.9) and (4.10), that the only explanation of such a finding is that $D_s \approx D_e$. Also shown in Fig. 4.19 are the transients calculated using Eq.(4.7) for several values of the ratio $D_s/D_e$. The best agreement is in fact obtained for $D_s/D_e$ between 0.9 and 1. It will be indeed shown in the following chapter that Coulomb spin drag is negligible because of screening of electron-electron interactions.

## 4.4 Conclusions

A new approach was used for investigating charge and spin diffusion in semiconductors (as well as surface and bulk recombination, which is not discussed in this manuscript, Cadiz et al. (2014)). Combination of TRPL and spatially-resolved luminescence gives the bulk recombination time $\tau_e$ and the spin relaxation time $T_1$ and, subsequently, the charge and spin diffusion constants and mobilities. This is because a single effective recombination time $\tau^{\text{eff}}$ taking account of surface and bulk recombination characterizes the long time decay transient of TRPL, as well as the diffusion and drift length measured using spatially-resolved luminescence.

The charge and spin diffusion constants and mobilities of a p-GaAs sample were obtained as a function of temperature, as well as $\tau_e^{\text{eff}}$, $\tau_s^{\text{eff}}$ and $T_1$. By using electric fields to increase the photoelectron temperature $T_e$ without significantly changing the hole or lattice temperatures, the charge and spin mobilities are shown to be principally dependent on $T_e$. For $T_e > 70$ K both the charge and spin mobilities vary as $T_e^{-1.3}$ while at lower temperatutes this changes to an even more rapid $T_e^{-4.3}$ law.

This finding shows that current models for minority carrier mobility, accounting for the hole distribution alone, as proposed by Kaneto et al. (1993), cannot describe the observed temperature dependence of the minority electron mobility since significant variations are measured even when the hole temperature is kept constant. The inclusion of minority

**Table 4.5:** Transport parameters at $T_e = 50$ K, $T_L = 15$ K.

| | | |
|---|---|---|
| Diffusion constant | $D_e \approx D_s$ | 45 cm$^2$/s |
| Charge effective lifetime | $\tau_e^{eff}$ | 335 ps |
| Minority electron mobility | $\mu_e \approx \mu_s$ | 12500 cm$^2$/V/s |
| Spin effective lifetime | $\tau_s^{eff}$ | 251 ps |
| Spin relaxation time | $T_1$ | 1125 ps |
| Surface recombination velocity | S | $4.6 \times 10^4$ cm/s |
| Majority hole mobility | $\mu_h$ | 100 cm$^2$/V/s |
| Hole Diffusion constant | $D_h$ | 0.13 cm$^2$/V/s |
| Ionized acceptor density | $N_A^-$ | $10^{18}$ cm$^{-3}$ |

carrier statistics in theoretical models is therefore necessary to better understand minority carrier mobilities in doped semiconductors.

The results obtained in sec.4.2.1, 4.2.2 and 4.2.3, give the transport parameters of Table.4.5 at $T_e = 50$ K, which is the measured electronic temperature in the experiments that will be described in Chapter 6. Note that the surface recombination velocity $S$ cm/s, is almost a factor of 10 smaller than the diffusion velocity $D_e/d \approx 2.73 \times 10^5$ cm/s so that surface recombination is negligible in this sample at low temperatures. The results of this chapter determines all the parameters necessary to understand the Pauli blockade effects in Chapter 6.

## 4.4. Conclusions

### 4.4.1 Publications related to this chapter

JOURNAL OF APPLIED PHYSICS **116**, 023711 (2014)

# All optical method for investigation of spin and charge transport in semiconductors: Combination of spatially and time-resolved luminescence

F. Cadiz,[1] P. Barate,[2] D. Paget,[1] D. Grebenkov,[1] J. P. Korb,[1] A. C. H. Rowe,[1] T. Amand,[2] S. Arscott,[3] and E. Peytavit[3]
[1]*Physique de la matière condensée, Ecole Polytechnique, CNRS, 91128 Palaiseau, France*
[2]*Université de Toulouse, INSA-CNRS-UPS, 31077 Toulouse Cedex, France*
[3]*Institut d'Electronique, de Microélectronique et de Nanotechnologie (IEMN), University of Lille, CNRS, Avenue Poincaré, Cité Scientifique, 59652 Villeneuve d'Ascq, France*

(Received 12 May 2014; accepted 27 June 2014; published online 14 July 2014)

A new approach is demonstrated for investigating charge and spin diffusion as well as surface and bulk recombination in unpassivated doped semiconductors. This approach consists in using two complementary, conceptually related, techniques, which are time-resolved photoluminescence (TRPL) and spatially resolved microluminescence ($\mu$PL) and is applied here to $p^+$ GaAs. Analysis of the sole TRPL signal is limited by the finite risetime. On the other hand, it is shown that joint TRPL and $\mu$PL can be used to determine the diffusion constant, the bulk recombination time, and the spin relaxation time. As an illustration, the temperature variation of these quantities is investigated for $p^+$ GaAs. © *2014 AIP Publishing LLC*. [http://dx.doi.org/10.1063/1.4889799]

APPLIED PHYSICS LETTERS **106**, 092108 (2015)

# Central role of electronic temperature for photoelectron charge and spin mobilities in $p^+$-GaAs

F. Cadiz,[1,a)] D. Paget,[1] A. C. H. Rowe,[1] E. Peytavit,[2] and S. Arscott[2]
[1]*Physique de la Matière Condensée, Ecole Polytechnique, CNRS, 91128 Palaiseau, France*
[2]*Institut d'Electronique, de Microélectronique et de Nanotechnologie (IEMN), University of Lille, CNRS, Avenue Poincaré, Cité Scientifique, 59652 Villeneuve d'Ascq, France*

(Received 28 January 2015; accepted 25 February 2015; published online 6 March 2015)

The charge and spin mobilities of minority photoelectrons in $p^+$-GaAs are determined by monitoring the effect of an electric field on the spatial profiles of the luminescence and of its polarization. By using electric fields to increase the photoelectron temperature $T_e$ without significantly changing the hole or lattice temperatures, the charge and spin mobilities are shown to be principally dependent on $T_e$. For $T_e > 70$ K, both the charge and spin mobilities vary as $T_e^{-1.3}$, while at lower temperatures this changes to an even more rapid $T_e^{-4.3}$ law. This finding suggests that current theoretical models based on degeneracy of majority carriers cannot fully explain the observed temperature dependence of minority carrier mobility. © *2015 AIP Publishing LLC*. [http://dx.doi.org/10.1063/1.4914357]

# Chapter 5

# Charge and spin diffusion of degenerate electrons: theoretical framework

In this chapter, we will discuss the different coupling mechanisms that may appear in the charge and spin coupled diffusion equations due to Pauli Blockade. When a semiconductor is excited with a local, high power light excitation, three effects may change the situation with respect to the low density diffusion studied in Chapter 4; i) local heating of the electron gas may cause a temperature gradient which leads to thermal currents, ii) at high density, Coulomb coupling with photoholes can influence diffusion of spin polarized electrons (ambipolar diffusion), iii) the electrons are degenerate, and we will show in this chapter that an important consequence of this is that diffusion depends on spin. While degeneracy had been implicitely included in some theoretical treaments of spin polarized electron transport (D'Amico and Vignale (2002); Takahashi et al. (2008); Qi et al. (2006)), it had not yet been explicitely detailed nor experimentally demonstrated.

Moreover, as discussed in Chapter 2, in p-doped material it is possible to control the degree of spin polarization of the ensemble of conduction electrons, so that the quasi-Fermi levels of spin + and spin − electrons can differ significantly, $E_{F_+} \neq E_{F_-}$, which is at the origin of a spin-dependence of the diffusion constant. We will show in the rest of this chapter that this is responsible for a novel spin filter effect which is of interest because it should modify all the other observed spin transport phenomena discussed in Chapter 2

in the degenerate regime, and it may affect the operation of a large number of proposed semiconductor spintronic devices (Datta and Das (1990); Wunderlich (2010); Zutic et al. (2007); Gerhardt et al. (2011))

We describe the relative efficiencies of the various possible charge-spin coupling mechanisms involved when bulk, $p^+$ material is considered. The ambipolar coupling to the photo-created hole distribution is of central importance, since, as it will be shown in Chapter 6, it increases the electron density near the excitation spot, favouring degeneracy. Also, Coulomb spin drag and spin-dependent bandgap renormalization effects will be shown to be negligible in this sample because of electrostatic screening by the majority holes.

## 5.1 General form of the diffusion equations

We suppose that there exists a radially symmetric excitation profile $g$ on an homogeneous sample (as in sec.3.2). In the absence of Rashba effects, i.e, in a bulk sample, the charge ($n$) and spin ($s$) densities will inherit this symmetry and both will be functions of $r$ and $z$, where $z$ is the depth coordinate inside the semiconductor. These two densities are, respectively, solutions of the continuity equations already given in Chapter 2

$$[g_+(r,z) + g_-(r,z)] - n(r,z)/\tau + \frac{1}{q}\vec{\nabla}\cdot[\vec{J_c}(r,z)] = 0 \tag{5.1}$$

$$[g_+(r,z) - g_-(r,z)] - s(r,z)/\tau_s + \frac{1}{q}\vec{\nabla}\cdot[\vec{J_s}(r,z)] = 0 \tag{5.2}$$

Here, $g_\pm$ is the spatially-dependent rate of creation of electrons of spin $\pm$, and $1/\tau_s = 1/\tau + 1/T_1$. Equations (5.1) and (5.2) are accompanied by the following boundary conditions: i) The normal component of the electron current at the front ($z = 0$) and back surface ($z = d$) is equal to $qSn(0)$ and $-qS'n(d)$ respectively. Here $S$ and $S'$ are the corresponding recombination velocities. ii) The normal component of the spin current equals $qSs(0)$ and $-qS's(d)$, respectively.

In the next sections it will be shown that the charge and spin currents $\vec{J_c} = \vec{J_+} + \vec{J_-}$ and $\vec{J_s} = \vec{J_+} - \vec{J_-}$ are expressed as the sum of three contributions; drift currents due to

internal or external electric field, diffusive currents in response to a spatial gradient of the Fermi energy, and thermoelectric currents caused by a gradient of the electronic temperature, where each of these contributions is the sum and difference of the corresponding spin currents, respectively: $\vec{J}_{c(s)} = [\vec{J}_+^{\rm drift} \pm \vec{J}_-^{\rm drift}] + [\vec{J}_+^{\rm diff} \pm \vec{J}_-^{\rm diff}] + [\vec{J}_+^{\rm therm} \pm \vec{J}_-^{\rm therm}]$.

A simple way to calculate the charge and spin currents $\vec{J}_c(r,z)$ and $\vec{J}_s(r,z)$ is to write the steady-state equation of motion for the spin $i$ electrons. In the presence of an electric field $\vec{E}$, and of a gradient of the Fermi energy $E_{F_i}$, we have [D'Amico and Vignale (2002)]:

$$m^* \frac{d\vec{v}_i}{dt} = -q\vec{E} - \vec{\nabla} E_{Fi} - \frac{m^* \vec{v}_i}{\tau_{mi}} - \frac{m^*(\vec{v}_i - \vec{v}_{-i})}{\tau_{ee,i}} \tag{5.3}$$

where $\vec{v}_i$ is the average velocity of electrons with spin $i$, the first and second terms on the right represent the force due to the electric field or to a gradient of the Fermi energy, respectively, and the fourth term is a drag term which reflects the transfer of momentum between spin $i$ and spin $-i$ electrons. This term is naturally proportional to the difference $\vec{v}_i - \vec{v}_{-i}$ and to the inverse of the collision time between electrons of spin $i$ with electrons of opposite spin, $\tau_{ee,i}$. This time can be written in the form $\tau_{ee,i} n_{-i} = n\tau_{ee}$, where $\tau_{ee}^{-1}$ corresponds to the factor $\gamma$ of D'Amico and Vignale (2000). Here, $\tau_{mi}$ is related to the mobility $\mu_i$ of noninteracting electrons of spin $i$ by $\mu_i = q\tau_{mi}/m^*$.

For $i = +$ and $i = -$, the system of the two coupled Eqs.(5.3) has a steady state solution that can be written in the form:

$$\vec{J}_i = q n_i \vec{v}_i = \vec{E} \sum_j \sigma_{ij} + \frac{1}{q} \sum_j \sigma_{ij} \vec{\nabla}_r E_{Fj} \tag{5.4}$$

where the various contributions will be described in the following sections. A more rigorous calculation of the Boltzmann equation (Appendix 8.2) gives a current which is found to be similar to Eq.(5.4), with an additional term to correct for thermoelectric effects.

## 5.2 Drift currents

The first term in Eq.(5.4) is a drift current due to the electric field $\vec{E}$. It is given by a generalized Ohm's law $\vec{J}_i^{\rm drift} = \vec{E} \sum_j \sigma_{ij}$, where the nondiagonal elements of the conductivity

matrix $\sigma_{ij}$ reflect the coupling between opposite spins originating from electron-electron collisions (spin Coulomb drag). This matrix is given by:

$$\sigma = \frac{q}{\tau_{ee}+\tau_m}\begin{bmatrix} n_+\mu_+(\tau_{ee}+\frac{n_+}{n}\tau_{m,-}) & n_+\mu_+\frac{n_-}{n}\tau_{m,-} \\ n_-\mu_-\frac{n_+}{n}\tau_{m,+} & n_-\mu_-(\tau_{ee}+\frac{n_-}{n}\tau_{m,+}) \end{bmatrix} \tag{5.5}$$

where the spin-averaged time $\tau_m$ is defined as

$$\tau_m = (n_+/n)\tau_{m-} + (n_-/n)\tau_{m+} \tag{5.6}$$

One then has $\vec{J}_c^{\text{drift}} = \sigma_c\vec{E}$ and $\vec{J}_s^{\text{drift}} = \sigma_s\vec{E}$, where $\sigma_c = [\sigma_{++}+\sigma_{+-}+\sigma_{-+}+\sigma_{--}]$ and $\sigma_s = [\sigma_{++}+\sigma_{+-}-\sigma_{-+}-\sigma_{--}]$.

## 5.3 Diffusion currents

The diffusion current of spin $i$ electrons is obtained from the second term of Eq.(5.4) which involves the spatial gradient of the Fermi energy. Note that this gradient is given by $\vec{\nabla}_r E_{F_j} = \vec{\nabla}_r E_{F_j}\mid_{T_e} + (\partial E_{F_j}/\partial T_e)\vec{\nabla}_r T_e$. However, the second term contributes to the thermoelectric current and will be considered in the following subsection. The diffusion current is given therefore by

$$\vec{J}_i^{\text{diff}} = \sum_j \sigma_{ij}(\vec{\nabla}_r E_{F_j}\mid_{T_e}). \tag{5.7}$$

Since $\vec{\nabla}_r E_{F_i}\mid_{T_e} = \sum_j \frac{\partial E_{F_i}}{\partial n_j}\vec{\nabla}_r n_j$ , the spatial gradient at constant temperature can be expressed as $\vec{\nabla}_r E_{F_j}\mid_{T_e} = S_{jj}\vec{\nabla}_r n_j + S_{j,-j}\vec{\nabla}_r n_{-j}$ where the spin stiffness matrix is given by

$$S_{ij} = \frac{\partial E_{F_i}}{\partial n_j}. \tag{5.8}$$

Eq.(5.7) takes the form of a generalized Fick's law:

$$\vec{J}_i^{\text{diff}} = q(D_{ii}\vec{\nabla}n_i + D_{i,-i}\vec{\nabla}n_{-i}) \tag{5.9}$$

where the elements of the diffusion matrix $D$ are given by

$$q^2 D_{ij} = \sigma_{ii}S_{ij} + \sigma_{i,-i}S_{-i,j}. \tag{5.10}$$

In the non-degenerate case, and considering only the diagonal terms of the spin stiffness matrix, one has $S_{ii} = \partial E_{F_i}/\partial n_i = k_B T_e/n_i$, so that the diffusion constant for spin $i$ electrons reduces to Eq.(2.6), $D_{ii} = k_B T_e/q\mu_e$. Equation (5.10) is therefore the generalized Einstein relation. We see that the charge and spin diffusive currents are then coupled, as in Eq.(1.8):

$$\frac{1}{q}J_c^{\text{diff}} = \frac{1}{q}(\vec{J}_+^{\text{diff}} + \vec{J}_-^{\text{diff}}) = D_{cc}\vec{\nabla}n + D_{cs}\vec{\nabla}s$$

$$\frac{1}{q}J_s^{\text{diff}} = \frac{1}{q}(\vec{J}_+^{\text{diff}} - \vec{J}_-^{\text{diff}}) = D_{sc}\vec{\nabla}n + D_{ss}\vec{\nabla}s$$

where the elements of the diffusion matrix are linear combinations of the $D_{ij}$ given by $2D_{cc} = [D_{++} + D_{+-} + D_{-+} + D_{--}]$ and $2D_{ss} = [D_{++} - D_{+-} - D_{-+} + D_{--}]$, $2D_{cs} = [D_{++} - D_{+-} + D_{-+} - D_{--}]$ and $2D_{sc} = [D_{++} + D_{+-} - D_{-+} - D_{--}]$, and can be straightforwardly calculated if the spin stiffness matrix $S_{ij}$ is known.

We will show in the following section that degeneracy alone gives a symmetric coupling of the form $D_{cs} = D_{sc} \neq 0$. Of course, different mechanims may exist at the same time, giving a very complex set of coupled equations for charge and spin diffusion.

### 5.3.1 The effect of Pauli principle on diffusion currents

Degeneracy induces a spin dependence of the diffusion constant due to two distinct effects which are direct consequences of the Pauli Principle. Neglecting electron-electron interactions which will be shown in sec.5.5 to be screened by the hole gas, the spin stiffness matrix is diagonal, and so the conductivity matrix of Eq.(5.5). The spin stiffness is calculated using the relation between the Fermi level $E_{Fi}$ of spin $i$ electrons and the spin concentration $n_i$ is given by

$$n_i = N_c^s \mathscr{F}_{1/2}^*(\eta_i) \tag{5.11}$$

where $\eta_i = E_{Fi}/k_B T_e$ and $N_c^s$ is the spin-resolved effective density of states in the conduction band, whose temperature dependence in GaAs is given by:

$$N_c^s = 2.15 \times 10^{17} \left(\frac{T_e}{300}\right)^{3/2} \text{ cm}^{-3} \tag{5.12}$$

and where the Fermi integral $\mathscr{F}_k^*(\eta_i)$ is given by

$$\mathscr{F}_k^*(\eta_i) = \frac{1}{\Gamma(k+1)} \int_0^\infty \frac{x^k dx}{1+e^{x-\eta_i}} \tag{5.13}$$

taking the derivative of Eq.(5.11) with respect to $n_i$ gives:

$$S_{ii} = \frac{\partial E_{Fi}}{\partial n_i} = \frac{k_B T_e}{N_c^s \mathscr{F}_{-1/2}^*(\eta_i)} \tag{5.14}$$

so that $S_{ii}$ decreases with increasing concentration. Eq. (5.10) then reduces to the spin-uncoupled Einstein equation for a degenerate electron gas [Finkelshtein (1983)]

$$D_i = \frac{n_i \mu_i}{q} S_{ii} \tag{5.15}$$

which can be reformulated as:

$$\boxed{D_i = \xi(n_i)\mu_i \frac{k_B T_e}{q}} \tag{5.16}$$

where the reduced spin stiffness $\xi = n_i S_{ii}/k_B T_e$ is found using Eq. (5.11) and given by

$$\xi(n_i) = \frac{\mathscr{F}_{1/2}^*(\eta_i)}{\mathscr{F}_{-1/2}^*(\eta_i)} \tag{5.17}$$

This quantity is unity for a nondegenerate gas and increases with concentration. The bottom panel of Fig.5.1 shows the concentration dependence of $\xi$ for $T_e = 50$ K, for which the density of states, according to Eq.(5.12), is $N_c^s \approx 1.5 \times 10^{16}$ cm$^{-3}$. It is seen that $\xi(n_i)$ becomes larger than 1 in the degenerate regime, i.e, when the spin photoelectron concentration $n_i$ approaches $N_c^s$.

The second possible effect induced by degeneracy is a spin-dependent increase of the mobility of spin $i$ electrons, as described by

$$\mu_i = q\tau_{mi}/m^* \tag{5.18}$$

because the Pauli principle directly affects the averaged momentum relaxation time $\tau_{mi}$, calculated in Appendix 8.2 using the Boltzmann equation formalism. It is found equal to:

$$\tau_{mi} = -\frac{2}{3}\frac{\int_0^\infty \tau_m(\varepsilon)\varepsilon^{3/2}(\partial f_{0i}/\partial\varepsilon)d\varepsilon}{\int_0^\infty \varepsilon^{1/2} f_{0i} d\varepsilon} \tag{5.19}$$

where $f_{0i}$ is the Fermi distribution and $\varepsilon$ is the kinetic energy in the conduction band. Here, $\tau_m(\varepsilon)$ is assumed to be of the form ((Smith (1978); Qi et al. (2006)):

$$\tau_m(\varepsilon) = a(T_L, T_e)\varepsilon^p \tag{5.20}$$

where the coefficients $a$ and $p$ determine the temperature dependence of the mobility, which was studied in Chapter 4. The concentration dependence of $\mu_i$ is obtained using Eq.(5.18), (5.19) and (5.20). One finds:

$$\boxed{\mu_i = \mu_0 \frac{\mathscr{F}^*_{p+1/2}(\eta_i)}{\mathscr{F}^*_{1/2}(\eta_i)} = \mu_0 \zeta(n_i)} \tag{5.21}$$

where $\mu_0$ is the mobility in nondegenerate conditions. Eq. (5.21) is a direct consequence of Pauli exclusion due to which elementary scattering processes are forbidden if the final state is already occupied by an electron of the same spin. As seen in the bottom panel of Fig.5.1, the quantity $\zeta$ increases with concentration. This increase is similar to that of $\xi$ for $p = 3/2$ and becomes progressively weaker with decreasing $p$.

The diffusion constant for spin $i$ electrons is finally given by

$$D_i = D_0 \nu(n_i) \tag{5.22}$$

where $D_0 = \mu_0 k_B T_e/q$ is the diffusion constant in a non-degenerate regime, and where

$$\boxed{\nu(n_i) = \xi(n_i)\zeta(n_i) = \frac{\mathscr{F}^*_{p+1/2}(\eta_i)}{\mathscr{F}^*_{-1/2}(\eta_i)}}. \tag{5.23}$$

The top panel of Fig.5.1 shows the function $\nu(n_i)$ as a function of the photoelectron concentration $n_i$. Also shown is the position of the Fermi energy with respect to the bottom of the conduction band. Different values for $p$, as defined in Eq.(5.20), are considered. It can be read off from Fig.5.1 that, for a typical electron gas of density $n = 10^{17}$ cm$^{-3}$ and

### 5.3. Diffusion currents

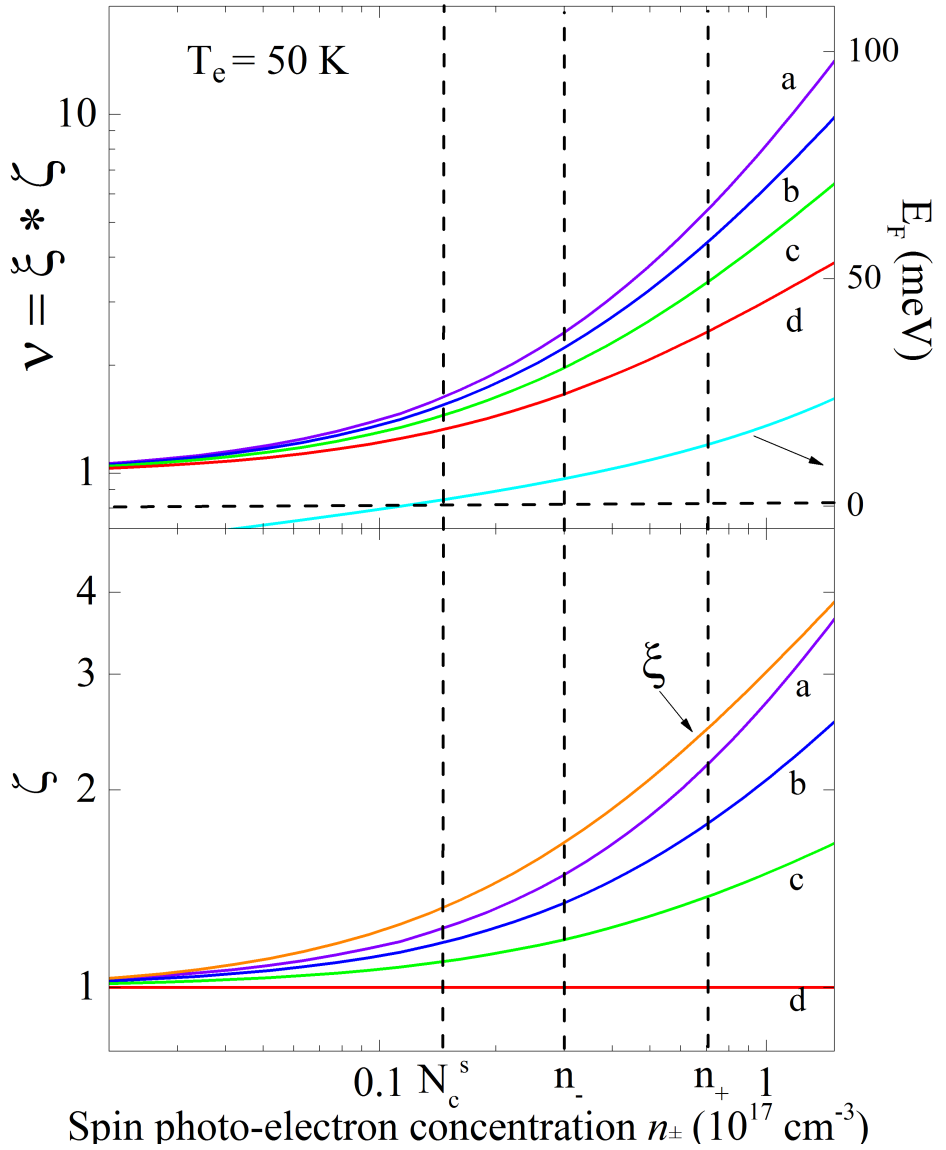


**Figure 5.1:** At $T_e = 50$ K, the bottom panel shows the reduced mobility $\zeta(n_\pm)$ as a function of photoelectron concentration $n_\pm$, defined in Eq.(5.21), for selected values of $p$, as defined by Eq. (5.20) : 3/2 (a),1 (b), 1/2 (c), 0 (d). Also shown is the function $\xi(n_\pm)$. The top panel shows the reduced diffusion constant $\nu(n_\pm)$ for the same values of $p$ as before, as well as the Fermi energy $E_{F_i}$, as a function of spin photolectron concentration. It is seen that degeneracy is important when $E_{F_i} geq 0$, and therefore, when $n_\pm \geq N_c^s \approx 1.5 \times 10^{16}$ cm$^-3$, where $N_c^s$ is the spin-resolved density of states. The vertical dashed lines represents the positions of $N_c^s$, $n_+$ and $n_-$ for a gaz of density $n = 10^{17}$ cm$^{-3}$ and spin polarization of $\mathscr{P} = 0.4$.

polarization of $\mathscr{P} = 0.4$ such that $n_+ = 7 \times 10^{16}$ cm$^{-3}$ and $n_- = 3 \times 10^{16}$ cm$^{-3}$, the ratio between $D_+$ and $D_-$ can be as large as $D_+/D_- \approx 2.2$ for $p = 3/2$ (unscreened ionized impurity scattering) and gradually reduces to $D_+/D_- \approx 1.49$ for $p = 0$, in which case the mobility is independent of concentration (see Eq.(5.21)).

### 5.3. Diffusion currents

I will show now that the concentration dependence of the diffusion constant, as defined by Eq.(5.23), introduces a novel charge-spin coupling mechanism. For this, we first approximate Eq.(5.22) to first order in $\mathscr{P}$ as:

$$D_{\pm} = D^*[1 \pm \delta\mathscr{P}] \tag{5.24}$$

with $D^* = D_0\nu(n/2)$ and where

$$\delta = \frac{n/2}{\nu(n/2)}\frac{d\nu(n/2)}{dn} = d\log[\nu(n/2)]/d\log(n/2) \tag{5.25}$$

which is equal to $2(p+1)/3$ at large degeneracy. Using the linearized form defined by Eq.(5.24), the charge and spin diffusion constants which appear in Eq.(1.8) are given by :

$$D_{cc} = D_{ss} = D^* \tag{5.26}$$

$$D_{cs} = D_{sc} = D^*\delta\mathscr{P} \tag{5.27}$$

and the linearized diffusion equations become:

$$\begin{aligned} [g_+ + g_-] - n/\tau + \vec{\nabla}\cdot[D^*(\vec{\nabla}n + \delta\mathscr{P}\vec{\nabla}s)] &= 0 \\ [g_+ - g_-] - s/\tau_s + \vec{\nabla}\cdot[D^*(\vec{\nabla}s + \delta\mathscr{P}\vec{\nabla}n)] &= 0 \end{aligned} \tag{5.28}$$

The Pauli Principle induces therefore a coupling between the charge and spin diffusion currents, for which the coupling coefficients $\delta\mathscr{P}$ are identical in the two equations. They increase with electron polarization and concentration. Two interesting effects predicted by (5.28) are identified:

- A novel spin filter effect: since, for $p > -1$, $\nu(n_i)$ is an increasing function of $n_i$, diffusion of majority $n_+$ electrons is more efficient compared with diffusion of minority $n_-$ electrons, $D_+ > D_-$ and $L_+ > L_-$. This has an interesting consequence on spin-polarized transport: once spin polarized electrons are created at $r = 0$, there is a diffusion-induced spatial separation of $n_+$ and $n_-$. Remarkably, this spin filter effect does not require any interface (Rougemaille et al. (2008), Vu et al. (2011)), it happens in bulk, homogeneous material. This is illustrated in Fig.5.2, where we

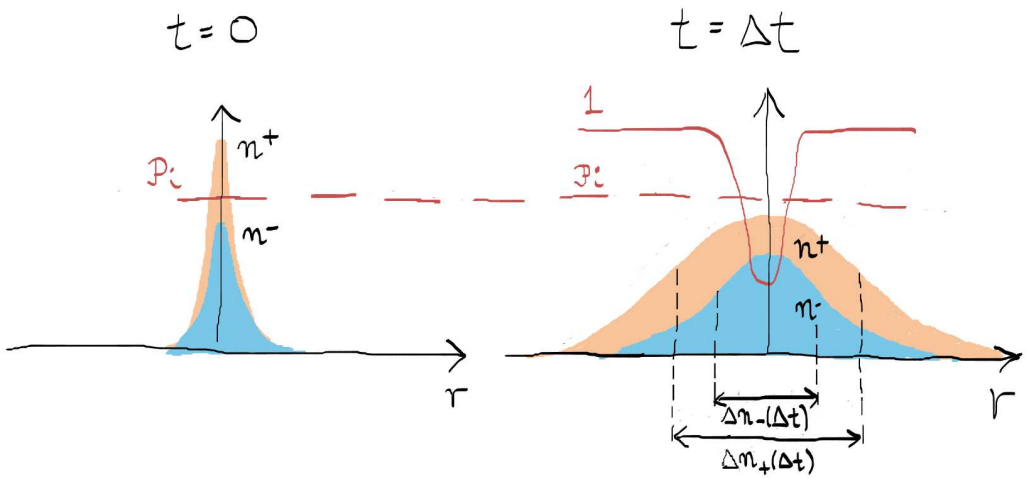


**Figure 5.2:** Principle of the Pauli principle driven spin filter effect: At $t = 0$, spin polarized electrons are injected in a semiconductor, with $s/n = \mathscr{P}_i$. After some time $\Delta t$, the density of $n_+$ is broader than the density of $n_-$ because of spin dependent diffusion. This produces a reduction of the spin polarization at $r = 0$, which becomes an increasing function of distance. Ignoring all spin relaxation mechanisms, the polarization will get close to 1 at distances much larger than $\Delta n_-$.

suppose that spin polarized electrons are created at $t = 0$ and are localized around $r = 0$, with an initial spin polarization $\mathscr{P}_i$. After a time $\Delta t$, and considering only the effect of diffusion, it is seen that since $D_+ > D_-$, the $n_+$ distribution spreads over a typical distance $\Delta n_+(\Delta t)$ which is larger than that for $n_-$, $\Delta n_-(\Delta t)$. Therefore, the spin polarization at $r = 0$ will be lower than $\mathscr{P}_i$, reaching its maximum possible value of 1 at distances where there are only spin + electrons.

- The other effect of the Pauli principle is that charge diffusion becomes spin-dependent. It is seen from the linearized charge diffusion equation appearing in (5.28) that, writing $s = n\mathscr{P}$ and neglecting the spatial variation of $\mathscr{P}$, one obtains a spin-averaged diffusion constant $\langle D \rangle = (n_+ D_+ + n_- D_-)/n$ equal to:

$$\langle D \rangle = D^*(1 + \delta \mathscr{P}^2) \tag{5.29}$$

For a fixed number of photoelectrons, the volume they occupy in space will be larger when they are spin polarized. This is physically equivalent to saying that the majority spins experience an additional outwards force due to the quantum degeneracy pressure. It is possible to directly observe this phenomenon by modulating the photoexcitation polarization between a $\sigma$ circularly polarized state and a linear po-

larized state $\pi$ without changing the excitation power (This is the $\sigma - \pi$ experiment, discussed in 6.2).

## 5.4 Thermoelectric currents : Soret charge and spin currents

In this section we consider the situation in which the electronic temperature varies in space. As discussed in 5.3, the spatial gradient of the Fermi energy will have a contribution coming from the spatial variation of $T_e$, leading to thermoelectric currents. The thermoelectric current of electrons of spin $i$ is calculated in Appendix 8.2 by solving the Boltzmann equation. It is of the form $\vec{J}_i^T = -\sum_j \sigma_{ij}\mathscr{S}_j\vec{\nabla}_r T_e$ and $\mathscr{S}_j$ is the spin-dependent Seebeck coefficient for which the value for unpolarized electrons is equal to its usual value given elsewhere (Cutler and Mott (1969)). It is given by $\mathscr{S}_j = -(1/qT_e)(E_{Tj} - \gamma_j k_B T_e)$, with

$$E_{Ti} = \frac{\int \tau_m(\varepsilon)\varepsilon^{3/2}(\partial f_{0i}/\partial\varepsilon)d\varepsilon}{\int \tau_m(\varepsilon)\varepsilon^{1/2}(\partial f_{0i}/\partial\varepsilon)d\varepsilon} \tag{5.30}$$

where $\gamma_i$ depends on the Fermi integral $\mathscr{F}_k(\eta) = \Gamma(k+1)\mathscr{F}_k^*(\eta)$ and is given by

$$\gamma_i = \frac{\mathscr{F}_{1/2}(\eta_i)}{\mathscr{F}_{-1/2}(\eta_i)} \tag{5.31}$$

Note that $\gamma_i = \xi(n_i)/2$, where $\xi$ is given by Eq.(5.17), so that one has $\mathscr{S}_i = -[k_B/q]\xi\theta_i$, with $\theta_i$ a dimensionless quantity given by

$$\theta_i = \frac{E_{T_i}}{\xi k_B T_e} - 1/2 \tag{5.32}$$

Its concentration dependence is shown in Fig. 5.3 for selected values of $p$.

In agreement with this curve, it can be shown that this quantity decreases with increasing concentration from $p+1$ in the nondegenerate limit to unity at very large $n$. In the case where $p = 0$, $\theta_i = 1$, independent of $n_i$. In spite of the resemblance of the above equations to those describing the Seebeck effect, the spin currents arise through a distinct effect, since the Seebeck effect describes a case in which there is generally no current [Brechet and Ansermet (2010)]. This effect has been described by Soret (1879) for mass

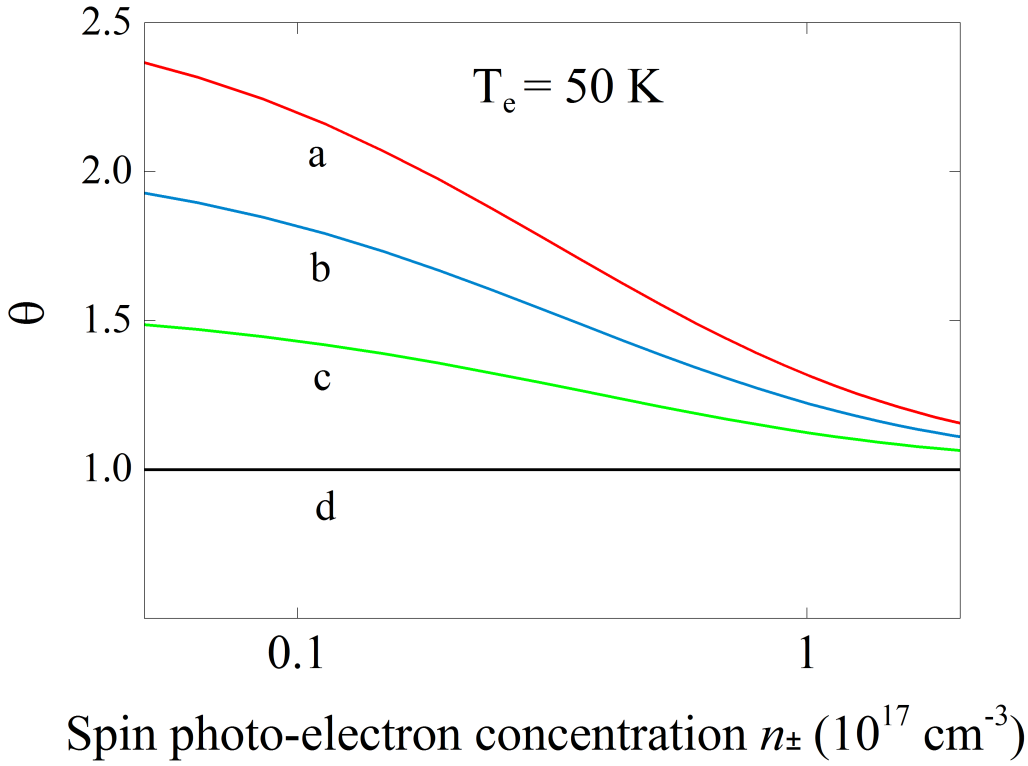


**Figure 5.3:** The dimensionless quantity $\theta$ [Eq. (5.32)] on which depends the Soret current, for $p = 3/2$ (a), 1 (b), 1/2 (c), 0 (d).

transport and the current $\vec{J}_i^T$ will be hereafter called the Soret current. Here, it is more convenient to express it in the form

$$\vec{J}_i^T = q \sum_j \vec{K}_{ij} n_j \tag{5.33}$$

The Soret velocity matrix $\vec{K}_{ij}$ is given by

$$q\vec{K}_{ij} = \frac{\sigma_{ij}}{q n_i \mu_i} \mu_j \left( \frac{E_{Tj}}{k_B T_e} - \gamma_j \right) \vec{\nabla}_r (k_B T_e) = \frac{\sigma_{ij}}{q n_i \mu_i} \mu_j \xi_j \theta_j \vec{\nabla}_r (k_B T_e) \tag{5.34}$$

so that, for a diagonal spin stifness matrix

$$\vec{K}_{ii} = D_{ii} \frac{\vec{\nabla}_r (k_B T_e)}{k_B T_e} \theta_i \tag{5.35}$$

The currents $\vec{J}_{cT}$ and $\vec{J}_{sT}$ are finally written

$$\vec{J}_c^T = q[\vec{K}_{cc}n + \vec{K}_{cs}s] \tag{5.36}$$

$$\vec{J}_s^T = q[\vec{K}_{sc}n + \vec{K}_{ss}s] \tag{5.37}$$

where $2\vec{K}_{cc} = [\vec{K}_{++} + \vec{K}_{+-} + \vec{K}_{-+} + \vec{K}_{--}]$, $2\vec{K}_{ss} = [\vec{K}_{++} - \vec{K}_{+-} - \vec{K}_{-+} + \vec{K}_{--}]$, $2\vec{K}_{sc} = [\vec{K}_{++} + \vec{K}_{+-} - \vec{K}_{-+} - \vec{K}_{--}]$, and $2\vec{K}_{cs} = [\vec{K}_{++} - \vec{K}_{+-} + \vec{K}_{-+} - \vec{K}_{--}]$.

As found from Eq. (5.35),

$$\frac{K_{++}}{K_{--}} = \frac{\theta(n_+)}{\theta(n_-)}\frac{D_+}{D_-} \tag{5.38}$$

so that under degeneracy the Soret current becomes spin-dependent. This creates a spin filter effect in the same way as spin-dependent diffusion. However, as shown in Fig. 5.3, $\theta(n_+) < \theta(n_-)$, so that the ratio of spin Soret velocities is smaller than that of the spin diffusion constants. In this case, the spin dependence of $J_c^T + J_c^{\text{diff}}$ is smaller than that of the sole $J_c^{\text{diff}}$, so that the thermal gradient causes an effective decrease of the spin filter effect.

Under the sole effect of the thermal gradient, the Soret velocities are given by $K_{cc} = K_{ss} = [K_{++} + K_{--}]/2$ and $K_{cs} = K_{sc} = [K_{++} - K_{--}]/2$ while $K_{+-} = K_{-+} = 0$. The ratio of the unipolar diffusive $[J_c^{\text{diff}}]$ and Soret currents is then given by

$$\frac{J_c^T}{J_c^{\text{diff}}} = \theta\frac{\vec{\nabla}_r T_e/T_e}{\vec{\nabla}_r n/n} \tag{5.39}$$

Since $\theta$ is in general of the order of unity, the ratio of the Soret current to the usual diffusion current is mainly determined by the relative values of the temperature and charge gradients.

## 5.5 Hole screening of electron-electron interactions

It is shown here that spin-spin or spin-charge couplings induced by electron-electron interactions are strongly suppressed because of screening by the hole gas. The effect of hole screening can be simply taken into account in the Random Phase Approximation (RPA)

in the present case where the hole concentration is larger than the electronic concentration, so that the hole screening is dominant over the electronic one. In this case, the static Coulomb potential in Fourier space is given by (Mahan (1981),Collet (1993))

$$v(k) = \frac{4\pi e^2}{\epsilon(k^2 + k_{DH}^2)} \tag{5.40}$$

where $e = q/\sqrt{4\pi\epsilon_0}$. The Debye Hückel screening wavevector $k_{DH}$ depends on the hole concentration according to Collet and Amand (1986)

$$k_{DH}^2 = \frac{4\pi e^2 N_A^-}{\epsilon k_B T} \frac{1}{\xi(N_A^- + \delta p)} \tag{5.41}$$

where $\delta p$ is the photo-hole concentration and the function $\xi$ is the same as in Eq.(5.17) but its argument is here the total hole concentration. In this framework, it seems clear that electron-electron interactions will be suppressed if $k_{DH}$ is larger than the typical value of $k$, of the order of the Fermi wavevector $k_{Fi} = (6\pi^2 n_i)^{1/3}$. In our sample, $N_A^- = 10^{18}$ cm$^{-3}$, so that with a hole temperature of $T_h = 50$ K one has $k_{DH} = 1.91 \times 10^7$ cm$^{-1}$. Considering an electronic concentration as high as $n = 10^{17}$ cm$^{-3}$, $k_F = 1.43 \times 10^6$ cm$^{-1}$, which is an order of magnitude smaller than $k_{DH}$. The photoelectron concentration required to have $k_F \sim k_{DH}$ is of the order of $n \sim 10^{20}$ cm$^{-3}$. A more detailed calculation (Cadiz et al. (2015a)) shows that due to this screening of the electron-electron interactions, exchange interactions and spin drag can be neglected.

## 5.6 Ambipolar diffusion equations

Taking account of all contributions defined in the preceding section, the diffusion equations for electrons and spins can be written

$$(g_+ + g_-) - n/\tau + \vec{\nabla} \cdot [(\vec{E}/q)\sigma_c + D_{cc}\vec{\nabla}n + D_{cs}\vec{\nabla}s + \vec{J}_c^T] = 0 \tag{5.42}$$

$$(g_+ - g_-) - s/\tau_s + \vec{\nabla} \cdot [(\vec{E}/q)\sigma_s + D_{sc}\vec{\nabla}n + D_{ss}\vec{\nabla}s + \vec{J}_s^T] = 0 \tag{5.43}$$

Since the hole effective mass is much larger than that of the electron, one has $D_h \ll D_e$, where $D_h$ is the majority hole diffusion constant. As a consequence, after creation

by light, both densities will spread at different rates. This charge separation leads to the appereance of an electric field that opposes to the separation of charges, affecting thus electron diffusion. In order to take into account the electrostatic coupling between electrons and the slower diffusing holes, it is further necessary to couple these equations with the diffusion equation for spin-unpolarized holes, which is

$$(g_+ + g_-) - \delta p/\tau + \vec{\nabla} \cdot [-(\vec{E}/q)\sigma_h + D_h \vec{\nabla}\delta p] = 0 \tag{5.44}$$

where $\delta p$ is the photohole concentration and $D_h$ is the hole diffusion constant.Here $\sigma_h = q(N_A^- + \delta p)\mu_h$ is the hole conductivity, where $\mu_h$ is the hole mobility. The thermoelectric hole current is neglected since the local heating of the hole gas is weak (Leo and Collet (1991)). The electric field satisfies Poisson's equation

$$\vec{\nabla} \cdot \vec{E} = e(\delta p - n)/\epsilon \tag{5.45}$$

where $\epsilon$ is the permittivity. Equations (5.42), (5.43), (5.44) and (5.45) must be solved numerically, as shown in Appendix 8.1.5, by imposing that, in addition to the boundary conditions for $n$ and $s$ defined in sec.5.1, the normal component of the hole current at the front ($z = 0$) and back surface ($z = d$) is equal to $qS\delta p(0)$ and $-qS'\delta p(d)$, respectively.

## 5.7 Conclusion of this chapter

We present a theoretical investigation of the effect of degeneracy on spin transport of a photoelectron gas. We now recall the main results :

a) In conditions where the photoelectron gas is degenerate, i.e. for a sufficiently low temperature and large excitation power, a novel spin-charge coupling mechanism is predicted that dictates that diffusive transport depends on spin. Even in the case where the momentum relaxation time does not depend on concentration ($p = 0$), which is close to the experimental situation of sec.4.2.5, relative differences in the spin-resolved diffusion constants as large as 50% between the two types of spins are expected when $n = 10^{17}$ cm$^{-3}$ at $T_e = 50$ K. This creates a spin filter effect during diffusive transport so that, in strong contrast with the usual decrease of polarization caused by spin relaxation, one should observe

an effective increase of polarization with distance as long as the electrons are degenerate. The spin-averaged charge diffusion constant is also shown to be spin-dependent, since in degenerate conditions, the charge spatial profile depends on the average spin polarization of the photoelectrons, in analogy to the quantum pressure observed in atomic systems. This effect can be measured by changing the laser polarisation from circular ($\sigma$) to linear ($\pi$).

b) Two other effects are expected to affect the magnitude of the degeneracy-induced spin-dependent diffusion. Firstly, ambipolar diffusion should increase the confinement of photoelectrons at the center, and thus the amount of degeneracy, due to the electrostatic electron-hole coupling. Secondly, if the electronic temperature is spatially inhomogeneous, thermoelectric currents due to the spin Soret effect are predicted to depend on spin in degenerate conditions.

c) Other spin-spin or spin-charge coupling mechanisms such as spin drag or bandgap renormalization are negligible in the present case because of screening of the electron-electron interactions by the holes of our $p^+$ material.

Note that the experimental technique discussed in Chapter 3 seems better adapted than the transient spin-grating technique for investigating the effect of degeneracy on spin transport. The main reason is that effects of degeneracy on pure spin currents created in the latter technique are not amplified by ambipolar diffusion and decrease under increase of excitation power because of the unavoidable initial heating of the electron gas by ultrashort pulses. Moreover, the transient grating may decay faster than the time required for photoelectrons to cool down and reach a degenerate regime.

# Chapter 6

# Observation of a new spin filter effect

In this chapter I present experimental evidence that, as predicted in the preceding chapter, the quantum degeneracy pressure induced by the Pauli principle has at least two major consequences for spin-polarized transport in semiconductors. The first is the appearance of a spin-filter effect in which the spin-polarization of quantum degenerate electrons increases with the distance over which they are transported. This observation is not only in complete opposition to usual notions of spin relaxation and diffusion (Appelbaum et al. (2007); Kikkawa and Awschalom (1999); Favorskiy et al. (2010)), but cannot be described by any of the other novel, spin transport phenomena that have recently been reported (Weber et al. (2005); Koralek et al. (2009)). Secondly, a spin-charge coupling that causes an increase in the volume of the photo-electron population at high electronic polarizations. This increase in volume is equivalent to that observed in degenerate atom traps (Truscott et al. (2001)).

The effect of Pauli blockade on the characteristic lifetimes in semiconductors has been already explored. For example, Kalevich et al. (2001) showed a redistribution of spins states in quantum dots, but in such a confined system there is no transport involved. Nemec et al. (2005) studied spin-dependent phase-space filling and its consequences on the optical transmission in bulk GaAs, whereas Amo et al. (2007) observed Pauli blockade of the spin flip relaxation time, also in bulk GaAs. Again, these studies did not explore the consequences of Pauli blockade on spin transport. This is the first experimental report that deals explicitly with diffusion of spin-polarized electrons in the Pauli blockade regime.

## 6.1 Pauli blockade-driven Spin Filter Effect

Figure 6.1 illustrates the experimental observation of the spin filter effect. It shows 15 $\mu$m $\times$ 15 $\mu$m images of the steady state spin polarization $\mathscr{P} = s/n$, on the same sample studied in Chapter 4 at $T_L = 15$ K as a function of space and power density. It is assumed a priori that, after the initial excitation, the majority and minority spin populations thermalize to quasi-equilibria associated with two quasi-Fermi energies, $E_{F_\pm}$, with $E_{F_+} > E_{F_-}$. At low excitation power (top images in Fig.6.1), both quasi-Fermi levels fall in the bandgap of the semiconductor and the concentrations $n_+$ and $n_-$ are both smaller than the spin-resolved effective density of states in the conduction band $N_c^s$. In this limit and in the absence of Coulomb spin drag (Weber et al., 2005), as demonstrated in sec.5.5, the diffusion constant for both spin populations is given by the Einstein relation [Eq.(2.6)]. The spin polarization is maximum at the point of light excitation, and decreases monotically as a function of distance $r$ to the excitation spot. This corresponds to a normal diffusion process, in which electrons lose their spin polarization over time and thus during transport.

In the extreme opposite case, both $E_{F_+}$ and $E_{F_-}$ lie above the bottom of the conduction band and $n_+$ and $n_-$ are larger than $N_c/2$. In this degenerate limit, the Pauli Principle dictates a spin-dependence of the diffusion constant as discussed in Chapter 5 and shown in Fig.5.1. Thus, since $n_+ > n_-$, $D_+ > D_-$ and majority spin electrons diffuse further than minority spin electrons. Consequently there is an effective depletion of majority carriers in the central region of the bottom images in Fig. 6.1, bringing $n_+$ closer to $n_-$ and thereby reducing the spin polarization relative to its value at low excitation powers. Therefore, a local minimum of the spin polarization is expected near $r = 0$, as predicted in Fig.5.2.

This minimum indeed progressively appears, so that as shown in Fig.6.2, a volcano-like shape is observed at high power. It can be seen from these angular averaged profiles that at high photoelectron density, spin polarization actually increases during transport during the first 2 $\mu$m. The polarization at $r = 0$ $\mu m$ is 28 %, while at $r \approx 2$ $\mu m$, it is 42 %, slightly larger than its low power value at the same distance from the excitation spot. As $r$ further increases, both $n_+$ and $n_-$ are reduced via carrier recombination until they are

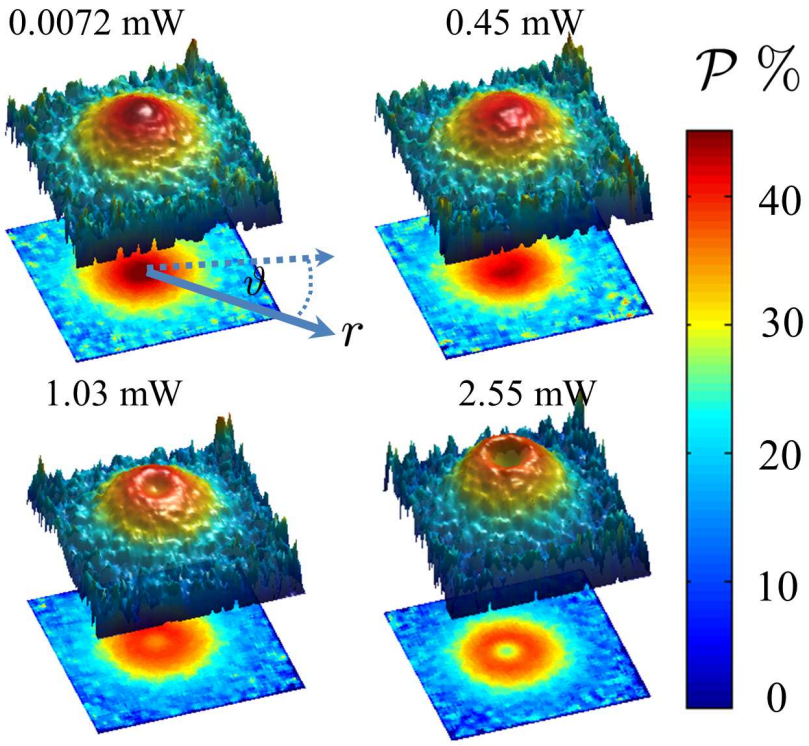


**Figure 6.1:** Images of the spin polarization, defined as the ratio between the spin density and the total electronic concentration, $\mathscr{P} = s/n$, in a GaAs thin film at $T_L = 15$ K induced by a circularly polarized, tightly focused laser spot at $r = 0$. As the excitation power and thus the photoelectron concentration increases, the appearance of a polarization dip at $r = 0$ is observed; i.e., the polarization increases during outwards diffusion. Luminescence spectra indicate an electronic temperature, $T_e = 50$ K, near $r = 0$.

smaller than $N_c/2$. In this case neither spin population is degenerate and spin transport is again described by the usual, decoupled diffusion process.

### 6.1.1 Size of the effect and level of degeneracy

The low power curves in Fig.6.2 reveal the expected polarization decrease caused by spin relaxation during transport (Favorskiy et al. (2010)). Note that at the lowest power, the steady-state electronic polarization at $r = 0$, $\mathscr{P}^{lp}(0) = 45$ % is almost equal to the initial polarization induced by light $\mathscr{P}_i = 50$ %. Since the spin relaxation time of thermalized electrons is much larger than their lifetime at this temperature (see Table 4.5), the slight difference comes mainly from spin relaxation during diffusion along $z$. In a simple two-dimensional picture, where the concentrations $n_\pm$ are replaced by their averages $\langle n_\pm \rangle$ over

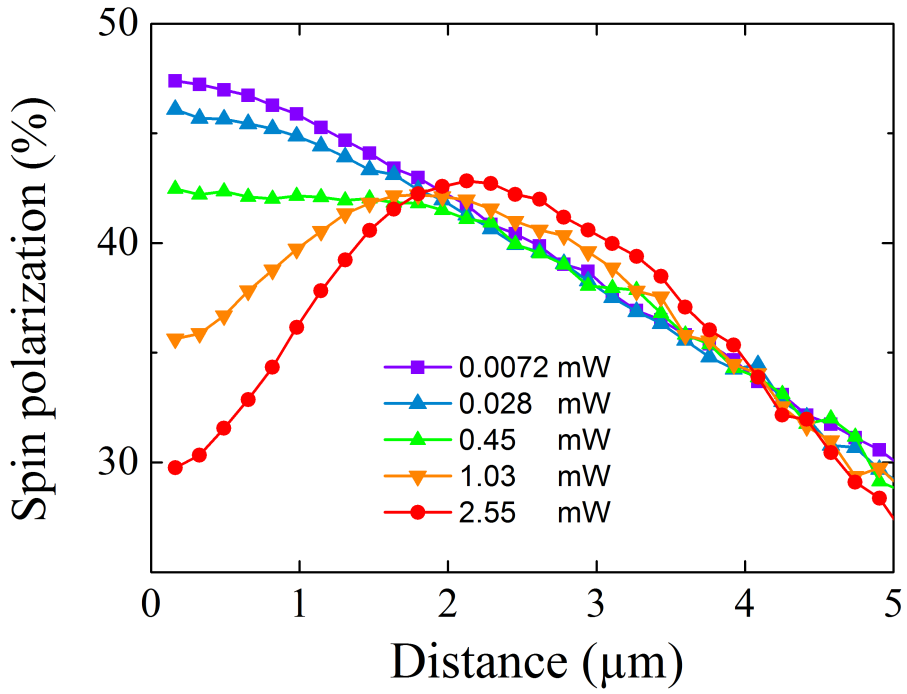


**Figure 6.2:** Angular averaged profiles of the spin polarization as a function of space and excitation power, 0.0072,0.028,0.45, 1.03 and 2.55 mW. The sample is kept at $T_L = 15K$ and the electronic temperature is $T_e = 50$ K.

depth $z$, this can be accounted for if $g_+$ and $g_-$ are replaced by $g_+^*$ and $g_-^*$, respectively, such that $g_+^*(0)/g_-^*(0) = (1 + \mathscr{P}^{lp}(0))/(1 - \mathscr{P}^{lp}(0))$.

In this framework, a semi-quantitative analysis of the experimental results is now performed by considering that the diffusion time necessary for the electrons to leave the excitation spot is, within numerical factors of order unity, given by

$$\tau_{eff}^0(\langle n_\pm \rangle) \approx \omega^2/[4D_\pm(\langle n_\pm \rangle)] \tag{6.1}$$

and is of the order of several ps, that is, shorter than characteristic times for recombination and spin relaxation. Considering that diffusion is the dominant process for removal of electrons from the excitation spot, the spin concentrations at $r = 0$ are given by:

$$\langle n_\pm \rangle = g_\pm^*(0)\tau_{eff}^0(\langle n_\pm \rangle) \tag{6.2}$$

One then obtains the following very simple results, in which the poorly known numerical

factors of the Eq.(6.1) are eliminated

$$D_+/D_- = \frac{1+\mathscr{P}^{lp}(0)}{1-\mathscr{P}^{lp}(0)} \times \frac{1-\mathscr{P}(0)}{1+\mathscr{P}(0)}. \tag{6.3}$$

From Eq.(6.3), at high power $D_+/D_- \approx 1.49$, implying that degeneracy causes a significant spin-dependence of the diffusion constant. By writing the diffusion constant in its linearized form of Eq.(5.27), one finds $\delta = 0.65$.

### 6.1.2 Polarization profiles as a function of excitation light polarization

In order to investigate the dependence of the effect of Pauli blockade on electronic spin polarization, we have changed the helicity of the excitation light in order to change $\mathscr{P}_i$. The corresponding polarization profiles, shown in panel a) of Fig. 6.3, show that the dip at the center indeed decreases with decreasing $\mathscr{P}_i$. Furthermore, as shown in Fig. 6.3 b), the electronic polarization at the point $r = 0$ is proportional to $\mathscr{P}_i$. This behavior is in agreement with the predictions made using Eq.(6.3) and Eq.(5.24), from which the following quadratic equation is obtained:

$$\delta\mathscr{P}^2(0) - (\delta+1)\mathscr{P}(0) + \mathscr{P}^{lp}(0) = 0. \tag{6.4}$$

To first order in $\mathscr{P}$, one has $\mathscr{P}(0) = \mathscr{P}^{lp}(0)/(1+\delta)$. From the slope of this behavior, one finds $\delta = 0.45$, in qualitative agreement with the value of the preceding subsection. The difference with the preceding value of $\delta = 0.65$ may be due to the fact that the electrons were at a higher temperature during these measurements, which is consistent with the fact that the averaged spin polarization in Fig.6.3 is smaller than the one observed in Fig.6.2, even at low excitation power.

Also shown in Fig.6.3 c) is the electronic polarization normalized by its maximum value, as a function of $\mathscr{P}_i$. It is seen that the relative magnitude of the polarization dip is independent of $\mathscr{P}_i$.

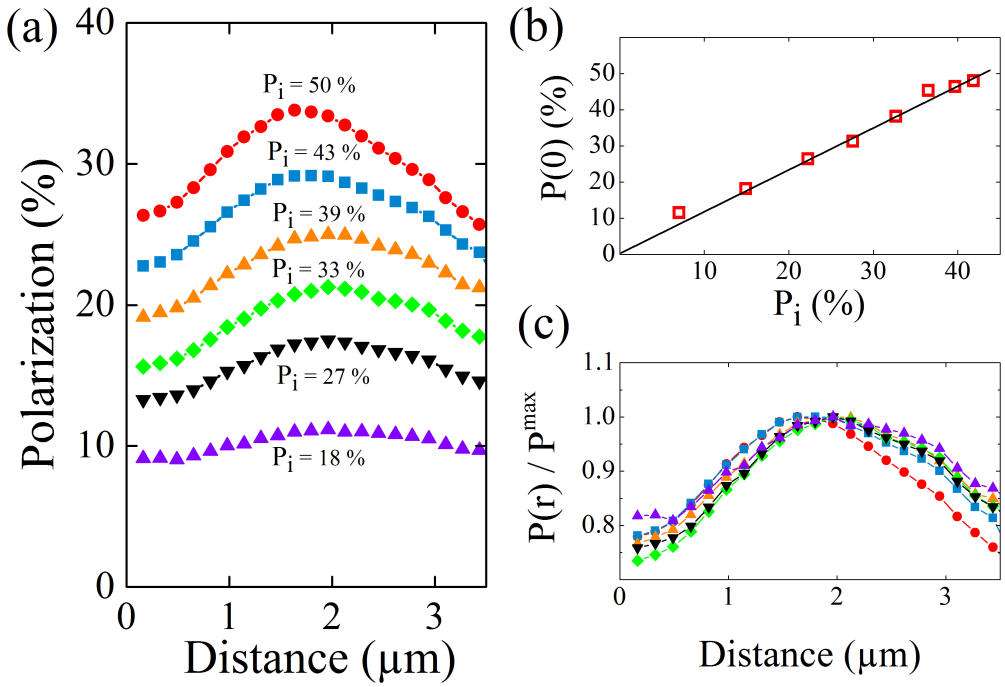


**Figure 6.3:** a) Electronic profiles for decreasing values of the initial polarization $|\mathscr{P}_i|$. As shown in panel b), the electronic polarization at $r = 0$ is proportional to $\mathscr{P}_i$, thus revealing that the ratio $D_+/D_-$ depends linearly on electronic polarization. Panel c) shows the same curves as panel a) when normalized by the maximum value of the spin polarization.

## 6.2 Spin-dependent charge diffusion: the $\sigma - \pi$ experiment

The effective charge diffusion constant, defined as $\langle D \rangle = (1/n) \sum_i n_i D_i$, is found using Eq. (5.29) and given by

$$\langle D \rangle = D^*[1 + \delta \mathscr{P}^2],$$

which implies that the charge profile under degeneracy depends on spin via a second order effect. This relative increase in the majority spin diffusion constant in the Pauli blockade regime is physically equivalent to saying that the majority spins experience an additional outwards force due to quantum degeneracy pressure, that changes the volume of the spin-polarized electron gas in the Pauli blockade regime in analogy with observations in atomic systems (Truscott et al. (2001)).

In order to demonstrate this effect, the sum profiles $I_\sigma$ for a circularly-polarized ($\sigma$) ex-

citation were compared with the profiles $I_\pi$ for a linearly-polarized excitation, ($\pi$, no electronic spin polarization), keeping the excitation power constant to within 0.1%. Figure 6.4 shows the relative difference of these profiles at $T_L = 15\ K$ for different power densities. At low power (Curve d), the signal is zero within experimental uncertainty, showing that charge transport in nondegenerate conditions does not depend on spin. In contrast, when the excitation power is increased, there progressively appears a depletion of photoelectrons at the center. This depletion, of the order of 2.5 %, is compensated by an excess of photoelectrons at a distance larger than about 1.5 $\mu$m, and shows that the diffusion constant of spin-polarized electrons is larger than for spin-unpolarized electrons created by $\pi$ excitation.

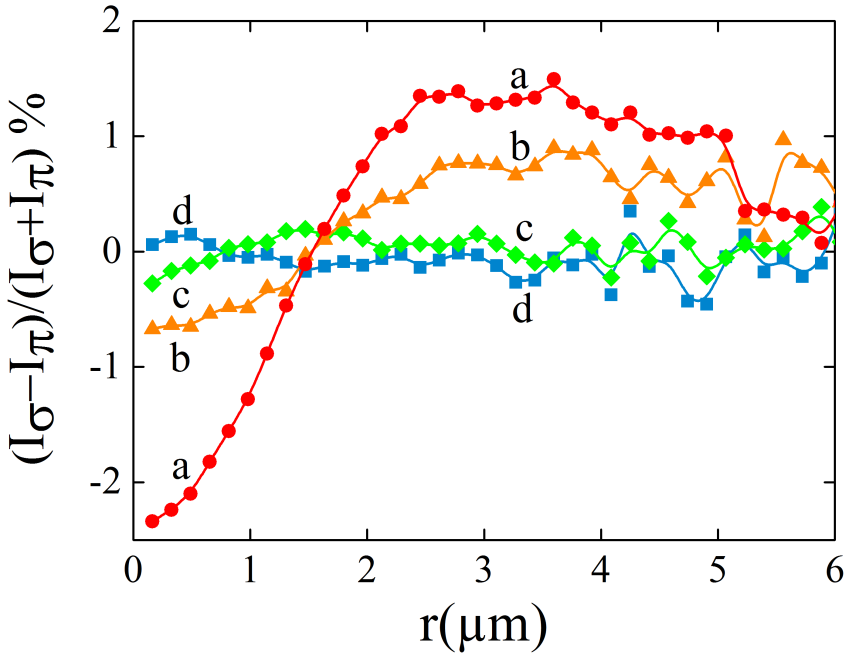


**Figure 6.4:** Relative difference between the luminescence intensity profiles obtained under circularly-polarized excitation ($\sigma$) and under linearly polarized excitation ($\pi$), for different power densities, a) 2.33 mW, b) 0.95 mW, c) 0.41 mW and d) 65 nW. For each excitation power, the only difference is the polarization of the photoelectron gas. A difference of the order of 2.5 % between both profiles is observed at high power at $r = 0$, revealing the spin-dependent diffusion of photoelectrons.

Using Eq.(5.29), the spin-dependence of the charge concentration at the center is approximately given by

$$\frac{\langle n_\sigma \rangle - \langle n_\pi \rangle}{\langle n_\sigma \rangle + \langle n_\pi \rangle} = \frac{\langle D_\pi \rangle - \langle D_\sigma \rangle}{\langle D_\pi \rangle + \langle D_\sigma \rangle} = -\frac{\delta \mathscr{P}^2}{2 + \delta \mathscr{P}^2} \tag{6.5}$$

from which we obtain $\delta = 0.58$, in agreement with the two preceding subsections.

## 6.3 Kinetic energy effects

Spatially resolved spectra centered at $r = 0$ for low and high power density are shown in Fig. 6.5. A comparison of the effect of Pauli blockade on electrons with different kinetic energies in the conduction band is therefore possible. In nondegenerate conditions (Curve a), the polarization does not depend on light energy and is consistent with the electronic polarization at the center for the low power curve of Fig. 6.2. As expected, in degenerate conditions (Curve b), the overall polarization is weaker than for Curve a because of the spin-dependent transport effects discussed above. However, this polarization decrease is mostly observed on the low energy side of the spectrum, while for energies above 1.52 eV, the two spectra almost coincide. It is concluded that the spin filter effect decreases with increasing kinetic energy in the conduction band. This is because occupation of the electronic states decreases with increasing energy, and therefore, electrons with high kinetic energy are less affected by the Pauli principle during an elastic scattering event.

## 6.4 Temperature dependence

An increase of electron temperature will result in an increase of the density of states, proportional to $T_e^{3/2}$, thus reducing the degree of degeneracy and the effects of Pauli blockade. Figure 6.6, which shows the spin polarization profiles obtained for different electronic temperatures at an excitation power of $P = 2.55$ mW, reveals a transition from a degenerate to a non-degenerate gas between $T_e = 90$ K (curve e) and $T_e = 110$ K (curve f). The electronic temperature that determines the transition into the non-degenerate regime, obtained by writing $n(0) = N_c$ and using Eqs. (6.2) and (6.1), and by neglecting the weak temperature dependence of $D_0$, is $T_e = 110$ K. This is in excellent agreement with the temperature evolution of the polarization profiles of Fig. 6.6.

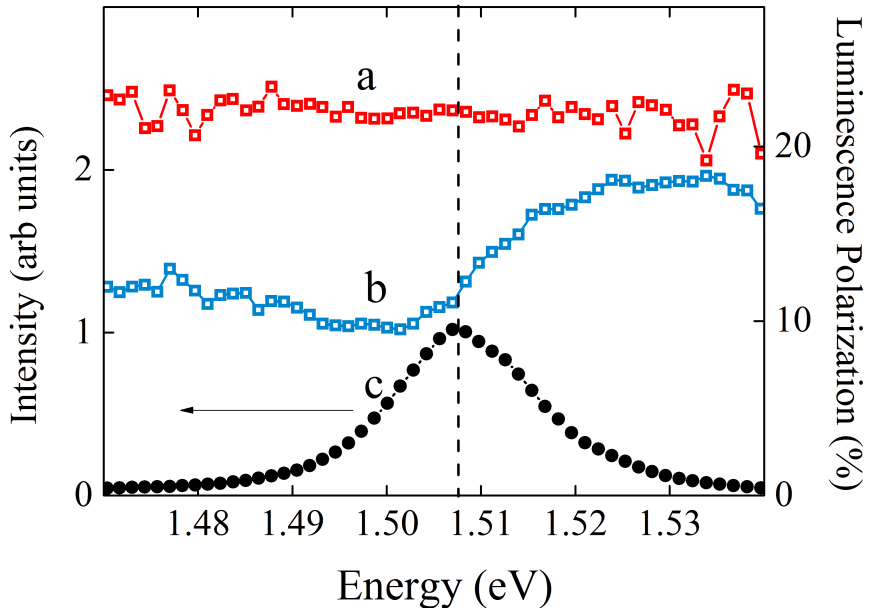


**Figure 6.5:** Dependence of spin polarization on kinetic energy. Curve a and Curve b show the spatially-resolved polarization spectrum at $r = 0$ and at 15 K for a power of 28 $\mu$W and 2.55 mW, respectively. Curve c shows for comparison the intensity spectrum at 2.55 mW at the center. Comparison between Curves a and b shows that the Pauli blockade effect is smaller for hot electrons.

## 6.5 Ruling out other possible interpretations of the experimental results

### 6.5.1 Hot electron effects

As suggested by Volkl et al. (2011) in the case of [110] quantum wells, it is tempting to conclude that the depolarization of thermalized electrons at the center rather arises from an increased efficiency of the local spin relaxation processes, caused by the larger hole concentration or by the increased temperature at the center. This hypothesis cannot explain the results for three main reasons : i) Such polarization loss can only concern electrons localized in potential fluctuations, since diffusive electrons will transmit their depolarization after diffusion. However, localized electrons only appear at lattice temperatures smaller than 10 K and are absent at the present higher temperature (Cadiz et al. (2014)). ii) Since the effective lifetime at $r = 0$ is of the order of $\omega^2/4D \approx 10$ ps, the polarization decrease at $r = 0$ would require an extremely strong, unphysical decrease of $T_1$ from its value of 1125 ps at low power (Cadiz et al. (2014)) iii) Since an increased

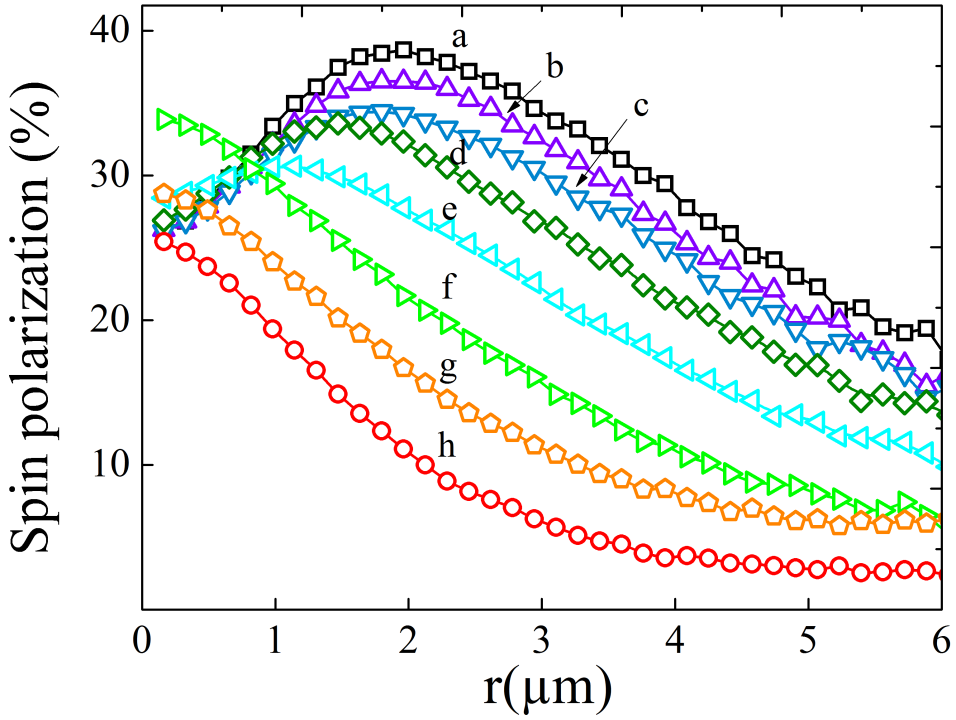


**Figure 6.6:** Temperature dependence of spin-dependent diffusion. Spin polarization as a function of space at excitation power of 2.55 mW and different values of the electronic temperature $T_e$ , a) 55 K, b) 57 K, c) 68 K, d) 82 K, e) 90 K, f) 110 K, g) 200 K and h) 360 K. The transition from the Pauli blockade to the non-degenerate regime occurs between 90 K and 110 K, in agreement with the expected temperature variation of the effective density of states, $N_c$.

spin relaxation at the center does not affect the charge density, it does not explain the observed dependences of the charge diffusion on intensity and polarization reported in Fig. 6.4.

### 6.5.2 Contribution of the substrate's luminescence

It could be that near $r = 0$, the total luminescence comes not only from the active $p^+$-GaAs layer but also from the substrate if the latter absorbs the photons that were not absorbed by the $p^+$-layer. If the substrate's luminescence is unpolarized and localized near $r = 0$ (for example, if the diffusion constant is smaller in the substrate), this could create a polarization dip at the centre of the images as those shown in Fig.6, with no relationship with diffusion of generate electrons in the p region. This problem was indeed observed in a sample consisting of a 2.3 $\mu$m thick, $p^+$ GaAs layer ($p = 6.5 \times 10^{19}$ cm$^{-3}$) surrounded by thin layers of p-doped AlGaAs ($p = 9.5 \times 10^{17}$ cm$^{-3}$) and grown over a

400 $\mu$m substrate of Si-Doped $n^+$-GaAs ($n = 2 \times 10^{18}$ cm$^{-3}$), as shown in Fig.6.7 a). In panel b) of Fig.6.7, the angular averaged polarization profiles at $T_L = 15$ K exhibit a very large polarization dip near $r = 0$ even at extremely low power densities such as 20 nW when the electrons are non degenerate. At $P = 0.14$ mW, a spatially-resolved spectrum was obtained at particular values of $r$, and their energy-averaged spin polarization (open squares) agrees well with the polarization profile measured by the luminescence imaging at those points.

Panel c) of Fig.6.7 shows these spectra and their energy-resolved spin polarization for $P = 0.14$ mW at selected distances from the excitation spot. It is seen that an excedent of light peaked at 1.53 eV is observed in the clearly non-exponential high energy part of the spectra, which is maximum at $r = 0$ and decreases rapidly in the region $r < 1$ $\mu$m. This luminescence is unpolarized as can be confirmed by the significant decrease of the spin polarization at an energy of 1.53 eV. This energy corresponds to the energy of maximum photoluminescence of the $n^+$-GaAs substrate at low temperature (Borghs et al. (1989)). This was confirmed by measuring the luminescence spectrum when the sample is photoexcited in the rear surface, when practically all of the incident energy is absorbed within the substrate. This photoluminescence, and its spin polarization, are shown as the dashed black curve and black closed circles, respectively, in Fig.6.7c).

We now show that this effect does not play a role for the samples decribed in sec.4.1, grown on a semi-insulating GaAs substrate whose luminescence is expected to be negiglible compared to that of the active layer. To confirm this, luminescence microscopy was also performed on a rectangular $p^+$-GaAs patch that was obtained from the samples described in sec.4.1, where the top epitaxial layer was patterned and selective wet etching of the GaInP layer was used in order to create free standing patches of GaAs as the one shown in panel a of Fig.6.8 (Arscott et al. (2010)). This patch is attached via capillary forces to a 0.2 mm thick SiC support, which is transparent to the laser energy and provides a good thermal contact with the sample holder. The polarization profiles obtained on this patch and on the sample grown in the semi-insulating wafer were compared at both room and low ($T_L = 15$ K) lattice temperature.

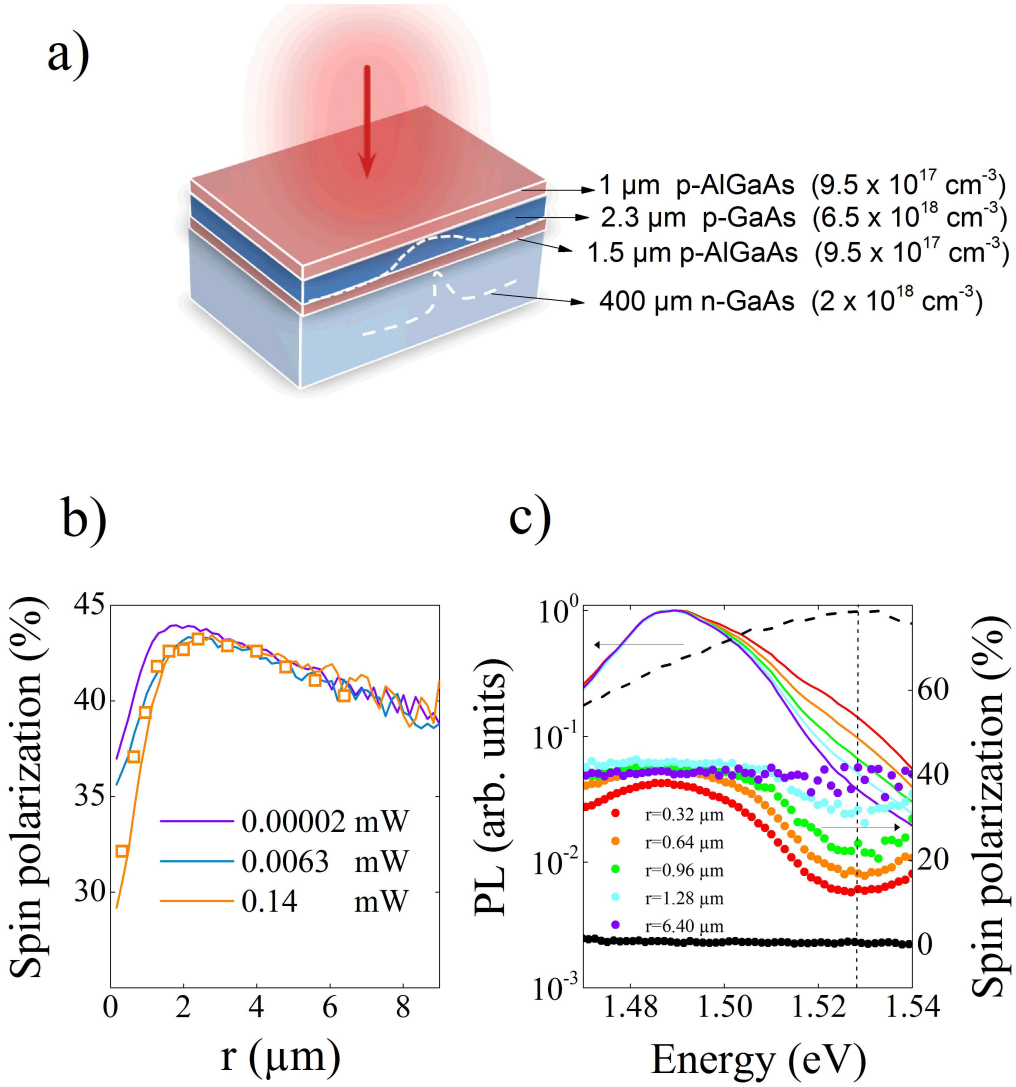


**Figure 6.7:** a) Schematic of a layered $p^+$-GaAs sample grown on top of a $n^+$-GaAs substrate. The dashed lines represent the photoelectron density at the steady state in the $p^+$-GaAs and in the substrate, where the spin polarization is small. The volume density of impurities in both layers being comparable, luminescence coming from the $p^+$-GaAs layer will be mixed with the one coming from the $n^+$-GaAs Substrate. b) Measured spin polarization profiles at $T_L = 15$ K. It is seen that a dip near $r = 0$ exists independently of the degree of degeneracy of the photoexcited electrons, since it is visible at extremely low power excitation. The squares represent the energy-averaged spin polarization calculated from local spectra at $P = 0.14$ mW. c) Photoluminescence spectra and its energy-resolved spin polarization at $P = 0.14$ mW for selected values of $r$. It is observed that with respect to the spectrum far from the excitation spot ($r = 6.4$ $\mu$m), as $r$ approaches to $r = 0$, an excedent of unpolarized luminescence at 1.53 eV is apparent, as can be confirmed with the measured energy-resolved spin polarization (closed circles). The energy of this excedent luminescence corresponds to the measured peak energy of the substrate's luminescence, shown by the dotted black curve, whose degree of circular polarization is near to zero, as shown by the closed black circles.

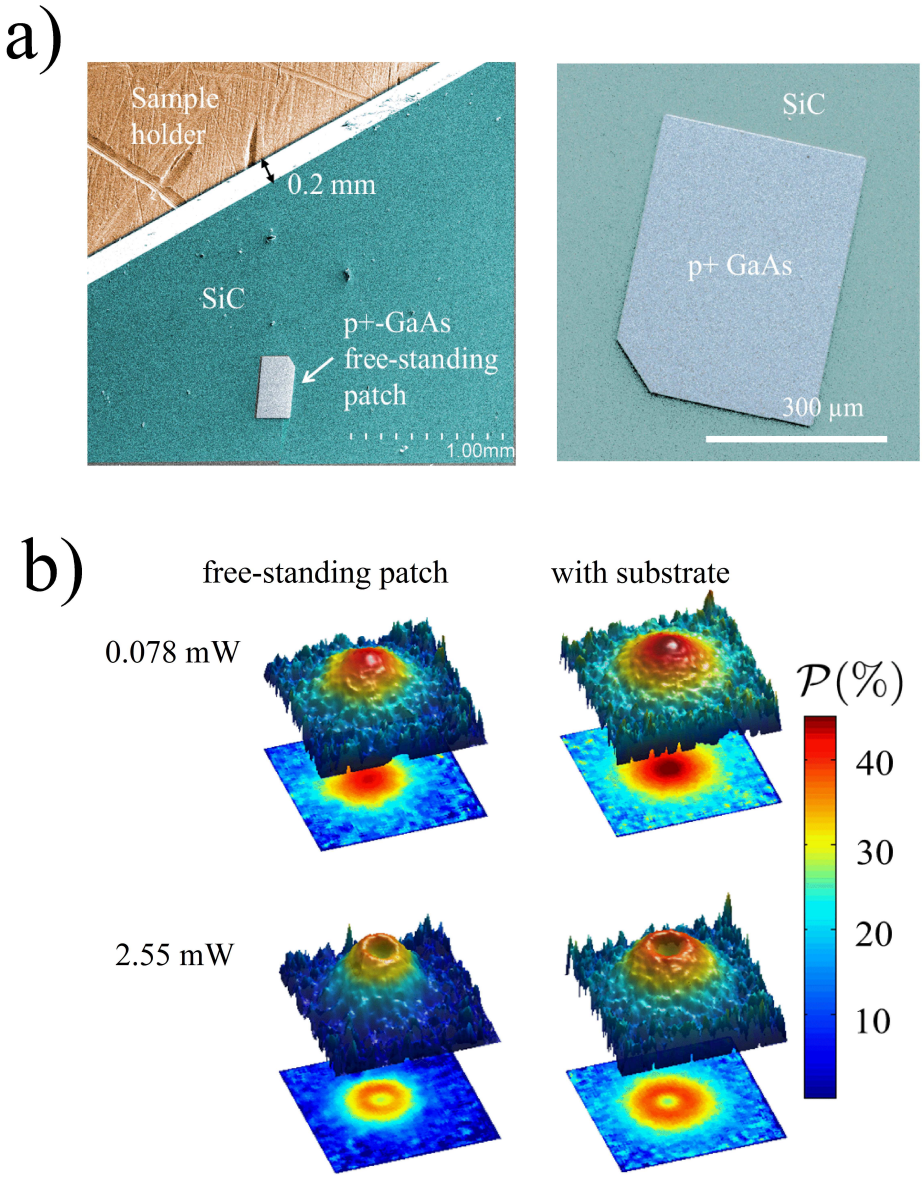


**Figure 6.8:** a) SEM image of a 3 $\mu$ thick $p^+$-GaAs free-standing patch attached to a SiC support. b) Images of the spin polarization for the free-standing patch at low temperature. The appereance of a polarization dip is also observed and compared to the images of Fig.6 at same excitation power obtained for the sample with the semi-insulating GaAs substrate.

Panel b) of Fig.6.8 shows the polarization images at $T_L = 15$ K at low ($P = 0.078$ mW) and high (2.55 mW) power excitation, for the patch sample and for the sample with substrate, whose polarization images are reproduced from Fig.6. The polarization dip becomes apparent and qualitatively the same result is obtained regardless of the presence of the semi-insulating GaAs substrate. In conclusion, it is shown that any artifact coming from the semi-insulating GaAs substrate can be ruled out.

## 6.6 Numerical solution of the coupled diffusion equations

Both the observed spin filter effect and the spin-dependent charge diffusion are interpreted as consequences of the Pauli principle, according to the theory of Chapter 5. In order to determine the relative importance of the various processes considered in Chapter 5, we have numerically solved the system of Eqs.(5.42),(5.43), (5.44) and (5.45), using an approximate method described in Appendix 8.1.5 and taking the measured transport parameters indicated in Table 6.6. These parameters were all determined independently, as described in Chapter 4, so that no fitting procedure was used.

As seen in Fig.5.1, a key parameter is the exponent $p$ related to the kinetic energy dependence of the momentum relaxation time, supposed to be of the form of Eq.(5.20), which we reproduce here:

$$\tau_m(\varepsilon) = a(T_L, T_e)\varepsilon^p,$$

where the exponent $p$ depends on the primary scattering process which can be modified by electrostatic screening (Chattopadhyay and Queisser (1981)). For example, scattering by ionized impurities gives $p = 3/2$, whereas when screened by holes, $p$ is reduced to $p = -1/2$.

The quantity $p$ can be measured using photoconductivity and photoHall measurements at low excitation power, as shown in Fig.6.9. Using a very large laser excitation spot ($\omega \sim w$, where $w$ is the width of the Hallbar) to ensure that the photoelectron concentration is homogeneous over the Hall bar, the ratio $r_H = \mu_e^H/\mu_e$ of the Hall mobility $\mu_e^H$ to the drift mobility of minority electrons can be found. The quantity $p$ is found using (Popovic (2004))

$$r_H = \frac{\Gamma(5/2+2p)\Gamma(5/2)}{[\Gamma(5/2+p)]^2} \tag{6.6}$$

The result is $r_H = 0.95 \pm 0.25$ at $T_e = 95$ K and $r_H = 0.8 \pm 0.25$ at $T_e = 300$ K, in agreement with the values close to unity obtained for majority electrons in n-GaAs by Look et al.

## 6.6. Numerical solution of the coupled diffusion equations

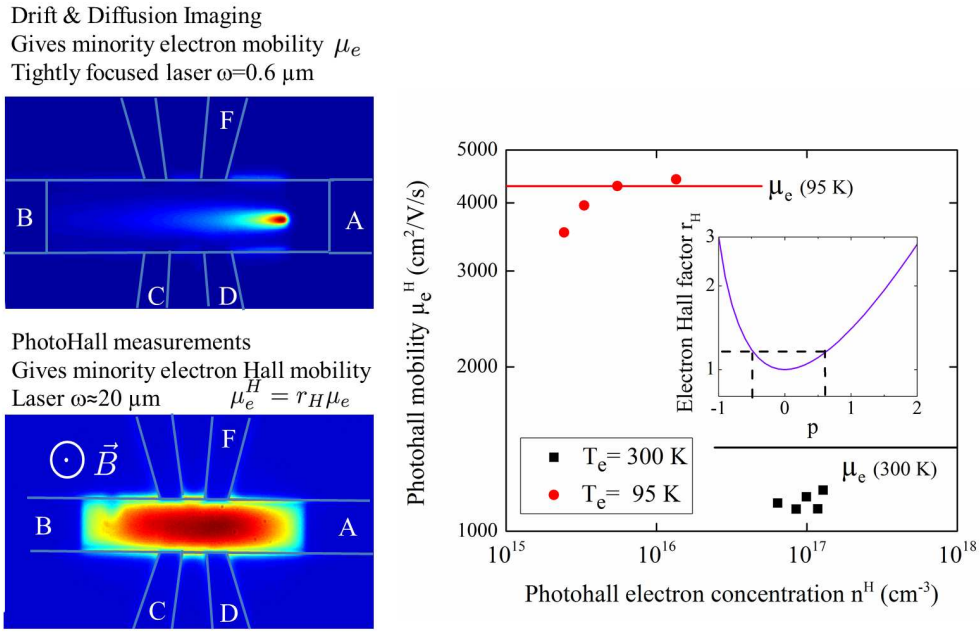


**Figure 6.9:** Left: Determination of the electron Hall factor $r_H$ is possible by combining the spatially resolved drift and diffusion of photoelectrons which, together with the electron lifetime, gives $\mu_e$, and photohall measurements under a perpendicularly applied magnetic field, which gives $\mu_e^H = r_H \mu_e$. In the latter, it is important to uniformly excite the sample, since a non-uniform photoelectron concentration will give false values for $\mu_e^H$ Right: Measured photohall mobility $\mu_e^H$ as a function of photoHall concentration $n^H$ at $T_e = 300$ K and $T_e = 95$ K. The lines are the measured mobilities at the same temperatures obtained by imaging the drift and diffusion profiles. It is seen that both experiments give similar values, $r_H = \mu_e^H/\mu_e \approx 0.95 \pm 0.25$ at 95 K and $r_H = 0.85 \pm 0.25$ at $T_e = 300$ K. The inset of the right panel shows the expected dependence of $r_H$ (Eq.(6.6)) on the exponent $p$ in Eq.(5.20).

(1996). Using these values and the graphical representation of Eq.(6.6) in the inset of Fig.6.9, $p$ is found to lie between approximately -0.5 and 0.5, in qualitative agreement with the predictions of the Brooks-Herring model (Chattopadhyay and Queisser (1981)) for screened collisions by charged impurities. The small value of $p$ implies that the mobility is almost independent of concentration, and, therefore, $\zeta$ defined in Eq.(5.21) is close to 1.

Finally, for the numerical resolution of the coupled diffusion equations, the excitation profile was modelled by a function of the form

$$G(r,z) = \frac{\alpha P}{2\pi\omega^2 h\nu} e^{-r^2/\omega^2} e^{-\alpha z},$$

where $P$, $h\nu$ and $\omega$ are the laser power, energy, and radius, respectively, and where $\alpha$ is

the absorption coefficient. The electronic temperature as a function of space, according to sec.3.3.3, is modelled by a Gaussian function of the form of Eq.(3.11):

$$T_e(r,z) = [T_e(0) - T_e^0]e^{-r^2/(\omega_T^2)}e^{-z/\omega_T} + T_e^0,$$

where $T_e^0$ is the temperature far from the excitation spot, and where $\omega_T$ is of the order of 1 $\mu$m. The polarization profiles were then calculated using Eq.(3.3) and Eq. (3.4).

### 6.7. Interpretation

| Parameters used in the numerical calculation | | |
|---|---|---|
| Parameter | Symbol | Value |
| Laser excitation energy | $h\nu$ | 1.59 eV |
| Laser beam radius | $\omega$ | 0.6 $\mu$m |
| Absorption coefficient | $\alpha$ | 1 $\mu m^{-1}$ |
| Laser power | $P$ | $0.0028$, 0.45, 1.03 and 2.55 mW |
| Reabsorption coefficient | $\alpha_l$ | $1/3$ $\mu m^{-1}$ |
| Sample thickness | $d$ | 3 $\mu$m |
| Surface recombination velocity | $S$ | $4.6 \times 10^4$ cm/s |
| GaAs dielectric constant | $\varepsilon_r$ | 10 |
| Reflectivity of the sample | $R$ | 0.3 |
| Electron diffusion constant | $D_e$ | 37 $cm^2/s$ |
| Charge lifetime | $\tau_e$ | 335 ps |
| Spin relaxation time | $T_1$ | 1150 ps |
| Hole diffusion constant | $D_h$ | 0.83 $cm^2/s$ |
| Hole mobility | $\mu_h$ | 200 $cm^2/V/s$ |
| Ionized acceptors | $N_A^-$ | $10^{18}$ $cm^{-3}$ |
| Electron temperature at low density | $T_e^0$ | 50 K |
| Electron temperature at $r = 0$ | $T_e(0)$ | 60 K at 0.45 mW, 65 K at 1.03 mW, 75 K at 2.55 mW |
| Temperature gradient radius | $\omega_T$ | 1 $\mu$m |
| Electron mobility | $\mu_e$ | 8800 $cm^2/V/s$ at $T_e = 50$ K, $\mu_e \propto 1/T_e$ |

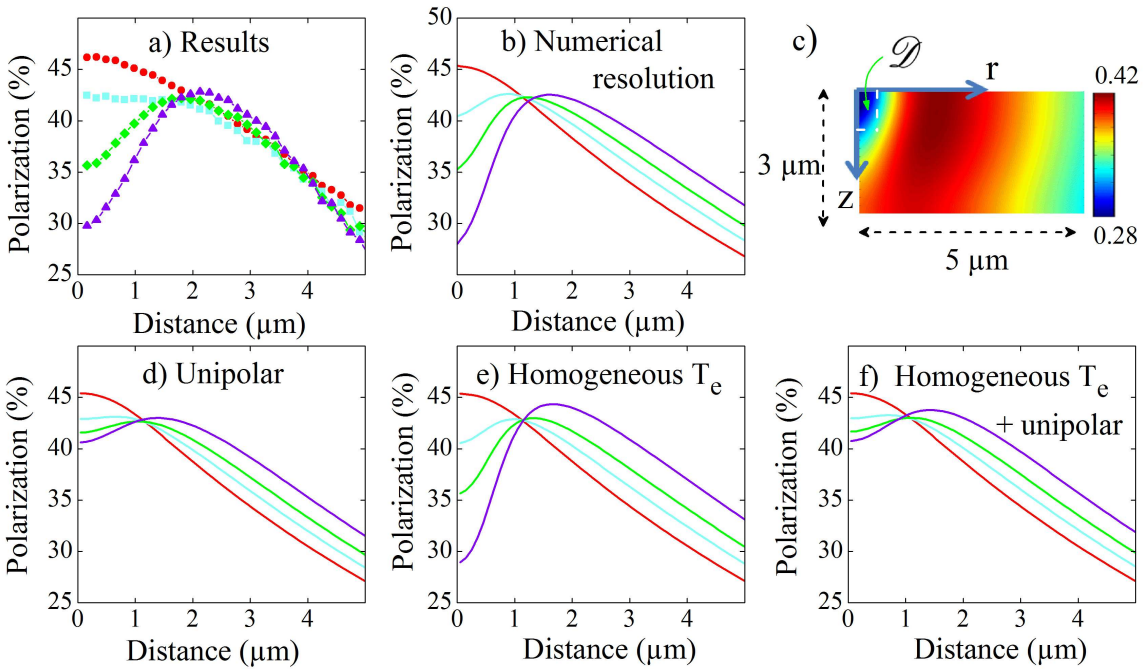


**Figure 6.10:** Panel a shows the experimental polarization profiles at $T = 15\ K$ as a function of excitation power : 28 $\mu$W (filled circles), 0.45 mW (filled squares), 1.03 mW (filled diamonds), 2.55 mW (filled triangles). Panels b, d, e and f show with the same symbols, the corresponding calculated profiles. Panel b show calculated profiles including all effects which modify spin transport. Panel c shows the calculated spatial distribution of the polarization for an excitation power of 2.55 mW. The profiles of Panel d were obtained in the simplest unipolar case. With respect to Panel b, the profiles of panel d do not consider ambipolar diffusion, those of Panel e do not consider thermoelectric currents, and those of Panel f neglect both ambipolar diffusion and temperature gradients and thus illustrate the conditions of spin-grating experiments.

## 6.7 Interpretation

The numerically calculated polarization profiles are shown in panel b of Fig.6.10 for the same excitation powers as Fig.6.2, whose curves are reproduced in panel a of Fig.6.10, for better comparision. These profiles correspond quite well with the experimental results of panel a, apart from a slight difference in the position of the polarization maximum. As shown in Panel c of Fig.6.10, the polarization dip is restricted mainly to a characteristic zone labelled $\mathscr{D}$, defined by $z < 1\ \mu$m and $r < 0.3\ \mu m$. Conversely, for $r \approx 1.5\ \mu m$ and $z < 1\ \mu m$, the polarization maximum is as large as 42%. At the highest excitation power, one calculates that the averages of the concentrations over $\mathscr{D}$ are $\langle n_+(\mathscr{D})\rangle \approx 2.8 \times 10^{17}$ cm$^{-3}$ and $\langle n_-(\mathscr{D})\rangle \approx 1 \times 10^{17}$ cm$^{-3}$. These values are higher than the spin-resolved effective density of states at $T_e = 80$ K which is $N_c^s \approx 3\times10^{16}$ cm$^{-3}$.

### 6.7.1 Strong effect of ambipolar diffusion

The importance of ambipolar diffusion is seen from Panel d of Fig.6.10, which shows the profiles calculated in the unipolar case, by considering only Eq.(5.42) and Eq.(5.43) and by taking $E = 0$. It is striking to see that, in this case, the spin filter effect is almost absent, as one observes only a small polarization dip in the profiles at $r = 0$. With the present values of $N_A$ and $n$, ambipolar diffusion results in reduced ambipolar diffusion constants $D^a_{cc}$ and $D^a_{cs}$ (see Appendix 8.1.5), by the same amount

$$\beta_h = \frac{N_A^- + n}{(N_A^- + n) + (\mu_0/\mu_h)[n_+\zeta(n_+) + n_-\zeta(n_-)]}$$

defined by Eq.(8.42). The latter quantity can be quite small since at low temperature $\mu_e/\mu_h \approx 85$. This results in an increase of the effective lifetimes at the centre, $\sim \omega^2/D$, and therefore of the concentration and of the degeneracy. In the unipolar case, we find at the highest excitation power $\langle n_+(\mathscr{D})\rangle \approx 5.2 \times 10^{16}$ cm$^{-3}$ and $\langle n_-(\mathscr{D})\rangle \approx 2.2 \times 10^{16}$ cm$^{-3}$. The total concentration is smaller than its above ambipolar value by a factor of $\approx 2$.

Note finally that the concentration is still slightly larger than $N_c^s$ so that some amount of degeneracy is still present. Indeed we calculate $D_+/D_- = 1.26$, i.e quite similar to the value obtained with the full calculation. This is because, in Eq.(5.24), the decrease of $\delta$ caused by the smaller concentration is compensated by the polarization increase so that the actual value of $D_+/D_-$ only weakly depends on concentration. On the other hand, the actual value of the polarization in $\mathscr{D}$ is the result of a self-consistent equilibrium and can be relatively sensitive to the concentration. [1]

[1] Another effect of ambipolar diffusion is to introduce an electrostatic coupling between spins + and spins − via the holes so that the ambipolar diffusion matrix $D^a_{ij}$ is not diagonal. This can be seen in the simpler case where the concentrations are spatially homogeneous, by performing linear combinations of the hole diffusion equation and of the diffusion equations for spins ± respectively, in the same way as in Smith (1978)

### 6.7.2 Marginal effect of Soret currents

Panel e shows the profile calculated under the same conditions as Panel b, except that the Soret charge and spin currents are neglected ($\vec{\nabla}T_e = 0$). Here $T_e$ is taken as spatially homogeneous and equal to its measured value at $r = 0$. Apart from the highest power where the profile is slightly shifted upwards, the profiles are nearly the same as in panel b implying that the Soret current plays a negligible role in these experiments [2]. The relative temperature gradient $\vec{\nabla}_r T_e/T_e$ strongly varies with distance. As found from Curve a of Fig. 3.5, its value at high power is very small near $r = 0$, reaches 1.3 $\mu$m$^{-1}$ in a very short interval near 0.6 $\mu$m, and then decreases to 0.3 $\mu$m$^{-1}$. In comparison, the charge relative gradient $\vec{\nabla}_r n_e/n_e$, found using Fig. 4.6, is almost independent of distance. Its value is of the order of $1\mu$m$^{-1}$ which, within experimental uncertainties, is larger than the relative temperature gradient at most distances. Using Eq.(5.39), it is thus concluded that the temperature gradient is not sufficient to obtain significant Soret currents.

## 6.8 Transient spin grating experiments

The question arises whether the same effect of the Pauli principle could be observed using the more conventional spin grating technique. Spin diffusion on this sample has also been measured with the latter technique performed at Christopher Weber's laboratory in Santa Clara University. The sample is illuminated with two obliquely incident, coherent laser pulses with crossed linear polarizations. As described previously in sec.2.3, this creates a uniform photoelectron density but with a sinusoidal variation of their spin polarization, with a wavevector $q$ which can be varied by changing the angle of incidence of the two pulse beams. This spin wave generates in turn a sinusoidal variation in the index of refraction through the Kerr effect.

The laser pulses have a Gaussian radius of 57 $\mu$m and a center wavelength of 800 nm, duration 120 fs, and repetition rate 80 MHz. At the highest fluence, of $f = 7.9$ $\mu$J/cm$^2$,

[2] The heating of the electron gas is given by the approximate balance equation $C_v(T_e - T)/\tau_{eff}(0) = g(0)\Delta E/n(0) - [dE/dt]\,|_{\rm phon}$. Here $C_v \approx 3k_B T_e/2$ is the heat capacitance per electron, $\Delta E$ is the energy per electron given to acoustic modes and $[dE/dt]\,|_{\rm phon}$ is the rate of energy exchange to the phonons, calculated in Ref. Pugnet et al. (1981). Using this simple equation, we find $\Delta E = 15$ meV, in good agreement with the initial kinetic energy after emission of two optical phonons.

each pair of pump pulses photoexcites electrons and holes at a density of $n \approx 3{\times}10^{17}$ cm$^{-3}$. The sample is kept at $T_L = 15$ K. According to the results discussed above, at this electron density degeneracy is expected to increase the diffusion constant via Eq.(5.23). Note that, in contrast with the luminescence microscopy experiment, ambipolar coupling and thermal currents are absent in this experiment. The grating's amplitude is monitored through diffraction of a time-delayed probe pulse, whose intensity is about 1/10 of that of one pump pulse. The amplitude decays through spin relaxation, electron-hole recombination, and spin diffusion at a rate given by Eq.(2.4), which we reproduce here :

$$1/\tau(q) = \frac{1}{\tau_s} + q^2 D_s$$

Measurement of the decay rate $1/\tau(q)$ at several $q$ determines the spin diffusion constant $D_s$. The diffracted probe amplitude is measured in a reflection geometry. Spin decay curves at $f = 3.1$ $\mu$J/cm$^2$ are shown in Fig.6.11(a). It is seen that the spin grating lifetime $\tau(q)$ decreases with increasing $q$.

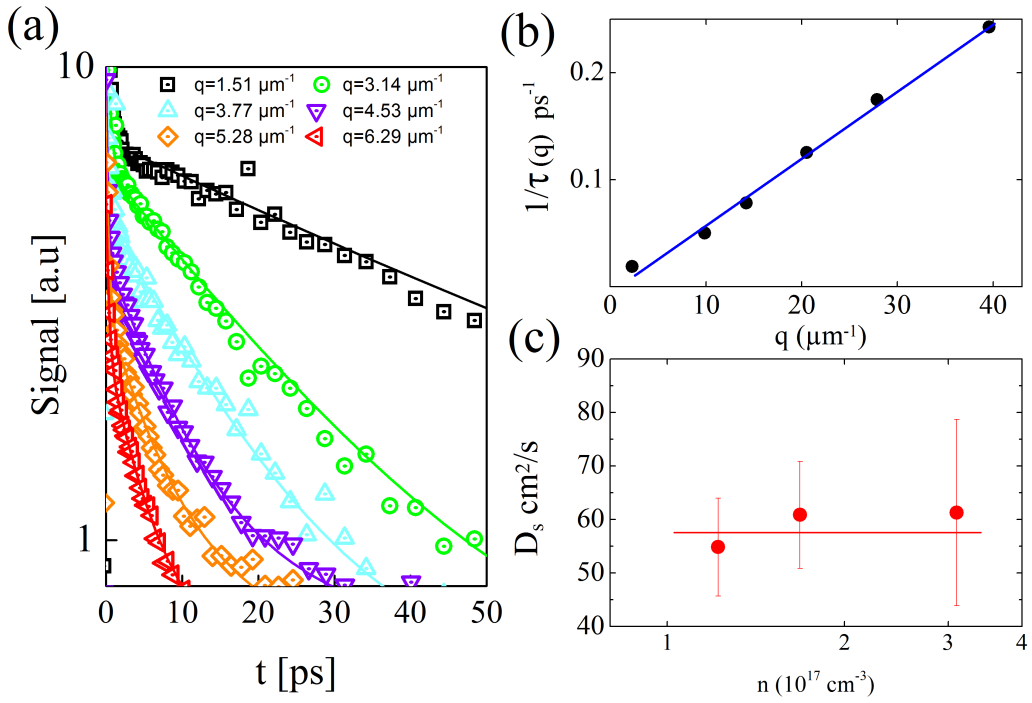


**Figure 6.11:** a) Spin transient signal for a fluence of 3.1 $\mu$J/cm$^2$ as a function of time delay for different values of $q$. The decay rate is faster when $q$ is increased, according to spin diffusion and relaxation. b) The $1/\tau(q)$ v/s $q^2$ plot is well fitted by a line, in agreement with Eq.(2.4), and whose slope gives the spin diffusion constant $D_s$. c) Measured spin diffusion constant as a function of photoelectron concentration. No significant dependence in concentration is observed.

Figure 6.11(b) shows the $q^2$-dependence of the decay rate $1/\tau(q)$. Fitting with Eq.(2.4) permits to measure the spin diffusion constant $D_s$. According to Eq.(5.23), at low temperature and at this fluence one would expect $D_s$ to depend strongly on the photoelectron concentration. However, when the fluence is increased by a factor of 2.5, no significant variation in $D_s$ is observed, as shown in Fig.6.11(c). It should be noted that at the lowest value of $q$, the spin grating decays within 50 ps and much faster at higher $q$. According to the time-resolved measurements discussed in sec.4.2.3, the electrons cool down with a characteristic time of $\sim 70$ ps. Thus, the spin grating signal decays faster than the time required for the photoelectron gas to cool down, so indeed it is not surprising to measure a rather constant diffusivity $D_s$. Another reason is the absence of electrostatic coupling with holes. If Coulomb coupling with photoholes was present, as in the microluminescence experiments, the decay rate of the spin grating would be highly supressed, and therefore the signal could persist even after the electrons have cooled down. However, since in this experiments the photoelectron density is homogeneous in space, spin diffusion is not affected by the holes.

These results are in agreement with the predicted polarization profiles at steady state, calculated by considering the unipolar limit without temperature gradients, $T_e$ being fixed to its measured value at $r = 0$. This situation is reminiscent of spatially homogeneous configuration of spin grating experiments. These profiles are shown in panel f) of Fig.6.10. In this case the polarization dip near $r = 0$ has almost disappeared. Observation of the Pauli blockade driven spin filter effect thus requires spatially inhomogenous electron and hole concentrations. This means that the usual spin grating technique may not be well adapted to the observation of Pauli-blockade effects in spin transport. On the other hand, for spin gratings, $T_e$ is also uniform in space, meaning that the charge and spin Soret effects are absent, a situation which should slightly increase the magnitude of Pauli-blockade phenomena. Given that heating of the photoelectron gas is unavoidable during high intensity photoexcitation, the ideal conditions for measuring the largest possible Pauli blockade effects are highly inhomogenous photoelectron and hole concentrations and spatially uniform temperatures.

## 6.9 Drift of degenerate spin-polarized electrons

In order to detect a possible spin-dependence of the mobility, according to Eq.(5.21), I have measured the modification of the polarization profiles caused by application of an electric field. If in degenerate conditions, $\mu_+ > \mu_-$ so that the drift length $L = E\mu\tau$ will be larger for the majority spin electrons, one would expect the polarization maximum observed in sec.6.1 to be attained at a distance comparable to the spin drift length, which may be adjusted since the latter depends linearly on the electric field. In this section, I will show that this is not the case regardless of the spin-dependence of the mobility.

I will show here that the effects are dominated by the Coulomb coupling between photoelectrons and the hole gas so that the internal electric field produced by the spatial separation of electrons and holes has a magnitude that can be much larger than the externally applied electric field, and moreover, it is of opposite sign. Coulomb coupling with holes can be accounted for if one considers an effective drift-diffusion equation for the photoelectron and for the spin density. In a non-degenerate regime, it is given by (see appendix 8.1.4):

$$\begin{aligned} g - n/\tau + \vec{\nabla} \cdot [n\mu_a \vec{E}^{\text{ext}} + D_a \vec{\nabla} n] = 0 \\ \mathscr{P}_i g - s/\tau_s + \vec{\nabla} \cdot [s\mu_a \vec{E}^{\text{ext}} + D_e \vec{\nabla} s] = 0 \end{aligned} \tag{6.7}$$

where $D_a = (n\mu_e D_h + (n + N_A^-)\mu_h D_e)/(n\mu_e + (n + N_A^-)\mu_h)$ and $\mu_a = \mu_h N_A^-/(n\mu_e + (n + N_A^-)\mu_h)$ are the ambipolar diffusion constant and mobility, defined by Eqs.(8.40) and (8.39), respectively, and where $\vec{E}^{\text{ext}}$ is the applied electric field. The ambipolar mobility, which is close to zero when $n \gg N_A^-$, takes into account the screening of the external electric field by the hole gas. This model can be compared with a complete 2-D numerical resolution of Eqs.(5.42),(5.43),(5.44) and (5.45). For simplicity, the electron temperature is kept constant at the measured value at low power of $T_e = 53$ K, so no thermal currents are included. The transport parameters are those measured in Chapter 4 at $T_e = 53$ K ($D_e = 47$ cm$^2$/s,$\mu_e = 11000$ cm$^2$/V/s, $\tau_e = 360$ ps, $T_1 = 1044$ ps, $\mu_h = 100$ cm$^2$/V/s).

Figure 6.12a) shows the measured charge density images for an applied electric field of

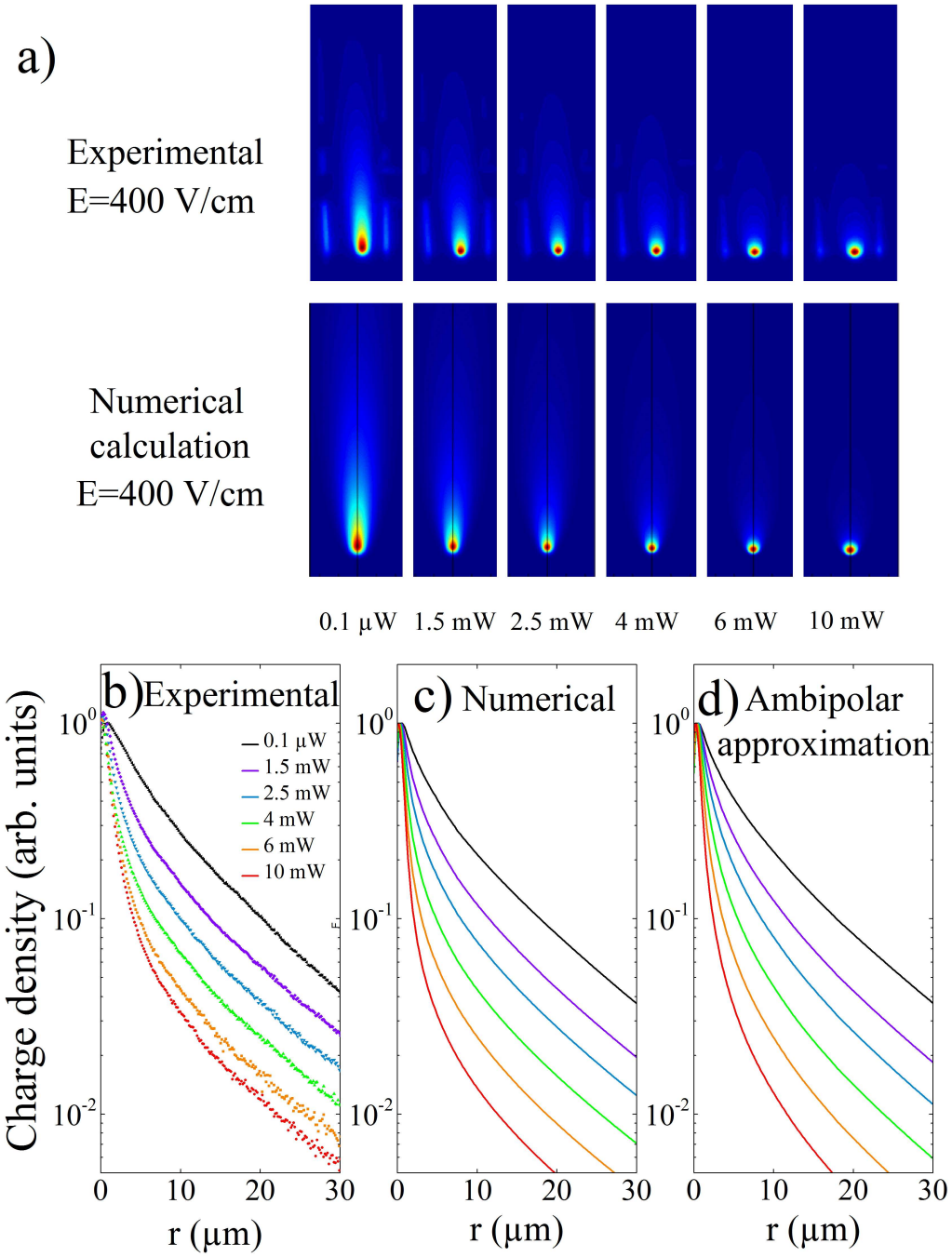


**Figure 6.12:** Panel a) shows the measured charge density images as a function of power and for an applied electric field of 400 V/cm. Also shown is a numerical calculation that takes into account Coulomb coupling of electrons with holes. Panel b) are cross sections of the images of panel a) along the direction of the electric field. An excellent agreement is observed between the experimental curves and the numerical calculations shown in panel c), except for the highest excitation powers since heating of the electron gas is not taken into account. Also shown in panel d) is a simplified numerical calculation by considering a single diffusion equation for the electrons with an effective ambipolar mobility.

400 V/cm and different values of the excitation power. It is seen that as the concentration increases, the apparent drift length is significantly reduced. The corresponding profiles (normalized to unity at $r = 0$) along the direction of the electric field are shown in panel b). This is indeed predicted by the profiles of panel c), corresponding to a numerical resolution of Eqs.(5.42),(5.43),(5.44) and (5.45). An excellent agreement is obtained between them and the experimental profiles of panel b), except for large powers since heating of the electron gas is neglected in the model. Also shown in panel d) is a numerical calculation obtained by using an effective ambipolar mobility and without considering degeneracy, as in Eq.(6.7). This simplified calculation reproduces all the relevant features due to Coulomb coupling with holes. The corresponding results for the spin density, as well as the predicted behaviour by using either the complete numerical calculation or the simplified model considering an ambipolar mobility, are shown in Fig.6.13.

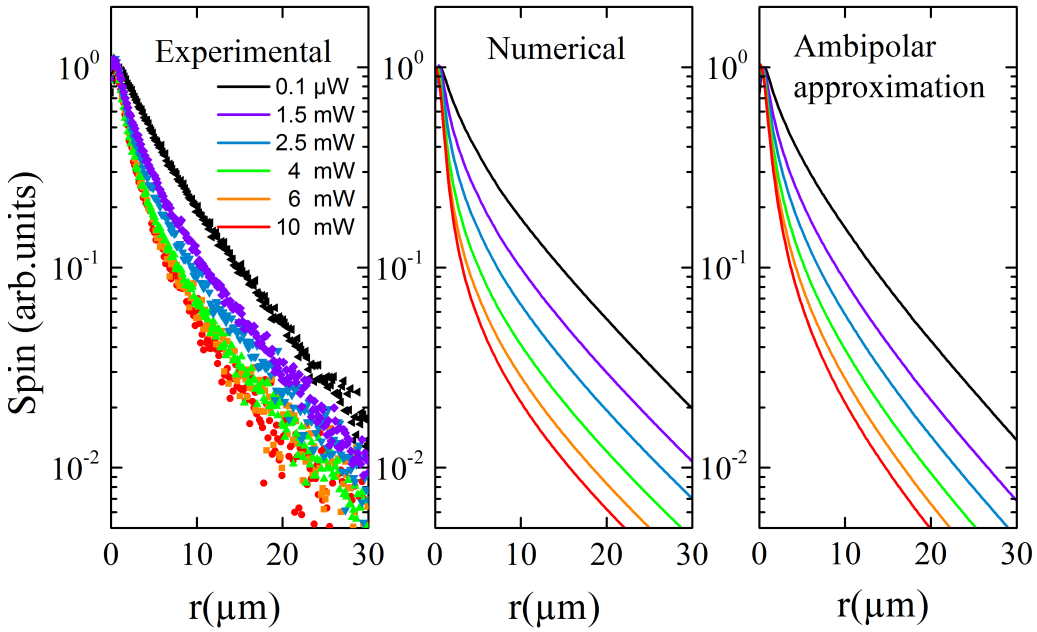


**Figure 6.13:** Left: measured spin profiles for an electric field of $E = 400$ V/cm and different excitation powers. Middle: spin profiles as predicted by a complete numerical calculation. Right: spin profiles obtained by a simplified model that uses an effective ambipolar mobility.

The total electric field, as well as the relative difference between the photoelectron density $n$ and the photohole density $\delta p$ are shown in Fig.6.14, for the same parameters used in

the complete numerical calculation of Fig.6.12 and 6.13. It is seen that, in the direction of the electron drift, quasi-neutrality is observed, with a relative difference between $n$ and $\delta p$ of about $10^{-4}$. This is possible due to the prescence of an internal electric field whose magnitude can be much stronger than the field applied between the contacts of the Hall bar.

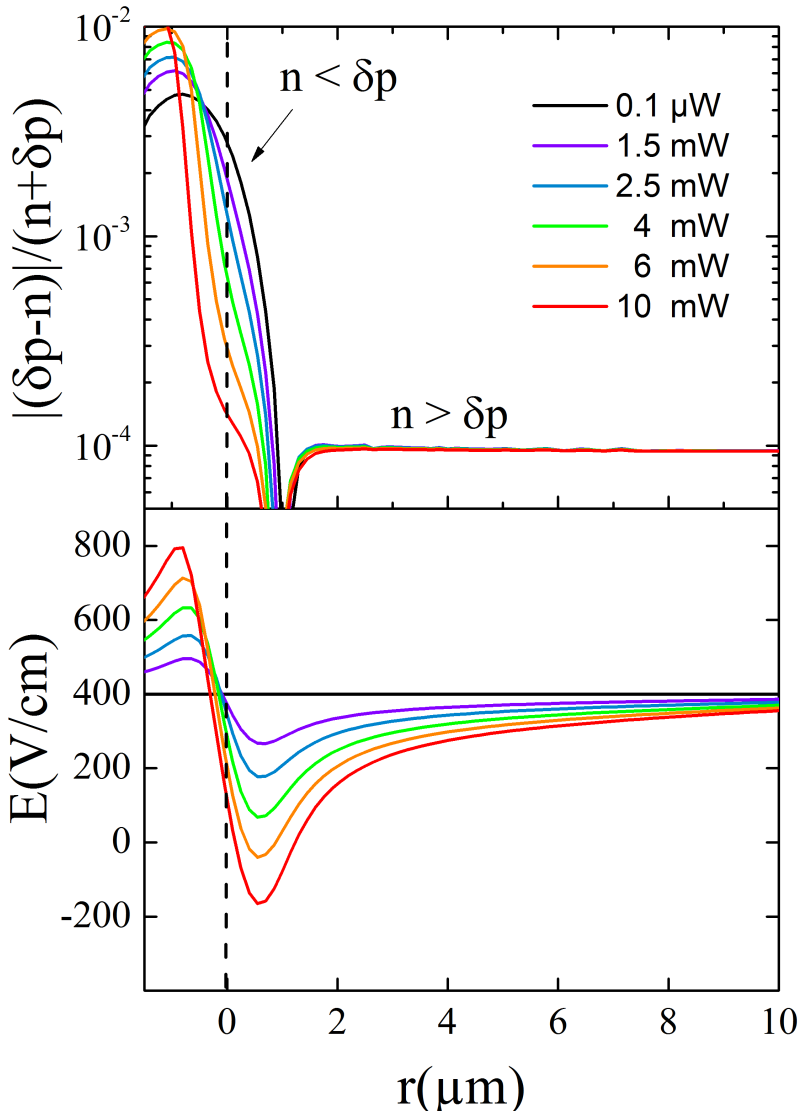


**Figure 6.14:** Top: spatial dependence of the relative difference between the photoelectron and the photohole density for an applied electric field of 400 V/cm and different values of the excitation power. Bottom: total electric field in the same conditions as in the top panel. It is seen that for $r > 0$ and over several $\mu$m, the total electric field is significantly reduced with respect to the applied 400 V/cm.

### 6.9. Drift of degenerate spin-polarized electrons

We now discuss the observed polarization profiles, as can be seen from Fig.6.15, where the images of the spin polarization as a function of applied electric field and excitation power are shown. The electronic temperature is $T_e = 40$ K at low density and zero-electric field.

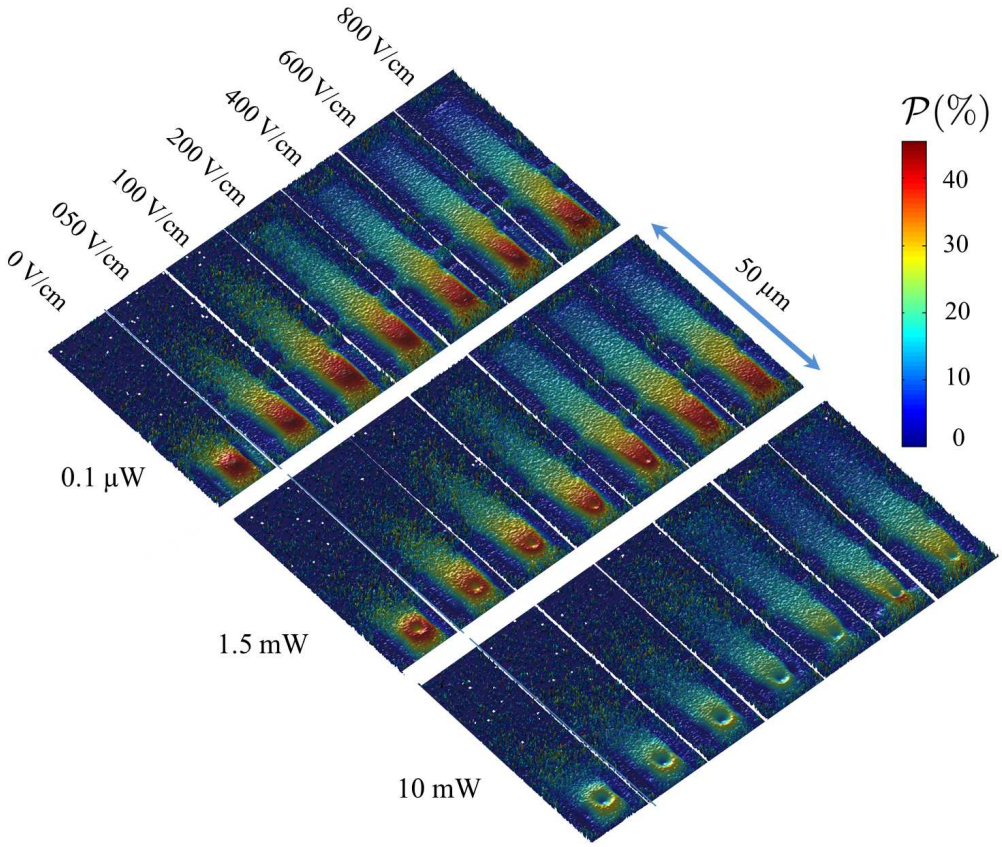


**Figure 6.15:** Measured spatial dependence of the spin polarization for a 1.55 eV excitation at $T_L = 15$ K as a function of the applied electric field and for different values of the excitation power. In the degenerate regime, the position of the polarization maximum does not depend on the applied electric field, whereas the amplitude of the polarization dip decreases with increasing $E$. This is due to both heating of the electron gas and to the decrease in concentration at $r = 0$ as the electron's drift under the influence of the electric field.

Figure 6.16 a) shows the measured spin polarization profiles at a fixed power of $P = 2.55$ mW and different values of the applied electric field. As the latter increases, the polarization dip disappears due to a decrease in the level of degeneracy. The numerical calculation in panel a) of Fig.6.16 shows that indeed the polarization dip is expected to vanish with increasing electric field. Since the numerical calculation assumes no heating of the electron gas, it predicts a slightly higher global spin polarization, but it is in qualitative agreement with the measured spin polarization profiles. Remarkably, almost no

variation is observed in the numerical calculation between $p = 0$ (constant mobility) and $p = 3/2$ (spin-dependent mobility), where $p$ is defined in Eq.(5.21).

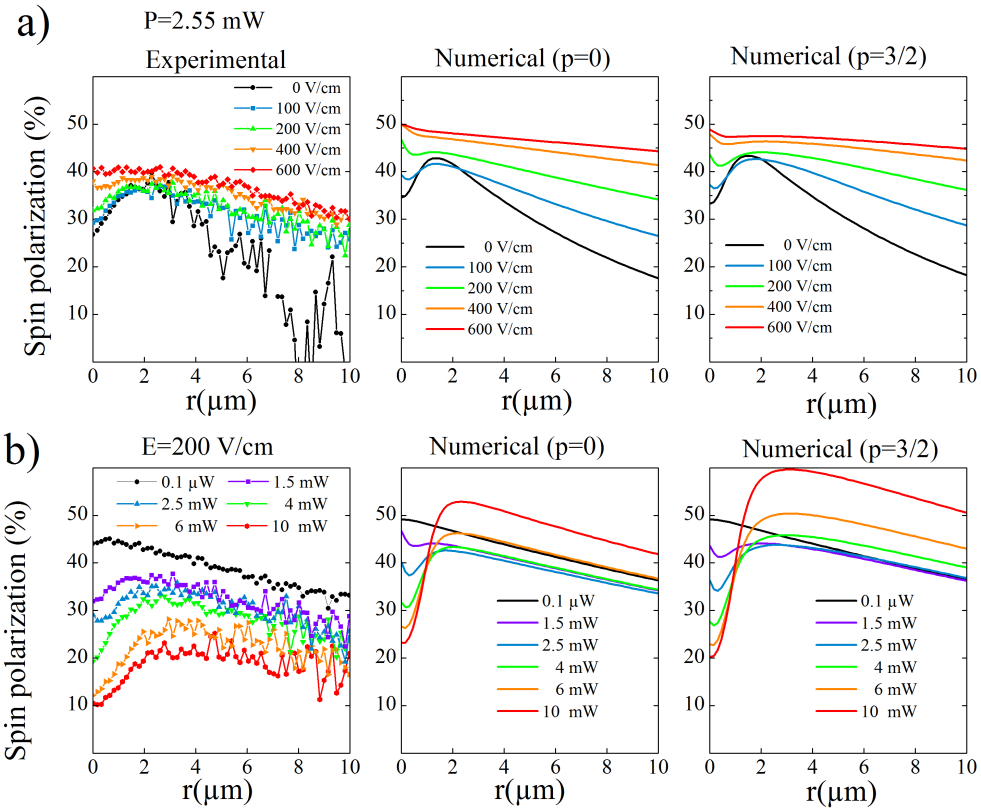


**Figure 6.16:** a) Measured spin polarization profiles at 2.55 mW as a function of the applied electric field. A numerical solution of the coupled diffusion equations for $p = 0$ and $p = 3/2$ is also shown. Regardless of the possible spin-dependence of the mobility, the polarization maximum does not drift under the influence of the electric field. b) Measured spin polarization profiles at a fixed electric field of $E = 200$ V/cm and different values of the excitation power, and the corresponding numerical calculations, showing that even in the ideal situation where the electron's temperature is kept constant at high power, and where the mobility is spin-dependent ($p = 3/2$), no significant drift of the polarization maxium is expected.

Figure 6.16b) shows the profiles observed at a fixed electric field of $E = 200$ V/cm and different values of the excitation power. For powers above 4 mW, heating of the electron gas is considerable and it results in an important decrease of the global spin polarization, as well as in the magnitude of the spin filter effect. The numerical calculations, which reproduce an ideal situation where the electrons are always at $T_e = 50$ K, show again only small variations between the cases $p = 0$ and $p = 3/2$, mainly due to a higher concentration-dependence of the diffusion constant in the latter case.

## 6.10 Conclusions of this chapter

Spin-polarized transport of photo-electrons in bulk, $p^+$-GaAs was investigated in the Pauli blockade regime at $T_e = 50$ K. In contrast to usual spin diffusion processes in which the spin polarization decreases with distance traveled due to spin relaxation, images of the polarized photo-luminescence reveal a spin-filter effect in which the spin polarization *increases* during transport over the first 2 $\mu$m from 26 % to 38 %. This is shown to be a direct consequence of the Pauli Principle and the associated quantum degeneracy pressure which results in a spin-dependence of the diffusive transport, with relative differences in the spin-resolved diffusion constants as large as 50% between the two types of spins. Such effect is linear in the electronic polarization, increases with the electron concentration and decreases with increasing kinetic energy in the conduction band. The spin-averaged charge diffusion constant is also shown to be spin-dependent due to the quantum degeneracy pressure.

It is remarkable that, for the present system with strong spatial inhomogeneity of charge, spin, and temperature induced by local laser excitation, the above results have a simple explanation. Indeed, detailed theoretical modeling of spin transport and characterization of the sample have shown that the diffusion constants $D_\pm$ of spins $\pm$ are mostly determined by the spatial gradient of their Fermi levels $E_{F_\pm}$, which itself depends on the sensitivity of $E_{F_\pm}$ to the concentrations $n_\pm$ of these electrons (the so called spin stiffness $\partial E_{F_\pm}/\partial n_\pm$ ). This quantity depends on concentration and is therefore distinct for $n_+$ and $n_-$).

On the other hand, the concentration inhomogeneity is crucial for observation of the effects of the Pauli Principle. This is because the electrostatic field caused by the distinct electron and hole diffusivities (ambipolar diffusion) increases the electron concentration at the place of excitation and therefore the degree of degeneracy. Such ambipolar-induced increase of the confinement could also be obtained by increasing the excitation power, but this will inevitably increase the electron temperature and decrease the amount of degen-

eracy. In the same sample, we have not found any manifestation of the Pauli Principle using the elegant spin grating technique, where the charge and temperature are spatially homogeneous. The main reason is that effects of degeneracy on pure spin currents created in the latter technique are not amplified by ambipolar diffusion.

It is predicted that other effects could play a role under degeneracy such as spin-dependent mobility (sec.5.3.1). However, for $p^+$ GaAs, this effect is weak, based on measurements of the dependence of the scattering time on kinetic energy (sec.4.2.5), as defined by the value of $p$ in Eq.(5.21). It is anticipated that the spin-dependence of the mobility should be observable at a lower p-type doping. Another possible effect is the existence of Soret currents, which are predicted to depend on spin in degenerate conditions. However, in the present situation, this dependence does not strongly affect the polarization profile because of the relative values of charge and temperature gradients. Distinct experimental configurations should be used for separate investigation of this effect. These effects could be evidenced by adjusting the acceptor doping, the laser energy and power.

It is finally pointed out that, in what concerns spin-dependent diffusion, the effects have been observed in a regime near the onset of degeneracy, where the photoelectron concentrations are not very large with respect to the effective density of states in the conduction band. This implies that much stronger effects are expected for larger powers. While this is not possible in the present case because of heating of the electron gas, we anticipate that the use of appropriate low dimensional structures of reduced effective density of states will increase the magnitude of the effects and to possibly open the way to the realization of spin components of increased diffusion length and mobility at a temperature closer to 300 K.

## 6.10. Conclusions of this chapter

### 6.10.1 Publications and oral communications related to this chapter

PRL 111, 246601 (2013) PHYSICAL REVIEW LETTERS week ending 13 DECEMBER 2013

**Effect of Pauli Blockade on Spin-Dependent Diffusion in a Degenerate Electron Gas**

F. Cadiz,* D. Paget, and A. C. H. Rowe
*Physique de la matière condensée, Ecole Polytechnique, CNRS, 91128 Palaiseau, France*
(Received 6 September 2013; published 9 December 2013)

Spin-polarized transport of photoelectrons in bulk, $p$-type GaAs is investigated in the Pauli blockade regime. In contrast to usual spin diffusion processes in which the spin polarization decreases with distance traveled due to spin relaxation, images of the polarized photoluminescence reveal a spin-filter effect in which the spin polarization *increases* during transport over the first 2 $\mu$m from 26% to 38%. This is shown to be a direct consequence of the Pauli principle and the associated quantum degeneracy pressure which results in a spin-dependent increase in the minority carrier diffusion constants and mobilities. The central role played by the quantum degeneracy pressure is confirmed via the observation of a spin-dependent increase in the photoelectron volume and a spin-charge coupling description of this is presented.

*Proc. SPIE* 9167, Spintronics VII, 91670C (August 28, 2014); doi:10.1117/12.2060198

**From Conference Volume 9167**

Spintronics VII
Henri-Jean Drouhin; Jean-Eric Wegrowe; Manijeh Razeghi
San Diego, California, United States | August 17, 2014

# Spin-dependent transport as a consequence of Pauli blockade in a degenerate electron gas

F. Cadiz, D. Paget and A.C.H. Rowe

Physique de la matière condensée, Ecole Polytechnique, CNRS, 91128 Palaiseau, France

**ABSTRACT**

Degeneracy of a photoelectron gas is shown to strongly affect spin polarized electron transport since the Pauli principle dictates a concentration dependence of the spin stiffness and of the mobility. This causes a spin dependence of the diffusion constant $D$. A spin-dependence of $D$ as large as 50 % is measured using polarized microluminescence imaging in $p^+$ GaAs thin films, revealing a novel spin filter effect. The charge diffusion constant also depends on spin via a second order effect.

**Keywords:** Spin transport, diffusion, Polarization

## 6.10. Conclusions of this chapter

PHYSICAL REVIEW B **91**, 165203 (2015)

### Effect of the Pauli principle on photoelectron spin transport in $p^+$ GaAs

F. Cadiz,[1] D. Paget,[1] A. C. H. Rowe,[1] T. Amand,[2] P. Barate,[2] and S. Arscott[3]
[1]*Physique de la Matière Condensée, Ecole Polytechnique, CNRS, 91128 Palaiseau, France*
[2]*Université de Toulouse, INSA-CNRS-UPS, 31077 Toulouse Cedex, France*
[3]*Institut d'Electronique, de Microélectronique, et de Nanotechnologie (IEMN), Université de Lille, CNRS, Avenue Poincaré, Cité Scientifique, 59652 Villeneuve d'Ascq, France*
(Received 25 February 2015; revised manuscript received 7 April 2015; published 17 April 2015)

In $p^+$ GaAs thin films, the effect of photoelectron degeneracy on spin transport is investigated theoretically and experimentally by imaging the spin polarization profile as a function of distance from a tightly focused light excitation spot. Under degeneracy of the electron gas (high concentration, low temperature), a dip at the center of the polarization profile appears with a polarization maximum at a distance of about 2 $\mu$m from the center. This counterintuitive result reveals that photoelectron diffusion depends on spin, as a direct consequence of the Pauli principle. This causes a concentration dependence of the spin stiffness while the spin dependence of the mobility is found to be weak in doped material. The various effects which can modify spin transport in a degenerate electron gas under local laser excitation are considered. A comparison of the data with a numerical solution of the coupled diffusion equations reveals that ambipolar coupling with holes increases the steady-state photoelectron density at the excitation spot and therefore the amplitude of the degeneracy-induced polarization dip. Thermoelectric currents are predicted to depend on spin under degeneracy (spin Soret currents), but these currents are negligible except at very high excitation power where they play a relatively small role. Coulomb spin drag and band-gap renormalization are negligible due to electrostatic screening by the hole gas.


**SPINTECH VII - Poster Presentations (BY LAST NAME)**

Poster Sessions will be held in the Renaissance Ballroom on the 5th floor of the Hotel Intercontinental Chicago

| | | | | | |
|---|---|---|---|---|---|
| J19 | Paget | Daniel | Ecole Polytechnique, Palaiseau, France | The effect of Pauli blockade on spin-dependent diffusion in degenerate semiconductors | 31-Jul |

SPIE. OPTICS+ PHOTONICS

CONNECTING MINDS. ADVANCING LIGHT.

San Diego Convention Center
San Diego, California, USA

**CONFERENCE 9167**

LOCATION: CONV. CTR. ROOM 15A AND CONV. CTR. ROOM 14B

Sunday–Thursday 17–21 August 2014 • Proceedings of SPIE Vol. 9167

# Spintronics VII

12:00 pm: **Spin-dependent transport as a consequence of Pauli blockade in a degenerate electron gas** *(Invited Paper)*, Fabian Cadiz, Daniel Paget, Alistair Rowe, Ecole Polytechnique (France). . . . . [9167-11]

Lunch Break . . . . . Sun 12:30 pm to 1:30 pm

## 6.10. Conclusions of this chapter


Spin/charge coupled transport in GaAs in the Pauli blockade regime

Fabian Cadiz, Daniel Paget, Alistair Rowe [1, @]

1 : Physique de la matière condensée
*Ecole Polytechnique, CNRS : UMR7643*
*Route de Saclay, 91128 Palaiseau - France*

## 6.10. Conclusions of this chapter

# Chapter 7

# Conclusion and future work

The effect of the Pauli principle on spin tranport has been investigated by using a novel luminescence microscopy technique. Spin-polarized electrons are created at $r = 0$ by a tightly-focused, circularly-polarized CW laser excitation. At 15 K and high excitation power, the spatially resolved spin polarization exhibits a volcano-like shape, with a counter-intuitive crater at the centre (Fig.6.1). The explanation is that the electron gas becomes degenerate and that, because of the Pauli principle, the spin diffusivity for majority spins $D_+$ is larger than for minority ones $D_-$, we estimate $D_+/D_- \approx 1.4$. In the same conditions, the exclusion principle also causes a charge-spin coupling, due to which the electronic concentration depends on their spin. By changing the laser polarization from circular to linear, a spin-dependent increase of the volume of the photo-electron population is observed (Fig.6.4), which is a rather weak effect since it is to second order in the electronic polarization. This consequence of the quantum degeneracy pressure is also observed in degenerate atom traps. Photohall effect measurements suggests that the mobility is only weakly spin-dependent, so most of the observed effect comes from a spin-dependent spin stiffness $S_\pm = \partial E_{F_\pm}/\partial n_\pm$.

The effect of degeneracy on the main phenomena relevant for spin transport in semiconductors is so far almost completely unknown. Besides spin-dependent diffusion and charge-spin coupling, the Pauli principle is predicted to affect spin transport in several ways (spin-dependent mobility, spin Soret currents, bandgap renormalization, etc). None of these novel effects have been demonstrated so far, and the present work opens perspectives for investigating them.

## 7.1 Importance of an inhomogeneous photoelectron concentration

The local gradient of electron temperature induced by light excitation is too weak to induce observable thermoelectric currents (Soret currents) but, under degeneracy, these currents are predicted to become spin-dependent. Since the spatial concentration inhomogeneity induced by local laser excitation is crucial for the observation of this phenomena, it is proposed to continue the exploration with the microscopy technique used so far. Moreover, the electrostatic field caused by the distinct electron and hole diffusivities (ambipolar diffusion) increases the electron concentration at $r = 0$ and therefore the degree of degeneracy. No manifestation of the Pauli principle has been observed using the transient spin grating technique, where the charge and the temperature are spatially homogeneous, and where the optically imprinted spin wave relaxes in time scales shorter than the time required for the electron gas to cool down, as suggested by time-resolved photoluminescence measurements.

## 7.2 Changing the hole concentration

The strong p-doping of the sample used in this work is crucial since it results in screening of the various electron-electron interactions by the prescence of the majority holes. This is also responsible for a weak spin-dependence of the electron mobility. Lower dimensional systems seem therefore promising since Coulomb screening is less efficient than in bulk material (Chazalviel (1999)). In addition, the concentration of free holes can be electrically controlled, for example in a $p^+$-AlGaAs/n-GaAs heterostructure, in which the hole concentration in the n-GaAs region can be adjusted by an applied voltage. This may be used to study the spin-dependence of the mobility if the diffusion length in the p-region is much smaller than in the n-region.

It was shown in sec.6.9 that, for a spatially inhomogeneous photoelectron density at high

concentration, the mobility is dominated by ambipolar Coupling with holes regardless of the possible spin-dependence of the mobility. A way to avoid this problem is to perform photoHall measurements under a uniform laser excitation whose degree of circular polarization is modulated at a frequency $f$. Variations in the photoHall voltage with a frequency $f$ will be a signal of a spin-dependent mobility.

## 7.3 The Pauli principle in confined systems.

It would be of great interest to explore the effect of Pauli blockade in lower dimensional systems since quantum confinement can increase $|\mathscr{P}_i|$ to $\sim$ 100 % while the density of states is smaller and less sensitive to changes in temperature ($N_c^{\mathcal{D}} \propto T_e^{\mathcal{D}/2}$, where $\mathcal{D} = 1, 2, 3$ is the dimensionality of the system). In this case, the effects of Pauli blockade should persist to higher temperatures. This may open the way to the exploitation of Pauli blockade driven spin-filter and coupling effects in room temperature semiconductor spintronic devices.

As an example, in a two-dimensional electron gas (2DEG) confined in a quantum well, Pauli blockade effects could be much larger than in our bulk p-GaAs sample. Indeed, a concentration of $n_0$ electrons in a bulk sample, when confined to a quantum well of thickness $d_{\mathrm{qw}}$, will have a two-dimensional density of $n_0^{2D} = n_0 d_{\mathrm{qw}}$. The density of states of a 2-D gas is given by $N_c^{2D} = m^* k_B T_e/(\pi\hbar^2)$, whereas for a three dimensional electron gas at the same temperature, $N_c^{3D} = 2(m^* k_B T_e/(2\pi\hbar^2))^{3/2}$. The relative degree of degeneracy when the electrons are confined in quantum well with respect to the bulk is therefore given by:

$$\frac{n_0^{2D}/N_c^{2D}}{n_0/N_c^{3D}} = d_{\mathrm{qw}}\sqrt{\frac{m^* k_B T_e}{2\pi\hbar^2}} \tag{7.1}$$

For GaAs, this ratio is 176.5 at room temperature and about 73 at $T_e = 50$ K, so that for a fixed number of photoelectrons, the degree of degeneracy is increased by 2 orders of magnitude in a quantum well. Moreover, in the degenerate regime, the reduced spin stiffness (see Eq.(5.17)) varies as $n^{2/3}$ in the bulk whereas in 2 dimensions it is proportional to $n$.

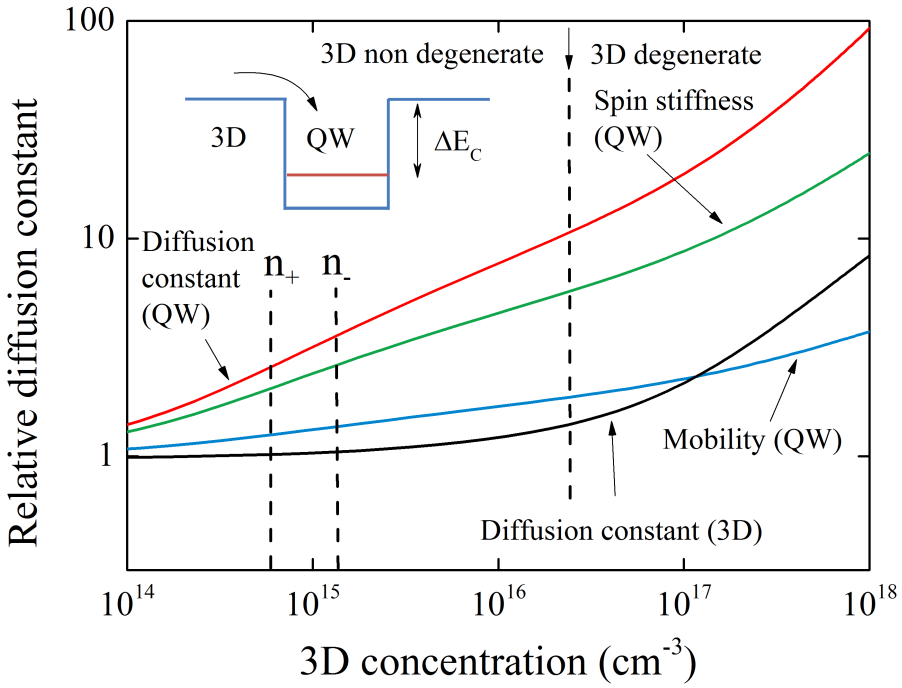


**Figure 7.1:** Creation of degenerate electrons in a QW by a low power injection from a 3D region. Here one has extended the equations of Chapter 5 and one has taken $\Delta E_c = 20$ meV, $T_e = 50$ K and $p$=0 (in the bulk). This figure shows as a function of concentration in the 3D zone, the diffusion constant, the spin stiffness and the mobility in the QW. Also shown for comparison (dotted line) is the concentration dependence of the diffusion constant in the 3D zone. While degeneracy in the 3D zone starts near $10^{16}$ cm$^{-3}$, it appears in the QW for concentrations at least two orders of magnitud smaller .

This is demonstrated by a more rigourous calculation in which photoelectrons created in the barrier are supposed to be in equilibrium with the quantum well, and the results for a well of depth 20 meV are shown in Fig.7.1 which shows the relative diffusivity in the QW as a function of the electronic concentration in the 3D layer. One sees that:

i) with respect to 3D diffusion, the concentration dependence of the diffusion constant in the QW is strongly enhanced and occurs for electronic concentrations in the 3D region which are reduced by about 2 orders of magnitude. As an example, for $n = 2 \times 10^{15}$ cm$^{-3}$ electrons of polarization $\mathscr{P} = 40$ % in the bulk (see dotted lines of Fig.7.1), the ratio of the diffusion constants of spins + and − in the QW is about 1.4 and a volcano-like spatial profile of the spin polarization, similar to that of Fig.6.1, will be obtained.

ii) Even if $p = 0$ (see Eq.(5.21)), the mobility now depends on concentration and therefore on spin because of the specific 2D density of states (Kainz and Rossler (2004)) and because screening is less efficient in 2D systems, according to Chazalviel (1999). Again, for $n = 2 \times 10^{15}$ cm$^{-3}$ and $P = 40$ %, one has $(\mu_+ - \mu_-)/\langle\mu\rangle \approx 10$ %, which should be easily revealed by photohall measurements under defocussed excitation in a Hall bar established on the QW. These effects should be further increased by adjusting the hole concentration in the QW in order to increase $p$.

Resonant light excitation between levels of the QW is also interesting since, because of the splitting between the heavy and light excitons, the hole spin relaxation time is strongly increased, so that circularly-polarized light will create spin-polarized holes. At sufficiently high excitation power, photocreated holes will be more numerous than dark holes and the hole gas will become spin-polarized. In this case, their spin diffusion will be revealed from the images. Under resonant excitation, it will be highly interesting to investigate the diffusion of degenerate spin-polarized hole gases.

Finally, it would be of great interest to explore spin diffusion in the ultimate 2D semiconductor case, for example by using monolayer group VI transition metal dichalgogenides, where screening is negligible and gating can be used to switch between bosonic and fermionic particles (Ross et al. (2013)). Their different spin-statistics should give rise to a dramatically different behaviour of spin diffusion in the degenerate regime.

## 7.4 The effect of Pauli principle on the Spin Hall Effect.

When an electric field $E_x$ is applied along the $x$-direction in a semiconductor, a transverse spin current $J^z_{s,y}$ appears due to the spin Hall Effect, where $z$ is the quantization axis of the spin, normal to the plane where the current flows. When the SHE is dominated by extrinsic contributions of side jump and skew scattering, one has

$$J^z_{s,y} = [\sigma^{ss} + \sigma^{sj}]E_x$$

where the skew-scattering contribution is given by $\sigma^{ss} = \frac{\tau_m}{\tau_{ss}}\sigma^D$, and where $\sigma_D = (nq^2\tau_m/m^*)$ is the drude conductivity. The skew-scattering time $\tau_{ss}$ is proportional to $\tau_m$ and typically $\tau_{ss}/\tau_m \sim 10^3$ [Hankiewicz and Vignale (2009)]. The side jump term is given by $\sigma^{sj} = -2\alpha m^* q^2$, where $\alpha$ is the spin orbit interaction strength. It can be seen that the side jump term does not depend on the momentum scattering time $\tau_m$. In contrast, the skew scattering contribution to the spin conductivity scales with transport scattering time. Therefore, it is expected that in the degenerate regime, the Pauli principle modifies the skew scattering conductivity, while the side jump conductivity, which is independent of $\tau_m$, remains completely unaffected. This provides a method for distinguishing between different types of spin Hall conductivity.

Note that under degeneracy, the spin relaxation time should increase due to Pauli blockade, as observed by Amo et al. (2007), and so this should also modify the spatial dependence of the spin accumulation at the edges of the Hall bar due to the SHE.

# Chapter 8

# Appendix

## 8.1 The mathematics of diffusion

In this section, the solution of the time-independent diffusion equation is discussed. Let's consider a sample where an inhomogeneous concentration $n$ may exist, with lifetime $\tau$ and diffusion constant $D$. The diffusion equation, often named Helmholtz equation, is given by:

$$g = \left(\frac{1}{\tau} - D\Delta\right) n \tag{8.1}$$

where $g$ is the creation rate of the quantity $n$. The boundary condition imposed at any point of the sample surface is given by:

$$[-D\vec{\nabla}n] \cdot \vec{e}_n = Sn \tag{8.2}$$

where $\vec{e}_n$ is the normal to the surface and where $S$ is the surface recombination velocity.

Note that if a uniform electric field $E$ is applied along the $x$-direction, Eq.(8.1) should be replaced by the more general drift-diffusion equation:

$$g = \left(\frac{1}{\tau} - \mu E\frac{\partial}{\partial x} - D\Delta\right) n \tag{8.3}$$

where $\mu$ is the mobility. The corresponding generalization of the boundary condition (8.2)

is given by

$$[-D\vec{\nabla}n - \mu n\vec{E}] \cdot \vec{e}_n = Sn \tag{8.4}$$

Whereas the drift-diffusion equation (8.3) represent a more general situation, Eq.(8.1) is completely general (provided that the mobility and diffusion constant are spatially independent) in the sense that the drift term in Eq.(8.3)can be eliminated if one writes the solution in the form $n = pe^{\alpha x}$. Indeed, replacing in Eq.(8.3), it can be shown that if $\alpha = -(\mu E\tau)/(2L^2)$, then $p$ satisfies an equation equivalent to Eq.(8.1):

$$g\frac{D_{\text{eff}}}{D} = \left(\frac{1}{\tau} - D_{\text{eff}}\Delta\right)p \tag{8.5}$$

with an effective diffusion constant given by:

$$D_{\text{eff}} = \frac{D}{1 + \frac{(\mu E)^2\tau}{4D}}. \tag{8.6}$$

with the same boundary condition given by (8.2). In consequence, any drift-diffusion equation with a uniform electric field is reduced to a pure diffusion equation of the form of Eq.(8.1). Note finally that Eq.(8.1) has the structure of an inhomogeneous Helmholtz equation, for which an isotropic Green function exists in two-dimensions with $n(r) \to 0$ as $r \to \infty$, and is given by:

$$n(r) \approx K_0[\frac{r}{L}] \tag{8.7}$$

where $K_0$ is a modified Bessel function of the second kind, $r$ is the radial coordinate and $L = \sqrt{D\tau}$ is the diffusion length. The complete solution for the two-dimensional case with a radially symmetrical creation function $g = g(r)$ can be written as:

$$n = \int_0^\infty K_0[\frac{r'}{L}]g(r - r')dr' \tag{8.8}$$

In three dimensions, there is no such analytical solution. However, as it will be shown below, in the case of a sample of thickness $d$ with infinte lateral dimensions and radially symmetrical excitation, the solution may be either written as a series expansion of spatial modes, or written in an integral form, the latter being an original result of this work.

### 8.1.1 Approximation by spatial modes

Here, we consider the diffusion equation in a sample of thickness $d$, with front and back surfaces corresponding to $z = 0$ and $z = d$, respectively, and a radially symmetrical excitation $g(r,z) = g_0 e^{-r^2/\omega^2} e^{-\alpha z}$. Eq.(8.1) is rewritten here

$$g(r,z) = \left(\frac{1}{\tau} - D\Delta\right) n(r,z)$$

where the boundary condition of Eq.(8.2) corresponds to $(Sn - D\partial n/\partial z)|_{z=0} = 0$ and $(S'n + D\partial n/\partial z)|_{z=d} = 0$. This equation is not separable, i.e., its solution cannot be expressed as a product of a function of $r$ and of a function of $z$. It will be shown here, however, that $n$ can be developed on a basis of separable functions. First, we find the eigenfunctions of the Laplace operator (Carlslaw and Jaeger (1966)):

$$\frac{d^2}{d^z} u_m(z) + \lambda_m u_m(z) = 0 \tag{8.9}$$

satisfying the same boundary conditions as Eq.(8.2). They are given by

$$u_m(z) = \beta_m[\sin(\alpha_m z/d) + \alpha_m/\gamma \cos(\alpha_m z/d)] \tag{8.10}$$

where $\lambda_m = \alpha_m^2/d$, $\gamma = Sd/D$ and where $\alpha_m$ is the solution of the non-linear equation:

$$\tan(\alpha_m) = \frac{\alpha_m(\gamma + \gamma')}{\alpha_m^2 - \gamma\gamma'} \tag{8.11}$$

with $\gamma' = S'd/D$. Eq.(8.11) has a countable set of solutions, with $\alpha_m \in [(m-1)\pi, m\pi]$ where $m$ is a natural number, and defines a set $\{u_m\}$ of orthogonal functions. The normalization constant $\beta_m$ is chosen such that $\{u_m\}$ forms an orthonormal set, i.e., $\int_0^d u_m(z) u'_m(z) dz = \delta_{mn}$, where $\delta_{ij}$ is the Kronecker symbol, and is given by:

$$\frac{1}{\beta_m^2} = \frac{d}{2}[1 - \frac{\sin 2\alpha_m}{2\alpha_m} + \frac{1 - \cos 2\alpha_m}{\gamma} + \frac{\alpha_m^2}{\gamma^2}(1 + \frac{\sin 2\alpha_m}{2\alpha_m})] \tag{8.12}$$

The solution of Eq.(8.1) can be expanded as:

$$n(r,z) = \sum_m f_m(r) u_m(z) \tag{8.13}$$

This gives, together with Eq.(8.9):

$$g(r,z) = \frac{1}{\tau}\sum_m f_m(r)u_m(z) - D\sum_m \frac{u_m(z)}{r}\frac{\partial}{\partial r}(r f_m(r)) + D\frac{\alpha_m^2}{d^2}\sum_m f_m(r)u_m(z)$$

Since the functions $\{u_m\}$ form an orthonormal set in the interval $[0,d]$, one can multiply by $u'_m$ and integrate over $z$ to obtain:

$$\int_0^d g(r,z)u_m(z)dz = \frac{f_m}{\tau_m} - D\frac{1}{r}\frac{\partial}{\partial r}(r\frac{\partial f_m}{\partial r}) \tag{8.14}$$

where we have defined an effective lifetime for the mode of order $m$:

$$1/\tau_m = 1/\tau + D\alpha_m^2/d^2. \tag{8.15}$$

Eq.(8.14) shows that the radial function $f_m(r)$ satisfies a one-dimensional Helmholtz equation with a diffusion length $L_m = \sqrt{D\tau_m}$ and excitation function $\int_0^d g(r,z)u_m(z)dz$. According to Eq.(8.8), the spatial mode of order $m$ is proportional to the modified Bessel function of the second kind $K_0$ convoluted with the excitation profile and decays as a function of $r$ with a characteristic distance $L_m = \sqrt{D\tau_m}$ :

$$f_m(r) = \int_0^\infty K_0[r'/\sqrt{D\tau_m}][\int_0^d g(r-r',z)u_m(z)dz]dr'. \tag{8.16}$$

Considering a gaussian excitation profile of the form $g(r,z) = g_0 e^{-r^2/\omega^2}e^{-\alpha z}$, then the expansion of Eq.(8.13) reads:

$$n(r,z) = g_0\sum_m c_m u_m(z)\int_0^\infty K_0[r'/L_m]e^{(r-r')^2/\omega^2}dr' \tag{8.17}$$

where $c_m$ are the Fourier coefficients corresponding to the expansion of the function $e^{-\alpha z}$ in the basis $\{u_m\}$:

$$c_m = \int_0^d e^{-\alpha z}u_m(z)dz \tag{8.18}$$

Fig.8.1 shows the approximated solution of Eq.(8.1) by considering the first 10 modes of the expansion in Eq.(8.17) for different values of the surface recombination velocities

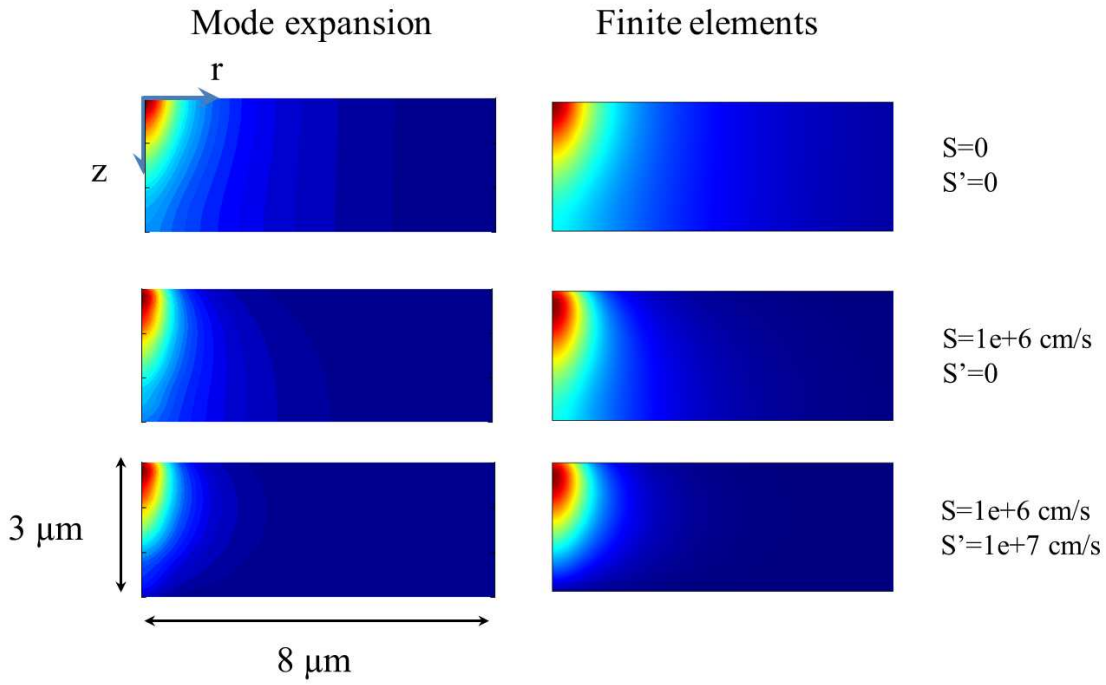


**Figure 8.1:** Left: First 10 mode expansion given by Eq.(8.17) for different values of the front and back surface recombination velocities, $S$ and $S'$, respectively. The diffusion length is $L = 4.6$ $\mu$m, the excitation is a Gaussian function with radius $\omega = 0.5$ $\mu$m and the absorption length is $\alpha^{-1} = 1$ $\mu$m. Right: solution obtained using a finite element implementation of Eq.(8.1), with the same parameters used in the left panel.

$S$ and $S'$. Also shown is a numerical resolution of Eq.(8.1) obtained by using a finite elements commercial package. The fixed numerical parameters are $D = 82$ cm$^2/s$ and $\tau = 26$ ns, $d = 3$ $\mu$m, $\omega = 0.5$ $\mu$m and $\alpha = 1$ $\mu$m$^{-1}$.

Note that an approximation of the exact solution requires a considerable number of modes since, according to Eq.(8.18),an exponential function will have a rich decomposition in terms of the basis $\{u_m\}$. However, since $L_m$ is a decreasing function of $m$, far from the excitation the concentration $n$ has a radial dependence dominated by $K_0(r/L_1)$, which decays with an effective diffusion length given by $L_1 = \sqrt{D\tau_1}$, where $\tau_1$ is the lifetime given by Eq.(8.15), which we explicity reproduce here

$$1/\tau_1 = 1/\tau + \frac{D\alpha_1^2}{d^2}$$

with $\alpha_1$ given by Eq.(8.11). This is confirmed in Fig.8.2, in which the black curves

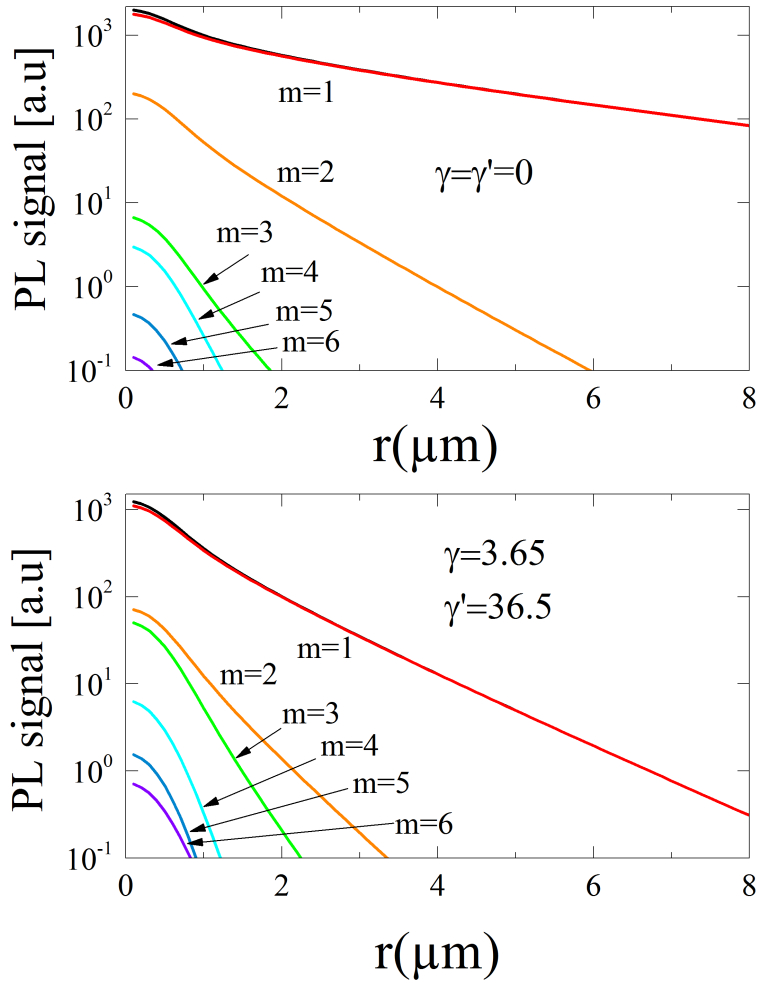


**Figure 8.2:** Total luminescence signal, as given by Eq.(8.19), and its decomposition in modes. The top panel corresponds to the case $S = S' = 0$, whereas the bottom panel corresponds to $S = 10^6$ cm/s and $S' = 10^7$ cm/s. In both cases, the modes of order $m > 1$ are negligible for sufficiently large $r$.

represent the PL signal (averaged over depth, as given by Eq.(3.3) ) :

$$n(r) = g_0 \left( \int_0^d \sum_m c_m u_m(z) e^{-\alpha_l z} \right) \int_0^\infty K_0[r'/L_m] e^{(r-r')^2/\omega^2} dr' \tag{8.19}$$

with $\alpha_l = 1/3\ \mu\text{m}^{-1}$, for the case $S = S' = 0$ (top) and $S = 10^6$ cm/s, $S' = 10^7$ cm/s (bottom). The first six modes in Eq.(8.19) are also shown separately. It can be seen that, except for very small values of $r$, the total signal is mainly given by the first mode of the expansion. Large surface recombination velocities give more relative weight to higher order modes near $r = 0$, but their influence on the total PL signal decreases rapidly as a function of $r$. This justifies fitting the experimental curves with only one mode.

### 8.1.2 Exact solution in an integral form

The mode expansion discussed in Eq.(8.1.1) requires many modes in order to reproduce the $z$-dependence of the concentration $n$. In this section we express the solution of the time-independent diffusion equation [Eq.(8.1)] in an integral form which can be easily evaluated numerically. The general solution is obtained by calculating the Green's function $G(r,z)$, which is the response to a Dirac excitation at the point $r=0$, $z=z'$, that satisfies the same boundary conditions as $n$ [Eq.(8.2)]. By using a similar approach as Duran et al. (2005), the in-plane Fourier transform $\hat{G}(\xi,z)$ of $G(r,z)$ satisfies an ordinary differential equation with respect to $z$:

$$-\frac{\tau}{2\pi L^2}\delta(z-z') = \frac{\partial^2\hat{G}(\xi,z-z')}{\partial z^2} - \kappa^2\hat{G}(\xi,z-z') \tag{8.20}$$

where $\kappa=\sqrt{1/L^2+\xi^2}$. By imposing the boundary conditions, the solution of Eq.(8.20) is:

$$\begin{aligned}\hat{G}(\xi,z-z') = \frac{\tau}{4\pi L^2\kappa}\Bigg[&e^{-\kappa|z-z'|} + \frac{\kappa-\frac{S}{D}}{\kappa+\frac{S}{D}}e^{-\kappa(z+z')} \\ &+\frac{2(\kappa-\frac{S'}{D})(\kappa\cosh\kappa z+\frac{S}{D}\sinh\kappa z)(\kappa\cosh\kappa z'+\frac{S}{D}\sinh\kappa z')}{e^{\kappa d}(\kappa+\frac{S}{D})[(\frac{SS'}{D^2}+\kappa^2)\sinh\kappa d+\kappa\frac{S+S'}{D}\cosh\kappa d]}\Bigg]\end{aligned} \tag{8.21}$$

The photoelectron concentration is then given by the following convolution:

$$n(r,z) = 2\pi\int_0^d e^{-\alpha z'}\Big[\int_0^\infty r' G(r-r',z-z')\varphi(r')dr'\Big]dz' \tag{8.22}$$

which can be rewritten as:

$$\boxed{n(r,z) = 2\pi\int_0^\infty \xi\hat{\varphi}(\xi)J_0(\xi r)d\xi\int_0^d e^{-\alpha z'}\hat{G}(\xi,z-z')dz'} \tag{8.23}$$

where $\hat{\varphi}(\xi)$ is the Fourier transform of $\varphi(r)$, and $J_0(\xi r)$ is a Bessel function of the first kind. For a Gaussian excitation profile of radius $\omega$, $\hat{\varphi}(\xi)\propto e^{-\xi^2\omega^2/4}$. The validity of Eq.(8.23) can be tested numerically, as can be seen in Fig.8.3, or by comparing it with well known solutions for simple cases. As an example, neglecting surface recombination ($S+S'=0$) and considering a line Dirac excitation $g=\delta(r)$(independent of $z$), Eq.(8.23)

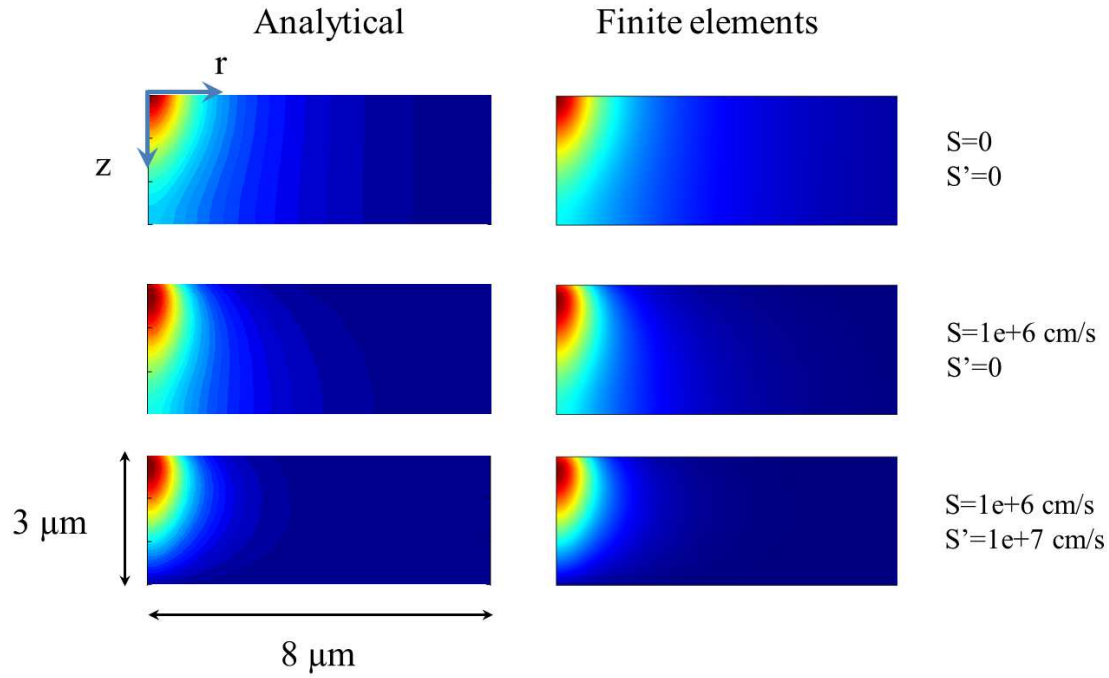


**Figure 8.3:** Left: solution of the diffusion equation given by the integral form of Eq.(8.23) for different values of the front and back surface recombination velocities, $S$ and $S'$, respectively. The diffusion length is $L = 4.6$ $\mu$m, the excitation is a Gaussian function with radius $\omega = 0.5$ $\mu$m and the absorption length is $\alpha^{-1} = 1$ $\mu$m. Right: solution obtained using a finite element implementation of Eq.(8.1), with the same parameters used in the left panel.

becomes

$$n(r,z) \propto \int_0^\infty \xi \frac{J_0(\xi r)}{1+(L\xi)^2} d\xi = \frac{1}{L^2}\int_0^\infty \frac{u}{1+u^2} J_0(ur/L)du$$

By using Mehler's Bessel function formula, $J_0(x) = 2/\pi \int_0^\infty \sin(x\cosh t)dt$ and Cauchy's residue theorem, it can be shown that:

$$n(r,z) \propto \int_0^t [\int_0^\infty \frac{u}{1+u^2}\sin(ur/L\cosh t)du]dt \propto \int_0^t e^{-r/L\cosh t}dt = K_0[r/L]$$

so that Eq.(8.23) reduces to the modified Bessel function of the second kind $n(r,z) \propto K_0(r/L)$ for $r > 0$, which is the known Green function for planar diffusion [Eq.(8.8)].

In the limit of a very thin sample ($d \to 0$) and with a passivated rear surface ($S' = 0$),

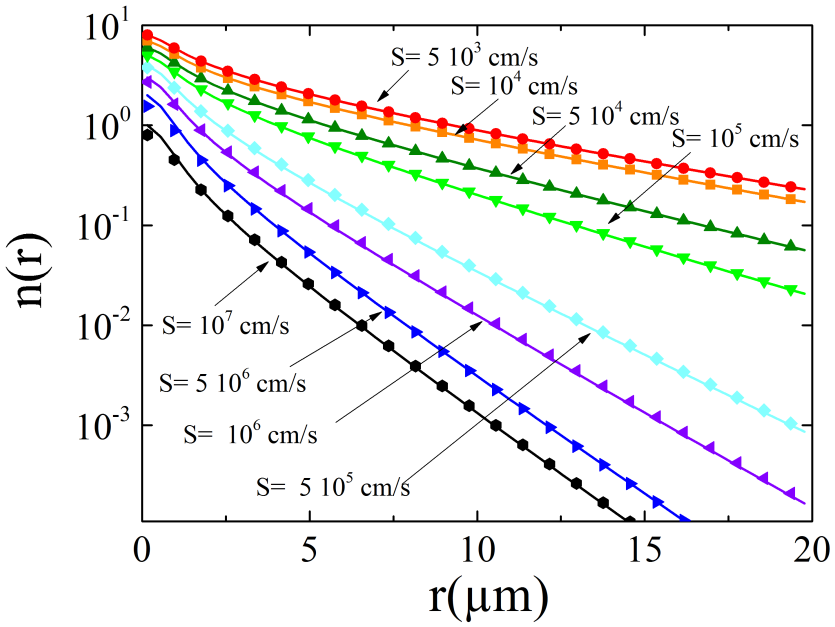


**Figure 8.4:** Lines are solutions of the diffusion equation given by Eq.(8.23) for a fixed diffusion length $L$ and for different values of the surface recombination velocity $S$. Symbols represent the solution obtained when $S = 0$ and where the diffusion length is replaced by an effective value given by Eq.(8.26), which takes into account surface recombination.

one finds:

$$G(\xi) \propto \frac{1}{\kappa^2 + \frac{S^2}{D^2}} = \frac{1}{1/L^2 + S^2/D^2 + \xi^2} \tag{8.24}$$

so it is equivalent to replace the sample by a passivated sample ($S = 0$) with an effective diffusion length given by

$$\frac{1}{L_{\text{eff}}^2} = \frac{1}{L^2} + \frac{S^2}{D^2} \tag{8.25}$$

which corresponds indeed to the solution of Eq.(8.11) for $\alpha_m << 1$, which gives an effective lifetime, according to Eq.(8.15), such that $L_{\text{eff}} = \sqrt{D\tau_{\text{eff}}}$. The latter result is a good approximation even for the case of finite thickness. The solid lines in Fig.8.4 are the solution of the diffusion equation given by Eq.(8.23) with $d = 3$ $\mu$m, $L = 10$ $\mu$m and a variable surface recombination velocity $S$ at the front surface. An average in the $z$ direction is performed.

The symbols in Fig.8.4 represent the solution given by Eq.(8.23) when taking $S = 0$ and where the diffusion length is now replaced by its effective value, given by the generalization

of Eq.(8.25) for an arbitrary thickness $d$:

$$\frac{1}{L_{\text{eff}}^2} = \frac{1}{L^2} + \alpha^2 \tag{8.26}$$

where $\alpha$ is given by $\alpha d \tan(\alpha d) = Sd/D$, which is a particular case of Eq.(8.11) for $S' = 0$ and $m = 1$. It is seen from Fig.8.4 that the agreement between the two approaches is excellent for all values of $S$ as long as $r > d$.

### 8.1.3 Solution of the time-dependent diffusion equation.

Here, we consider the time-dependent diffusion equation for an homogeneous excitation ($\omega \to \infty$), for which the solution $n$ will only depend on time and depth:

$$g(z,t) = \left(\frac{\partial}{\partial t} + \frac{1}{\tau} - D\Delta\right) n(z,t) \tag{8.27}$$

with boundary conditions given by Eq.(8.2), which we reproduce here: $D\partial n/\partial z|_{z=0} = Sn(0)$ and $D\partial n/\partial z|_{z=d} = -S'n(d)$. For the solution of the time-dependent diffusion equation we first neglect hot electron effects so that thermalization is considered to be instantaneous. We thus assume that $g(z,t) = g_0\delta(t)e^{-\alpha z}$ in Eq. (8.27) and we search for a linear combination of $u_m(z)$ with time-dependent coefficients, $n(z,t) = \sum_m a_m(t)u_m(z)$, were $u_m$ are the eigenfunctions of the Laplace operator defined in Eq.(8.10). Replacing the latter expansion in Eq.(8.27), and using the orthogonality of the set $\{u_m(z)\}$, we find that the general solution of the diffusion equation is written:

$$n(z,t) = \sum_m a_m u_m(z) e^{-t/\tau_m} \tag{8.28}$$

where the characteristic times $\tau_m$ of the various modes are those given by Eq.(8.15)

$$1/\tau_m = 1/\tau + D\alpha_m^2/d^2$$

The expression for $a_m$ is found by imposing that at $t = 0$, $n(z,0) = n_0 e^{-\alpha z}$. This gives $a_m = n_0 c_m$, where $c_m$ are the coefficients defined in Eq.(8.18). The total luminescence intensity is finally given by:

$$I_{\mathrm{TRPL}}(t) = K \int_0^d e^{-\alpha_l z} \sum_m c_m e^{-t/\tau_m} u_m(z) dz$$

where $\alpha_l$ is the absorption coefficient at the luminescence energy, and $K$ is a constant. Finally, the intensity can be written

$$\boxed{I_{\mathrm{TRPL}}(t) = K \sum_m d_m e^{-t/\tau_m}} \tag{8.29}$$

where

$$d_m = \beta_m^2 A_m(\alpha) A_m(\alpha_l) \tag{8.30}$$

and

$$\begin{aligned} A_m(x) =& [x^2 + (\alpha_m/d)^2]^{-1} \{\alpha_m (1/d + x/\gamma) \\ & - e^{xd} \left[ \alpha_m \cos(\alpha_m) [\frac{1}{d} + \frac{x}{\gamma}] + \sin(\alpha_m) [x - \frac{\alpha_m^2}{\gamma d}] \right] \} \end{aligned} \tag{8.31}$$

It is seen from the form of $\beta_m$ [Eq.(8.12)] and $A_m(x)$ that the coefficients $d_m$ only depend on $\gamma$, $\gamma'$ and $d$. In the special case where $\gamma' = 0$, the amplitudes $d_m$ are given in Fig.8.5, from which it is seen that for a passivated surface for which $\gamma = 0$ only one mode is present in the transient, with characteristic lifetime equal to the bulk lifetime $\tau$. In contrast, the use of a naturally oxidized sample guaranties that $\gamma$ is not very small, so that more than one mode is observed in the transient.

If one considers that thermalization of photocarriers after creation occurs in a time $\tau_0$ which can be comparable with the times $\tau_m$ above, Eq.(8.29) should be replaced by

$$I_{\mathrm{TRPL}}(t) = K \sum_m \frac{d_m}{1/\tau_m - 1/\tau_0} [e^{-t/\tau_m} - e^{-t/\tau_0}] \tag{8.32}$$

if one assumes that the spatial distribution is unchanged during thermalization.

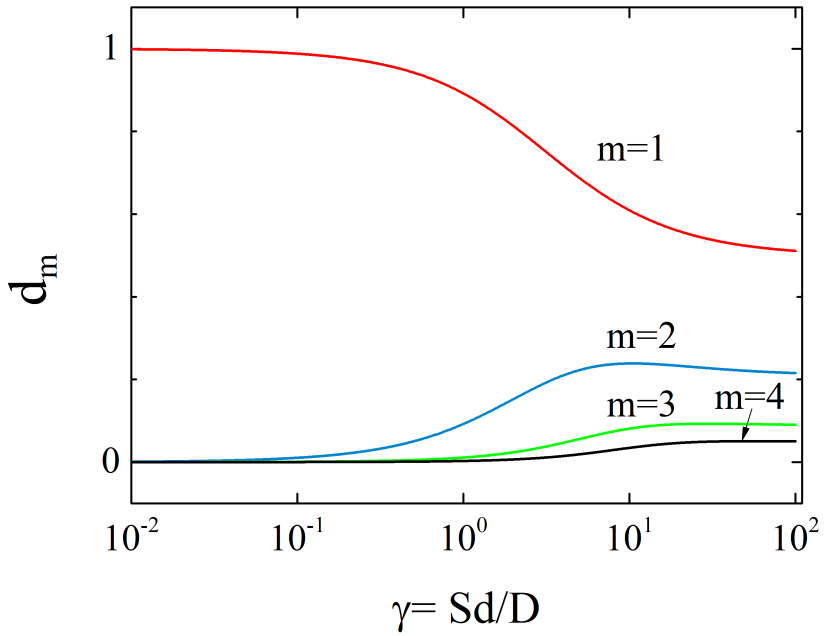


**Figure 8.5:** Values of the amplitudes $d_m$ calculated using Eq. (8.30) and neglecting photoluminescence reabsorption as well as the recombination at the back surface.

### 8.1.4 Ambipolar drift-diffusion equations in the non-degenerate regime

In a p-doped sample, the charge density is coupled to the photohole density via the Coulomb interaction. Therefore, a set of coupled differential equations must be solved. For the charge density, and in the absence of any charge-spin coupling mechanism:

$$g - K(N_A + \delta p)n + \vec{\nabla} \cdot [\mu_e n \vec{E} + D_e \vec{\nabla} n] = 0 \tag{8.33}$$

where $K$ is the bimolecular recombination coefficient, $N_A$ is the acceptor concentration,$\vec{E}$ is the electric field and $\delta p$ is the hole density created by light, who satisfies the following equation:

$$g - K(N_A + \delta p)n + \vec{\nabla} \cdot [-\mu_h (N_A^- + \delta p)\vec{E} + D_h \vec{\nabla} \delta p] = 0 \tag{8.34}$$

where $N_A^-$ is the concentration of ionized acceptors. The electric field depends on $n$ and $\delta p$ via Poisson's equation:

$$\vec{\nabla} \cdot E = q(\delta p - n)/(\epsilon \epsilon_0) \tag{8.35}$$

Equations (8.33),(8.34) and (8.35) may be reduced to only one, taking an effective diffusion constant and mobility for the electronic density. By taking the difference between Eq.(8.33) and Eq.(8.34), one obtains:

$$\vec{\nabla}\cdot[(n\mu_e+(N_A^-+\delta p)\mu_h)\vec{E}]=\vec{\nabla}\cdot[D_h\vec{\nabla}\delta p-D_e\vec{\nabla}n] \tag{8.36}$$

A solution of this equation, neglecting derivatives in the $z$ direction, and imposing a constant value $\vec{E}^{\text{ext}}$ for the electric field at infinity is given by:

$$\vec{E}=\frac{D_h\vec{\nabla}\delta p-D_e\vec{\nabla}n}{n\mu_e+(N_A^-+\delta p)\mu_h}+\frac{\mu_h N_A^-}{n\mu_e+(N_A^-+\delta p)\mu_h}\vec{E}^{\text{ext}} \tag{8.37}$$

Replacing Eq.(8.37) in Eq.(8.33), and by assuming quasi neutrality ($n\approx\delta p$), the following ambipolar drift-diffusion equation for the electron density is obtained:

$$g-K(N_A+\delta p)n+\vec{\nabla}\cdot[\mu_a n\vec{E}^{\text{ext}}+D_a\vec{\nabla}n]=0 \tag{8.38}$$

where $\mu_a$ and $D_a$ are the ambipolar mobility and diffusion constant, respectively:

$$\mu_a=\frac{\mu_e\mu_h N_A^-}{n\mu_e+(n+N_A^-)\mu_h} \tag{8.39}$$

$$D_a=\frac{n\mu_e D_h+(N_A^-+\delta p)\mu_h D_e}{n\mu_e+(N_A^-+\delta p)\mu_h} \tag{8.40}$$

Note that here, the expression for the mobility is distinct from that of the usual ambipolar mobility [Smith (1978)]. This is because the ambipolar mobility is defined here with respect to the external electric field only, whereas the equation found in Smith (1978) uses the total electric field. For the spin density, the following equation is obtained:

$$\mathcal{P}_i g-K(N_A+\delta p)s-\frac{s}{T_1}+\vec{\nabla}\cdot[\mu_a s(\vec{E}^{\text{ext}}+\frac{D_h-D_e}{\mu_h N_A^-}\vec{\nabla}n)+D_e\vec{\nabla}s]=0 \tag{8.41}$$

### 8.1.5 Ambipolar spin diffusion in the degenerate regime

The system of Eq. (5.42), Eq. (5.43), Eq. (5.44) and Eq. (5.45) must be solved numerically since the conductivities and diffusion constants depend on space. However, an exact

numerical solution of these equations is difficult, since small errors in $n$ and $\delta p$ results in large errors in $\vec{E}$. This renders the equations highly nonlinear and a convergent solution is difficult to obtain using finit element methods without approximations. To address this, the hole continuity equation is replaced by a combination of combination of Eqs. (5.42) (multiplied by $\sigma_h$) and (5.44) (multiplied by $\sigma_c$) in the usual way presented by Smith (1978). Defining the reduced hole conductivity $\beta_h = \sigma_h/(\sigma_h + \sigma_c)$, of the form

$$\beta_h = \frac{N_A^- + n}{(N_A^- + n) + (\mu_0/\mu_h)[n_+\zeta(n_+) + n_-\zeta(n_-)]} \tag{8.42}$$

the following equation to describe the hole distribution is obtained

$$(g_+ + g_-) - \delta p/\tau + \frac{\vec{E}}{q}\vec{\nabla}\sigma_c^a + \vec{\nabla}[D_{cc}^a\vec{\nabla}\delta p + D_{cs}^a\vec{\nabla}s + \frac{1}{q}\beta_h\vec{\nabla}\vec{J_c^T}] = 0 \tag{8.43}$$

where

$$D_{cc}^a = \beta_h D_{cc} + (1-\beta_h)D_h \tag{8.44}$$

$$D_{cs}^a = \beta_h D_{cs} \tag{8.45}$$

and $\vec{\nabla}\sigma_c^a = \beta_h\vec{\nabla}\sigma_c - (1-\beta_h)\vec{\nabla}\sigma_h$. Equation (8.43) is approximate since, as justified in Paget et al. (2012), it assumes charge neutrality $[n = \delta p]$. Further, it neglects for simplicity the spatial dependences of electron and hole conductivities. However, this approximation appears to yield reasonable results. For example, at the highest excitation power where the equations are most strongly coupled, the sum of all the terms of the left hand of Eq. (5.42) is two orders of magnitude smaller than the maximum value of $\vec{\nabla}\cdot[D_{cc}\vec{\nabla}n]$ so that these terms efficiently compensate each other.

## 8.2 Boltzmann equation formalism for charge, spin and thermoelectric currents

The current $\vec{J_i}$ of photoelectrons of spin $i$ is given by

$$\vec{J_i} = -\frac{q}{m^*}\int \vec{p} f_i d^3p \tag{8.46}$$

where the function $f_i$, which describes the distribution of electrons of spin $i$ as a function of space and of momentum $\vec{p}$, is obtained from a resolution of the Boltzmann equation

$$\frac{\partial f_i}{\partial t} + \vec{p}\vec{\nabla}_r f_i - \frac{q\vec{E}}{m^*}\nabla_k f_i = [\frac{\partial f_i}{\partial t}]_{icoll} + [\frac{\partial f_i}{\partial t}]_{e-ecoll} \tag{8.47}$$

where the second term of the left hand accounts for the effect of diffusion in a Fermi energy gradient. The third term describes the effect of electric field and the two terms on the right hand are collision integrals accounting for electron-impurity collisions and electron-electron collisions.

Note that the more recent models of D'Amico and Vignale (2002); Flensberg et al. (2001) and Glazov and Ivchenko (2004) propose estimates of the collision integrals, but do not take into account spatial inhomogeneities of $f$, which play a crucial role. These inhomogeneities are considered in an independent approach by Chakravarti (1975). However, the latter approach neglects spin polarization, so that electron-electron-collisions have no effect.

Here, neglecting band nonparabolicity, we propose the following Ansatz to first order which reduces to the result of D'Amico and Vignale (2002) for a homogeneous electron gas and to that of Chakravarti (1975) for spin-unpolarized electrons.

$$\begin{aligned} f_i = f_{0i} &- \frac{\alpha_{ii}\tau_m(\varepsilon)}{m^*}\left[-q\vec{E}\cdot\vec{\nabla}_\varepsilon f_{0i} + \vec{p}\cdot\vec{\nabla}_r f_{0i}\right] \\ &- \frac{\alpha_{i,-i}\tau_m(\varepsilon)}{m^*}\left[-q\vec{E}\cdot\vec{\nabla}_\varepsilon f_{0,-i} + \vec{p}\cdot\vec{\nabla}_r f_{0,-i}\right] \end{aligned} \tag{8.48}$$

where for non coupled spins ($\alpha_{ij} = \delta_{ij}$) one recognizes the usual drift term in the electric field $\vec{E}$ and the diffusion term proportionnal to the spatial gradient $\vec{\nabla}_r f_{0i}$ [Chakravarti (1975)]. In order to take account of the spin-spin interactions for the evolution of $f_i$, it is natural to add a coupling term with the evolution of $f_{-i}$, using a coupling factor $\alpha_{i,-i}$ which describes the modification of conductivity $\sigma_{i,-i}$ caused by e-e collisions, defined in Eq.(5.5). In the same way, the evolution of $f_i$ is also modified by losses to the $-i$ spin reservoir, which are taken into account by the muliplicative factor $\alpha_{ii}$. It is considered here that $\tau_m(\varepsilon)$ does not depend on spin, so that the spin dependence of $\tau_{mi}$ used in Sec.5.3.1 originates solely from the spin dependence of the Fermi distribution. Eq. (8.46)

permits to calculate the currents using Eqs.(8.46), (8.48) and

$$\vec{\nabla}_r f_{0i} = -\frac{\partial f_{0i}}{\partial \varepsilon} \cdot \left[ \sum_j \frac{\partial E_{F_i}}{\partial n_j} \vec{\nabla}_r n_j + \left( \frac{\partial E_{F_i}}{\partial k_B T_e} + \frac{\varepsilon - E_{F_i}}{k_B T_e} \right) \vec{\nabla}_r (k_B T_e) \right] \tag{8.49}$$

Since the contribution of the equilibrium term $f_0$ is zero, the current is written as the sum of a drift current, of a diffusion current and of a thermoelectric current, respectively proportional to $\vec{E}$, $\vec{\nabla}_r n$, and $\vec{\nabla}_r (k_B T)$. This gives the expressions of the drift and diffusion currents given in chapter 5. Transforming the integration over momentum to an integration over kinetic energy, the expression of the average time $\tau_{mi}$ given by Eq. (5.19) is readily obtained. The thermoelectric charge and spin currents originate from the third term of Eq. (8.49). The thermal-induced change of $E_{F_i}$ at constant concentration, $\partial E_{F_i} / \partial k_B T_e$ is calculated by expressing that the derivative of $n_i = N_c^s \mathscr{F}_{1/2}^*(\eta_i)$ with respect to temperature, as found from Eq. (5.11), is zero. Using $\partial \mathscr{F}_k^*(\eta)/\partial \eta = \mathscr{F}_{k-1}^*(\eta)$, one finds the expression given in Eq. (5.34) for $\vec{K}_{ij}$.

# Bibliography

Ahrenkiel, R. K. (1993). Minority-carrier lifetime in iii-v semiconductors. *Semiconductors and Semimetals*, 39:Academic, New York.

Ahrenkiel, R. K., Duniavy, D. J., Greenberg, D., Schlupmann, H. C., Hamaker, and MacMillan, H. F. (1987). Electron mobility in p-gaas by time of flight. *Appl. Phys. Lett*, 51:776.

Amo, A., Vina, L., Lugli, P., Tejedor, C., Toropov, A. I., and Zhuravlev, K. S. (2007). Pauli blockade of the electron spin flip in bulk gaas. *Phys. Rev. B*, 75:085202.

Appelbaum, I., Huang, B., and Monsma, D. J. (2007). Electronic measurement and control of spin transport in silicon. *Nature*, 447:295–298.

Arscott, S., Peytavit, E., Vu, D., Rowe, A. C. H., and Paget, D. (2010). Fluidic assembly of hybrid mems: a gaas-based microcantilever spin injector. *J. Micromech. Microeng.*, 20:025023.

Awschalom, D. D. and Samarth, N. (2009). Spintronics without magnetism. *Physics*, 2:50.

Balocchi, A., Duong, Q. H., Renucci, P., Liu, B. L., Fontaine, C., Amand, T., Lagarde, D., and Marie, X. (2011). Full electrical control of the electron spin relaxation in gaas quantum wells. *Phys. Rev. Lett*, 107:136604.

Bennett, H. S. (2002). Multidimensional, closed-form analytic expression for mobilities in gaalas heterostructures. *J. Appl. Phys.*, 92:4475.

Beyzavi, K., Lee, K., Kim, D. M., Nathan, M. I., Wrenner, K., and Wright, S. L. (1991). Temperature dependence of minotiy-carrier mobility and recombination time in p-type gaas. *Appl. Phys. Lett*, 58:1268.

## Bibliography


Bir, G. L., Aronov, A. G., and Pikus, G. E. (1975). Spin relaxation of electrons due to scattering by holes. *JETP*, 42:705.

Blakemore, J. S. (1982). Semiconducting and other major properties of gallium arsenide. *J. Appl. Phys.*, 53:R123.

Borghs, G., Bhattacharyya, K., Deneffe, K., Vanmieghem, P., and Mertens, R. (1989). Band-gap narrowing in highly doped n- and p-type gaas studied by photoluminescence spectroscopy. *J. Appl. Phys.*, 66:4381.

Brechet, S. D. and Ansermet, J. P. (2010). Spin soret effect. *arxiv: 1011.2323v1 [cond-mat. mes-hall]*.

Cadiz, F., Barate, P., Paget, D., Grebenkov, D., Korb, J. P., Rowe, A. C. H., Amand, T., Arscott, S., and Peytavit, E. (2014). All optical method for investigation of spin and charge transport in semiconductors: Combination of spatially and time-resolved luminescence. *J. Appl. Phys.*, 116:023711.

Cadiz, F., Paget, D., Rowe, A. C. H., Amand, T., Barate, P., and Arscott, S. (2015a). Effect of the pauli principle on photoelectron spin transport in p+ gaas. *Phys. Rev. B*, 91:165203.

Cadiz, F., Paget, D., Rowe, A. C. H., Berkovits, V. L., Ulin, V. P., Arscott, S., and Peytavit, E. (2013). Surface recombination in doped semiconductors: Effect of light excitation power and of surface passivation. *J. Appl. Phys.*, 114:103711.

Cadiz, F., Paget, D., Rowe, A. C. H., Peytavit, E., and Arscott, S. (2015b). Central role of electronic temperature for photoelectron charge and spin mobilities in p+ gaas. *Appl. Phys. Lett*, 106 (9):092108.

Cameron, A. R., Riblet, P., and Miller, A. (1996). Spin gratings and the measurement of electron drift mobility in multiple quantum well semiconductors. *Phys. Rev. Lett*, 76:4793.

Carlslaw, H. S. and Jaeger, J. C. (1966). *Conduction of heat in solids*. Oxford University press.

**Bibliography**

Chakravarti, A. N. (1975). Theory of electron diffusion under a temperature-gradient in degenerate semiconductors having non-parabolic energy-bands. *Czech. J. Phys. B*, 25:778.

Chattopadhyay, D. and Queisser, H. J. (1981). Electron scattering by ionized impurities in semiconductors. *Rev. Mod. Phys.*, 53:745.

Chazalviel, J. N. (1999). *Coulomb Screening by Mobile Charges*. Birkhäuser.

Collet, J. and Amand, T. (1986). Model calculation of the laser semiconductor interaction in subpicosecond regime. *J. Phys. Chem. Sol*, 47:153.

Collet, J. H. (1993). Screening and exchange in the theory of the femtosecond kinetics of the electron hole plasma. *Phys. Rev. B*, 47:10279.

Colomb, C. M., Stockman, S. A., Varadarajan, S., and Stillman, G. E. (1992). Minority-carrier transport in carbon doped gallium-arsenide. *Appl. Phys. Lett*, 60:65.

Crooker, S. A. and Smith, D. L. (2005). Imaging spin flows in semiconductors subject to electric, magnetic, and strain fields. *Phys. Rev. Lett*, 94:236601.

Cutler, M. and Mott, N. F. (1969). Observation of anderson localization in an electron gas. *Phys. Rev.*, 181:1336.

D'Amico, I. and Vignale, G. (2000). Theory of spin coulomb drag in spin-polarised transport. *Phys. Rev. B*, 62:4853.

D'Amico, I. and Vignale, G. (2002). Coulomb interaction effects in spin-polarized transport. *Phys. Rev. B*, 65:085109.

Datta, S. and Das, B. (1990). Electronic analog of the electrooptic modulator. *App. Phys. Lett*, 56:665.

Dresselhaus, G. (1955). Spin-orbit coupling eeffect in zinc-blende structures. *Phys. Rev.*, 100:580.

Dumke, W. P. (1963). Optical transitions involving impurities in semiconductors. *Phys. Rev.*, 132:1998.

**Bibliography**

Duran, M., Muga, I., and Nédélec, J. C. (2005). The helmholtz equation with impedance in a half space. *Comptes Rendus Mathematiques*, 341:561.

D'yakonov, M. I. and Perel, V. I. (1971a). Possibility of orienting electron spin with current. *JETP Lett.*, 13:467.

D'yakonov, M. I. and Perel, V. I. (1971b). Spin orientation of electrons associated with the interband absoption of light in semiconductors. *Sov. Phys. JETP*, 33:1053.

Efros, A. L., Halpern, Y. S., and Shklovsky, B. I. (1972). *Proceedings of the International Conference on Physics of semiconductors, Warsaw 1972*. Polish Scientific publishers, Warsaw.

Favorskiy, I., Vu, D., Peytavit, E., Arscott, S., Paget, D., and Rowe, A. C. H. (2010). Circularly polarized luminescence microscopy for the imaging of charge and spin diffusion in semiconductors. *Rev. Sci. Instr.*, 81:103902.

Finkelshtein, A. M. (1983). Influence of coulomb interaction on the properties of disordered metals. *Sov. Phys. JETP*, 57:97–108.

Flensberg, K., Jensen, T. S., and Mortensen, N. A. (2001). Diffusion equation and spin drag in spin-polarized transport. *Phys. Rev. B*, 64:245308.

Furuta, T., Taniyama, H., and Tomizawa, M. (1990). Minority electron-transport property in p-gaas under high electric-field. *J. Appl. Phys.*, 67:293.

Gerhardt, N. C., Li, M. Y., Jahme, H., Hopfner, H., Ackemann, T., and Hofmann, M. R. (2011). Ultrafast spin-induced polarization oscillations with tunable lifetime in vertical-cavity surface-emitting lasers. *Appl. Phys. Lett*, 99:151107.

Glazov, M. M. and Ivchenko, E. I. (2004). Effect of electron-electron interaction on spin relaxation of charge carriers in semiconductors. *JETP*, 99:1279.

Hankiewicz, E. M. and Vignale, G. (2009). Spin-hall effect and spin coulomb drag in doped semiconductors. *J. Phys.: Condens. Matter*, 21:253202.

Harmon, E. S., Lovejoy, M. L., and Melloch, M. R. (1993). Experimental observation of a minority electron mobility enchancement in degeneratel doped p-type gaas. *Appl. Phys. Lett*, 63:536.

Henn, T., Kiessling, T., Ossau, W., Molenkamp, L. W., Reuter, D., and Wieck, A. D. (2013). Picosecond real-space imaging of electron spin diffusion in gaas. *Phys. Rev. B*, 88:195202.

Hernandez-Minguez, A., Biermann, K., Hey, R., and Santos, P. V. (2014). Spin transport and spin manipulation in gaas (110) and (111) quantum wells. *Phys. Status Solidi B*, 251:1736.

Horinaka, H., Ono, D., Zhen, W., Wada, K., Cho, Y., Hayashi, Y., Nakanishi, T., Okumi, S., Aoyagi, H., Saka, T., and Kato, T. (1995). Spin relaxation of electrons in strained gaas layer photocatode of polarized electron source. *Jpn. J. Appl. Phys*, 34:6444.

Jungwirth, T., Wunderlich, J., and Olejnik, K. (2012). Spin hall effect devices. *Nature Materials*, 11:382–390.

Kainz, J. and Rossler, U. (2004). Temperature dependece of dyakonov-perel spin relaxation in zinc-blende semiconductor quantum structures. *Phys. Rev. B*, 70:195322.

Kalevich, V. K., Paillard, M., Kavokin, K. V., Marie, X., Kovsh, A. R., Amand, T., Zhukov, A. E., Musikhin, Y. G., Ustinov, V. M., Vanelle, E., et al. (2001). Spin redistribution due to pauli blocking in quantum dots. *Phys. Rev. B*, 64(4):045309.

Kaneto, T., Kim, K., and Littlejohn, M. (1993). Calculation of minority-carrier mobilities in heavily-doped p-type semiconductors in the dielectric-function formalism. *Phys. Rev. B*, 47:16257.

Kato, Y. K., Myers, R. C., Gossard, A. C., and Awschalom, D. D. (2004). Observation of the spin hall effect in semiconductors. *Science*, 306:1910.

Kiessling, T., Quast, J. H., Kreisel, A., Henn, T., Ossau, W., and Molenkamp, L. (2012). Spatially resolved photocarrier energy relaxation in low doped bulk gaas. *Phys. Rev. B*, 86:161201.

Kikkawa, J. M. and Awschalom, D. D. (1999). Lateral drag of spin coherence in gallium arsenide. *Nature*, 397:139.

Kim, S., Son, C., Chung, S., Park, Y., Kim, E., and Min, S. (1997). Temperature-dependent hall analysis of carbon-doped gaas. *Thin Solid Films*, 310:63.

**Bibliography**

Koralek, J. D., Weber, C. P., Orenstein, J., Bernevig, B. A., Zhang, S. C., Mack, S., and Awschalom, D. D. (2009). Emergence of the persistent spin helix in semiconductor quantum wells. *Nature*, 458:610.

Lampel, G. (1968). Nulcear dynamic polarization by optical electronic saturation and optical pumping in semiconductors. *Phys. Rev. Lett*, 20:491.

Leo, K. and Collet, J. H. (1991). Influence of the electron hole scattering on the plasma thermalization in doped gaas. *Phys. Rev. B*, 44:5535.

Look, D. C., Stutz, C. E., Sizelove, J. R., and Evans, K. R. (1996). On hall scattering factors for holes in gaas. *J. Appl. Phys.*, 80:1913.

Lovejoy, M. L., Melloch, M. R., and Lundstrom, M. S. (1995). Temperature dependence of minority and majority carrier mobilities in degenerately doped gaas. *Appl. Phys. Lett*, 67:1101.

Lowney, J. R. and Bennett, H. S. (1991). Majority and minority electron and hole mobilities in heavily doped gaas. *J. Appl. Phys.*, 69:7102.

Luber, D., Bradley, F., Haegel, N., Talmadge, M., Coleman, M., and Boone, T. (2006). Imaging transport for the determination of minority carrier diffusion length. *Appl. Phys. Lett*, 88:163509.

Mahan, G. D. (1981). *Many-Particle Physics*. Plenum.

Meier, F. and Zakharchenya, B. (1984). *Optical Orientation (North-Holland, Amsterdam)*.

Murakami, S., Nagaosa, N., and Zhang, S. C. (2003). Dissipationless quantum spin current at room temperature. *Science*, 301:1348.

Nelson, R. J. and Sobers, R. G. (1978). Minority-carrier llifetimes and internal quantum efficiency of surface-free gaas. *J. Appl. Phys.*, 49:6103.

Nemec, P., Kerachian, Y., van Driel, H. M., and Smirl, A. L. (2005). Spin-dependent electron many-body effects in gaas. *Phys. Rev. B*, 72:245202.

Okamoto, N., Kurebayashi, H., Trypiniotis, T., Farrer, I., Ritchie, D. A., Saitoh, E., Sinova, J., Masek, J., Jungwirth, T., and Barnes, C. H. W. (2014). Electric control of the spin hall effect by intervalley transitions. *Nature Materials*, 13:932.

**Bibliography**

Paget, D., Cadiz, F., Rowe, A. C. H., Moreau, F., Arscott, S., and Peytavit, E. (2012). Imaging ambipolar diffusion of photocarriers in gaas thin films. *Journal of Applied Physics*, 111:123720.

Pauling, L. (1960). *The Nature of the Chemical Bond*. Cornell University Press, New York.

Popovic, R. S. (2004). *Hall effect devices*. Institute of Physics Publishing, Bristol.

Pugnet, M., Collet, J., and Cornet, A. (1981). Cooling of hot electron-hole pplasma in the prescence of screened electron-phonon interactions. *Solid State Communications*, 38:531.

Qi, Y., Yu, Z. G., and Flatte, M. E. (2006). Spin gunn effect. *Phys. Rev. Lett*, 96:026602.

Quang, D. N., Dat, N. N., and Vanan, D. (1993). On the electron-mobility in slightly compensated heavily-doped gaas at low-temperatures. *Phys. Lett. A*, 182:125.

Quast, J., Henn, T., Kiessling, T., Ossau, W., Molenkamp, L., Reuter, D., and Wieck, A. (2013). Hot carrier effects on lateral electron spin diffusion in n-type gaas. *Phys. Rev. B*, 87:205203.

Ross, J. S., Sanfeng, W., Hongy, Y., Ghimire, N. J., Jones, A. M., Aivazian, G., Yan, J., Mandrus, D. G., Xiao, D., Yao, W., and Xu, X. (2013). Electrical control of neutral and charge excitons in a monolayer semiconductor. *Nature Communications*, 4:1474.

Rougemaille, N., Lamine, D., Lampel, G., Lassailly, Y., and Peretti, J. (2008). Injection energy dependence of spin-polarized hot-electron transport through a ferromagnetic metal/oxyde/semiconductor junction. *Phys. Rev. B*, 77:094409.

Schultes, F., Christian, T., Jones-Albertus, R., Pickett, E., Alberi, K., Fluegel, B., Liu, T., Misra, P., Sukiasyan, A., Yuen, H., and Haegel, N. (2013). Temperature dependence of diffusion length, lifetime and minority electron mobility in gainp. *Appl. Phys. Lett*, 103:242106.

Seymour, R. J., Junnarkar, M. R., and Alfano, R. R. (1982). Slowed picosecond kinetics of hot photogenerated carriers in gaas. *Solid State Communications*, 41:657.

Shah, J. (1999). *Ultrafast Spectroscopy of Semiconductors and Semiconductor Nanostructures*. Springer, Berlin.

Shapiro, S. L. and Teukolsky, S. A. (1983). *Black Holes, White Dwarfs and Neutron Stars, The Physics of Compact Objects*. Wiley, New York.

Sinova, J., Culcer, D., Niu, Q., Sinitsyn, N. A., Jungwirth, T., and MacDonald, A. H. (2004). Universal intrinsic spin hall effect. *Phys. Rev. Lett*, 92:126603.

Smith, R. A. (1978). *Semiconductors*. Cambridge University Press, Cambridge.

Soret, C. (1879). *Archives des Sciences Physiques et Naturelles, Geneve*, 2:48.

Takahashi, Y., Inaba, N., and Hiroshe, F. (2008). Temperature dependence of spin-polarized electron transport including electron-electron interaction. *J. Appl. Phys.*, 104:023714.

Tea, E. and Aniel, F. (2011). Minority electron mobilities in gaas, in0.53ga0.47as, and gaas0.5sb0.5 calculated within an ensemble monte carlo model. *J. Appl. Phys.*, 109:033716.

Truscott, A. G., Strecker, K. E., McAlexander, W. I., Partridge, G. B., and Hulet, R. G. (2001). Observation of fermi pressure in a gas of trapped atoms. *Science*, 291:2570–2572.

Ulbrich, R. (1973). Energy relaxation of photoexcited hot electrons in gaas. *Phys. Rev. B*, 8:5719.

Ulrich, B., Munshi, S. R., and Brown, G. J. (2007). Photoluminescence analysis of p-doped gaas using the roosbroeck shockley relation. *Semiconductor Science and Technology*, 22:1174.

Volkl, R., Griesbeck, M., Tarasenko, S. A., Schuh, D., Wegscheider, W., Shuller, C., and Korn, T. (2011). Spin dephasing and photoinduced spin diffusion in a high-mobility two-dimensional electron system embedded in a gaas-(al,ga)as quantum well grown in the [110] direction. *Phys. Rev. B*, 83:241306.

Vu, D., Jurca, F., Maroun, F., Allongue, P., Tournerie, N., Rowe, A. C. H., and Paget, D. (2011). Spin-dependent photoelectron tunnneling from gaas into magnetic cobalt. *Phys. Rev. B*, 83:121304.

Walukiewicz, W., Lagowki, J., Jastrzebski, L., and Gatos, H. (1979). Minority-carrier mobility in p-type gaas. *J. Appl. Phys.*, 50:5040.

Wang, G., Balocchi, A., Lagarde, D., Zhu, C. R., Amand, T., Renucci, P., Shi, Z. W., Wang, W. X., Liu, B. L., and Marie, X. (2013a). Temperature dependent electric field control of the electron spin relaxation in (111)a gaas quantum wells. *Appl. Phys. Lett*, 102:242408.

Wang, G., Liu, B. L., Balocchi, A., Renucci, P., Zhu, C. R., Amand, T., Fontaine, C., and Marie, X. (2013b). Gate control of the electron spin-diffusion length in semiconductor quantum wells. *Nature Communications*, 4:2372.

Weber, C. P., Benko, C. A., and Hiew, S. C. (2011). Measurement of spin diffusion in semi-insulating gaas. *J. Appl. Phys.*, 109:106101.

Weber, C. P., Gedik, N., Moore, J. E., J.Orenstein, Stephens, J., and Awschalom, D. D. (2005). Observation of spin coulomb drag in a two-dimensional electron gas. *Nature*, 437:1330.

Wunderlich, J. (2010). Spin hall effect transistor. *Science*, 330:1801.

Wunderlich, J., Kaestner, B., Sinova, J., and Jungwirth, T. (2005). Experimental observation of the spin-hall effect in a two-dimensional spin-orbit coupled semiconductor system. *Phys. Rev. Lett*, 94:047204.

Zerrouati, K., Fabre, F., Bacquet, G., Bandet, J., Frandon, J., Lampel, G., and Paget, D. (1988). Spin lattice relaxation in p-type gallium arsenide single crystals. *Phys. Rev. B*, 37:1334.

Zhang, T. T., Barate, P., Nguyen, C. T., Ballochi, A., Amand, T., Renucci, P., Carrere, H., Urbaszek, B., and Marie, X. (2013). L-valley electron spin dynamics in gaas. *Phys. Rev. B*, 87:041201(R).

Zutic, I., Fabian, J., and Erwin, S. C. (2007). Bipolar spintronics: From spin injection to spin-controlled logic. *J. Phys. Condens. Matt*, 19:165219.